ACOUSTIC SURFACE WAVE EXCITATION IN LAYERED STRUCTURES

by

Douglas H. Hurlburt, B.A. (Physics)(Johns Hopkins),
M.Sc. (Physics)(McGill)

A thesis submitted to the Faculty of Graduate Studies and Research
in partial fulfillment of the requirements for the degree of
Doctor of Philosophy

Department of Electrical Engineering
McGill University
Montreal, Canada

JULY, 1972

ABSTRACT

An analytical and computational procedure for the study of acoustic surface wave excitation in anisotropic layered structures has been developed. The analysis is based upon solution of the coupled wave equations and is directed toward "low coupling" materials which can be oriented such that the particle displacements are in the sagittal plane.

The admittance characteristics (complex) of interdigital transducers, as used to excite surface waves in such structures, are calculated and compared with experimental results. The behaviour and interactions of surface waves within the region occupied by the transducer are presented and analyzed. Also a simple mathematical model for an interdigital transducer is discussed and the results calculated using this model are compared with the general theory.

The computational methods and procedures are also considered.

ACOUSTIC SURFACE WAVE EXCITATION IN
LAYERED STRUCTURES

by

Douglas H. Hurlburt, B.A. (Physics)(Johns Hopkins),
M.Sc.(Physics)(McGill)

Department of Electrical Engineering

ACOUSTIC SURFACE WAVE EXCITATION IN LAYERED STRUCTURES

by

Douglas H. Hurlburt, B.A.(Physics)(Johns Hopkins),
M.Sc.(Physics)(McGill)

A thesis submitted to the Faculty of Graduate Studies and Research
in partial fulfillment of the requirements for the degree of
Doctor of Philosophy

Department of Electrical Engineering
McGill University
Montreal, Canada

JULY,1972

ABSTRACT

An analytical and computational procedure for the study of acoustic surface wave excitation in anisotropic layered structures has been developed. The analysis is based upon solution of the coupled wave equations and is directed toward "low coupling" materials which can be oriented such that the particle displacements are in the sagittal plane.

The admittance characteristics (complex) of interdigital transducers, as used to excite surface waves in such structures, are calculated and compared with experimental results. The behaviour and interactions of surface waves within the region occupied by the transducer are presented and analyzed. Also a simple mathematical model for an interdigital transducer is discussed and the results calculated using this model are compared with the general theory.

The computational methods and procedures are also considered.

ACKNOWLEDGEMENTS

The author wishes to gratefully acknowledge the assistance and guidance of Dr. G.W. Farnell throughout the course of this research. He also wishes to thank Dr. M.P. Bachynski, Dr. R.J. McIntyre, Dr. I.P. Shkarofsky and other members of the Research Laboratories of RCA Limited for their assistance and numerous suggestions. Also, Dr. E. Adler and Mr. A. Fahmy of McGill University for many fruitful discussions and technical assistance.

Special thanks are due Dr. M. Holland of the Raytheon Research Division, Waltham, Mass., for providing the $ZnO - SiO_2$ samples that were used in Chapter V; and Dr. F.S. Hickernell, of the Motorola Government Electronics Division, Scottsdale, Ariz., for information on surface wave velocities and transducers.

Mr. S.A. Rahman and Miss T. Hackett carefully prepared the numerous graphs and diagrams; and Mrs. M. Goldfinch swiftly and accurately typed a long and complicated manuscript.

Funds for computer use and general research needs were supplied under grant no. A-589 from the National Research Council, Ottawa.

TABLE OF CONTENTS

CHAPTER V COMPARISON BETWEEN COMPUTED AND MEASURED ADMITTANCE DATA

CHAPTER VI SURFACE WAVE BEHAVIOUR WITHIN THE TRANSDUCER

CHAPTER VII A SIMPLE TRANSDUCER MODEL

AN ABRIDGED SYMBOLS LIST

The following is a list of the most commonly used symbols. Other symbols are used in specific instances and they will be defined as their use dictates. Functions are, in general, deleted from this list, but will be defined as they appear. The following notes apply to the symbolic notation:

(1) Subscripts and superscripts will be added to the basic variable, as required, but the basic definition of the variable will remain unchanged.

(2) A "-" appearing over a variable will be used to imply the Fourier transform of the variable.

(3) A "^" appearing over a variable will denote that the variable is evaluated in the layer.

(4) The symbol "*" is used to indicate the complex conjugate.

LIST:

A_n	coefficients of the harmonic electric potential expansion
$AP^{(\pm)}$	"amplitude factors" for the wave solutions
C_m	coefficients of the homogeneous wave solutions outside the transducer region
c_{ijkl}, c_{ij}	elements of the elastic tensor in tensor and matrix notation, respectively
D, D/2	length and "half-length" of the transducer, respectively
D_m	components of the electric displacement vector
$D_m^{(\pm)}$	coefficients of the homogeneous wave solutions within the transducer region
d	width of individual fingers in the transducer
E_m	components of the electric field
e_{mij}, e_{ij}	elements of the piezoelectric tensor in tensor and matrix notation, respectively
H	layer thickness

k, k_s, k_b	the wave number (general, surface wave, branch point, respectively)
L	center-to-center spacing of adjacent fingers in the transducer
l_m	roots of the "secular equation"
M_m	decay constants for the electric potential function
m_o	the number of finger pairs in the transducer ($D/2 = m_o L$)
S_{ij}, S_i	components of the strain in tensor and matrix notation, respectively
T_{ij}, T_i	components of the stress in tensor and matrix notation, respectively
t	time
U_k	a general particle displacement, also particle displacements in layer
V_j	a general particle displacement
V_o	the applied signal voltage
v, v_s, v_b	wave velocity (general, surface wave, branch point, respectively)
W_j	particle displacements in the substrate
W_o	finger overlap, or aperture, of the transducer
$x, 1$ $y, 2$ $z, 3$	coordinate axes as letters and numbers
α_{jm}	eigenvectors for the homogeneous solutions
Γ_{ij}	elements of the general wave equations
γ_{ij}	the elements Γ_{ij} after application of the Fourier transform
$\varepsilon_{mn}, \varepsilon_m$	elements of the dielectric tensor in tensor and matrix notation, respectively
θ_i	driving terms for the inhomogeneous wave equations
Λ	left-hand side of the boundary condition equations
ρ	mass density
ϕ	general electric potential function

ψ	electric potential function of an infinite transducer
ω	angular frequency

CHAPTER I

INTRODUCTION

1.1 History

Developments of the last decade in the field of ultrasonics have focussed increasing attention on the generation and propagation of elastic surface waves in anisotropic materials*. This interest originally resulted from their use in ultrasonic delay lines and guided wave structures[2,45,62,66,71], as well as surface wave amplifiers[27,72,75,77]. More recently it has been shown that acoustic surface wave filters can be fabricated[28,35,65] and surface waves show considerable promise in the general field of signal processing[45,62]. It has been proposed that surface wave devices, with properties analogous to those of electromagnetic waveguide devices, can be developed with a considerable overall reduction in size[62]. It has also been shown that many of the techniques which evolved for the analysis of electromagnetic problems can be applied to the analysis of acoustic wave devices[3].

The study of elastic surface waves began with the theoretical formulation for waves on the free surface of an isotropic solid by Lord Rayleigh[42], which was later extended by Love[43] and Lamb[39]. In 1924, Stoneley[63] considered the problem of elastic waves propagating at the interface of two semi-infinite isotropic solids; however, the propagation of elastic waves on the free surface remained the dominant interest for many years. With the increasing sophistication of surface wave devices, the study of

---

* The interested reader is referred to the excellent review paper by R.M. White[73], with its complete bibliography, in addition to the general bibliography by Smith and Damon[56]. The paper of Slobodnik and Conway[59] contains extensive information on the characteristics of surface wave materials.

elastic surface waves has been fully extended into the realm of anisotropic layered media in the last few years[21,23,41,50,51]. Layered media have proved to be of considerable interest, with respect to surface wave devices, because of the ability to derive benefit from the different materials used, e.g. a piezoelectric layer may be used to excite surface waves on a non-piezoelectric substrate[23].

Early transducers for the generation and detection of elastic surface waves consisted of a wedge arrangement, through which a homogeneous bulk wave was converted into a surface wave[69]. Other variations on the bulk-to surface wave theme are possible[33], although they have largely been restricted to the generation of waves on free surfaces. The introduction of the "interdigital" (ID) transducer[15,73,74], which has become the standard means of generating and detecting elastic surface waves, made possible the direct generation of waves on free surfaces, as well as in layered structures.

The theoretical study of the excitation and detection of elastic surface waves on the free surface of piezoelectric materials, using ID transducers, has been the topic of several papers[15,36,58]. Of these studies, that by Smith et al.[58] has been very successful in deriving a "model" that can be fitted to experimental data. With the growing interest in layered structures, some efforts have been made to use this "model" to describe the behaviour of ID transducers in such structures[20,30,32,60,61]. However, a theoretical treatment of surface wave excitation in layered structures, of the type performed by Joshi and White[36] for the free surface, has not yet been attempted.

1.2 Thesis Background and Purpose

This thesis evolved from experiments being conducted at McGill University on the generation and propagation of acoustic surface waves in layered structures, in the fall of 1969. The purpose of these experiments was to generate and detect surface waves in layered structures using sputtered layers of CdS as the piezoelectric material, and non-piezoelectric substrates, such as silicon.* The work of Joshi and White[36] had appeared only a few months prior to these investigations, while the work of Smith et al.[58] appeared during the course of the experiments. The analysis of Joshi and White[36] was "aesthetically" satisfying in the sense that it was based on the true physics of the problem; however, it was felt that it lacked completeness in its failure to obtain the wave solutions within the transducer region. The "Stanford Model" of Smith et al.[58] was not as satisfying, for it is difficult to justify such a model from a theoretical analysis of surface wave behaviour; although, undeniably, it could predict the transducer admittance characteristics with considerable accuracy.

The experiments using CdS on Si were suffering from severe insertion loss problems, for reasons that were not fully understood until much later. Thus, it was decided to postpone the experimental effort and attempt a theoretical study of acoustic surface wave excitation in layered media. The intent of this study was to concentrate on "low-coupling" materials, such as CdS and ZnO, in conjunction with non-piezoelectric materials, for the layer and substrate, respectively. It was felt desirable to fill in some of the apparent gaps left in the analysis of Joshi and White[36], and at the same time try to obtain greater insight into the behaviour of the surface waves in the region of the ID transducer. An

---

* Recently, Schnitzler et al.[52] have reported surface wave excitation with CdS on glass.

attempt would also be made to add "rigor" to the analysis of Smith et al.[58].

1.3 Thesis Summary

The remainder of this manuscript will be devoted to the study of acoustic surface wave excitation in layered structures, and related problems. It will be seen that the dispersion present in such structures can be implicitly included, and the effect such dispersion has on the electrical properties of the transducer will be demonstrated. The wave solutions within the transducer will be derived and used to show how the waves interact within this region. The transducer admittance characteristics will be calculated using the wave solutions both inside and outside the transducer region, and will be shown to agree very well with measured data. A simple mathematical model, which contains the essence of the "Stanford Model"[58], will be derived and used to describe both the wave behaviour within the transducer region and the transducer admittance. The analysis will also be used to examine the effect of changes in the elastic and piezoelectric constants on the transducer admittance characteristics.

As with many studies of this nature, extensive use of a high speed digital computer is necessary for the determination of theoretical results. Thus, one chapter and a portion of one appendix will be devoted to the computational methods involved.

CHAPTER II

THEORY

2.1 Introduction

Before proceeding with the formal solution of the "inhomogeneous layer problem", a certain amount of groundwork must be prepared. In this section the topics to be presented include:

(1) the nature of the transducer structure (2.1.1)

(2) the coordinate system to be used (2.1.2)

(3) the general equations of motion for a piezoelectric material (2.1.3)

  (a) the general inhomogeneous problem
  (b) the inhomogeneous problem with a low coupling approximation

(4) the electric potential function to be used (low coupling) (2.1.4)

(5) the steps leading to the solution of the "inhomogeneous layer problem" (low coupling) (2.1.5) .

A low coupling approximation will be introduced as an approximation which greatly simplifies the method of solution and one which is reasonable for materials such as quartz, cadmium sulfide and cadmium selenide[50]. As shown in section 2.1.3, this permits the analysis to be separated into two parts: a purely electrostatic portion and a forced elastic portion. The solution to the electrostatic part is then used as the driving term for the elastic portion. If the piezoelectric coupling of the materials is not small, as is the case for $LiNbO_3$, one would expect that the analysis cannot be separated in the same fashion. However, as will be shown, for certain orientations of $LiNbO_3$ the errors introduced by separating the analysis in this fashion are not serious. It will be assumed that the materials used for the layer and substrate are perfect dielectrics and the possible effects of conductivity will be ignored.

2.1.1 The Interdigital Transducer

The interdigital (ID) transducer, which has become the generally accepted method for the generation of elastic surface waves, consists of a grid of parallel metallic strips, as shown in Fig. 2.1a. From an electrical standpoint, the fingers of the ID transducer can be driven in several ways. The most common is to operate the fingers in a push-pull fashion, with adjacent fingers of opposite polarity, as shown in Fig. 2.1b. This drive scheme is suitable for an ID transducer located on the free surface, or at the interface, with or without a metallic plating. Another drive scheme, suitable only for an ID transducer in conjunction with a metallic plating, is to operate all of the fingers in phase and of opposite polarity to the plating. This form of drive is shown in Fig. 2.1c. For most transducer applications, the separation between adjacent fingers, as well as their width, is the same throughout the length of the transducer and the overlap of adjacent fingers, W_o, is constant. This is the only situation that will be considered in the analysis to follow; however, it has been shown that by varying both the finger overlap and the spacing it is possible to make ID transducers that behave as filters with many useful properties[28,35,65].

2.1.2 Coordinate System

The coordinate system, shown in Fig. 2.2, has the origin located at the interface of the layer and substrate such that the substrate occupies the half-space $z < 0$, while the layer is in the region $0 < z < H$. Figure 2.3 shows the orientation of the ID transducer with respect to the coordinate system. The fingers of the transducer are parallel to the y-axis,

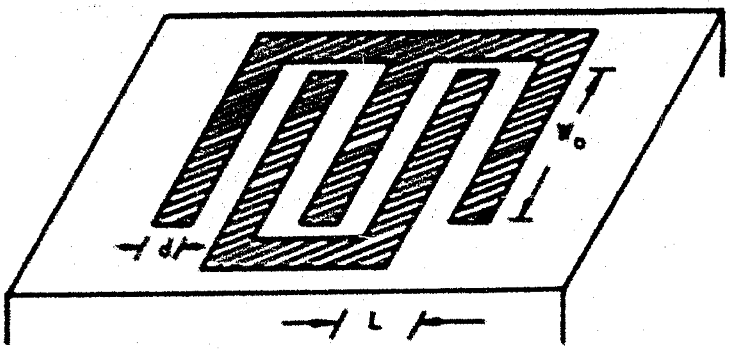

Figure 2.1(a)

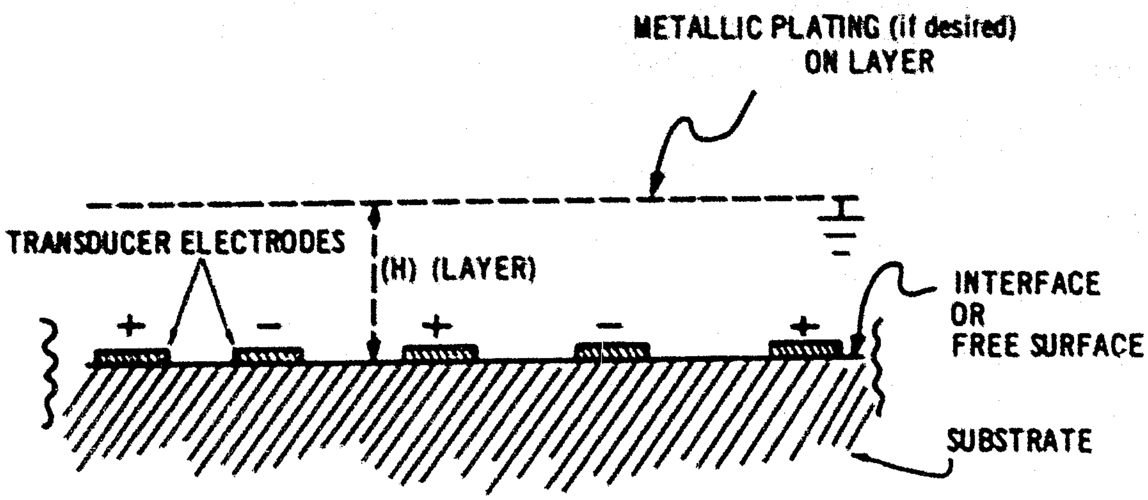

Figure 2.1(b)

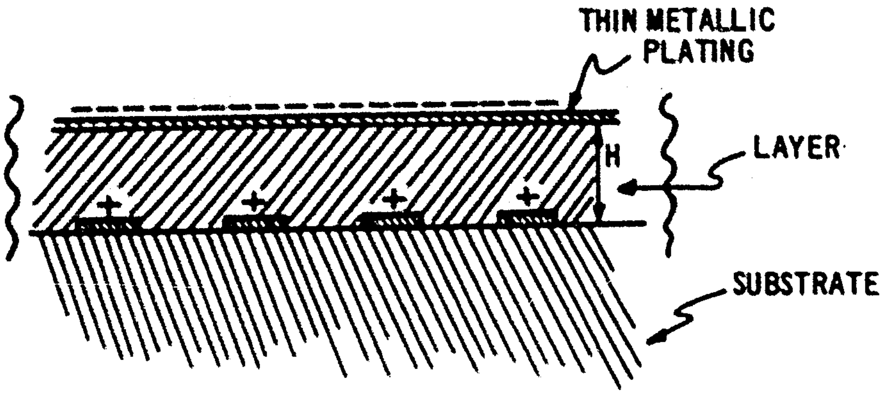

Figure 2.1(c)

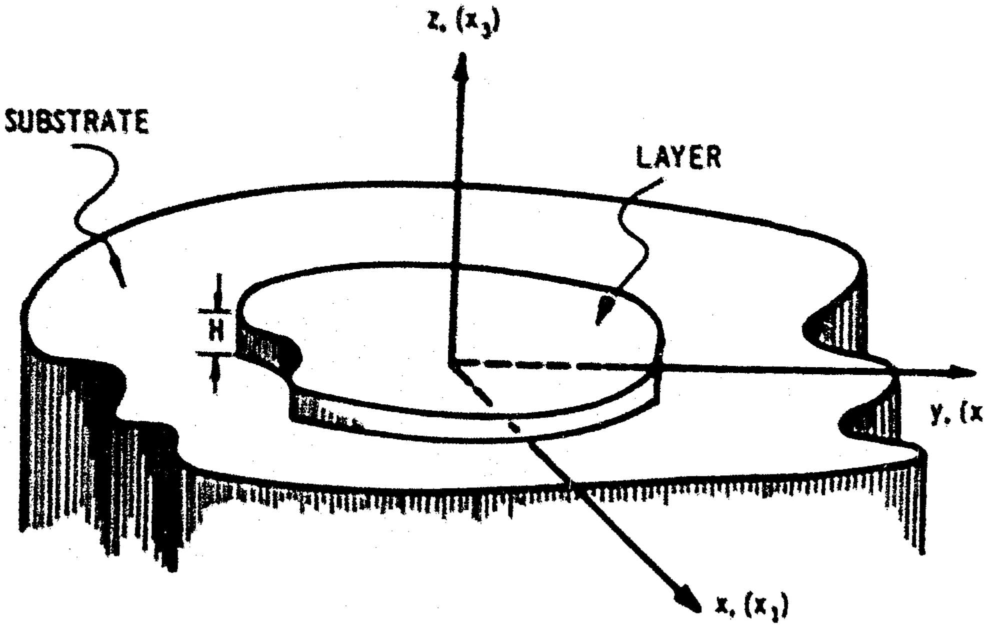

Figure 2.2

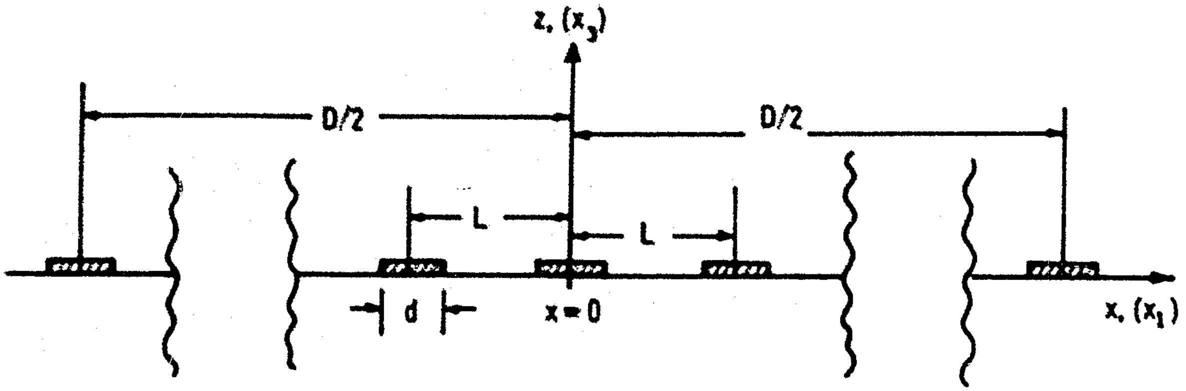

Figure 2.3

and are assumed to be very long compared to their width. This assumption implies that there is no component of the applied electric field parallel to the y-axis; and thus $\partial\phi_a/\partial y = 0$, where ϕ_a represents the applied electric potential function. The center-to-center distance of adjacent fingers is given by L, while the width of individual fingers is d. The centers of the end fingers of the transducer are located at $x = \pm D/2$, with the center of a finger located at the origin. Hence, D/2 is an integer times L. It will be assumed that the thickness of the fingers is much less than their width. The overlap of adjacent fingers, W_o, will often be referred to as the "aperture" of the transducer.

2.1.3 Equations of Motion for a Piezoelectric Material

The study of wave generation and propagation in piezoelectric materials begins with the "equations of state" for a piezoelectric medium[6],

$$T_{ij} = c_{ijkl}S_{kl} + e_{mij}\,\partial\phi/\partial x_m \tag{2.1}$$

and

$$D_m = e_{mkl}S_{kl} - \epsilon_{mn}\,\partial\phi/\partial x_n \; ; \tag{2.2}$$

where:* T_{ij} are the elements of the stress tensor

S_{kl} are the elements of the strain tensor, $S_{kl} = \frac{1}{2}\left(\frac{\partial U_k}{\partial x_l} + \frac{\partial U_k}{\partial x_k}\right)$

U_k are the particle displacements

x_l are the coordinate system axes

ϕ is the electric potential function, $E = -\mathrm{grad}(\phi)$

D_m are the elements of the electric displacement vector

c_{ijkl} are the elements of the stiffness tensor at constant E

e_{mij} are the elements of the piezoelectric tensor

ϵ_{mn} are the elements of the dielectric tensor at constant S.

Newton's Law can be written[6]

---

* An abridged symbols list will be found on page v .

$$\rho \frac{\partial^2 U_i}{\partial t^2} = \frac{\partial T_{ij}}{\partial x_j} \quad , \tag{2.3}$$

where ρ = mass density of the material.

By invoking the symmetry properties of the c_{ijkl},[49]

$$c_{ijkl} = c_{ijlk} = c_{jikl} \quad ,$$

equations (2.1) and (2.3) can be combined to obtain the general wave equation for piezoelectric materials,

$$c_{ijkl} \frac{\partial^2 U_k}{\partial x_j \partial x_l} - \rho \frac{\partial^2 U_i}{\partial t^2} = - e_{mij} \frac{\partial^2 \phi}{\partial x_m \partial x_j} \quad . \tag{2.4}$$

In the absence of stored charge, the application of the divergence operator to (2.2) gives the general form of Laplace's equation,

$$e_{mkl} \frac{\partial^2 U_k}{\partial x_m \partial x_l} - \epsilon_{mn} \frac{\partial^2 \phi}{\partial x_m \partial x_n} = 0 \; , \tag{2.5}$$

since $e_{mkl} = e_{mlk}$[49].

The desired solutions of the equations (2.4) and (2.5) are "straight crested" in the sense that the planes of constant phase are perpendicular to the propagation vector [k] and the wave amplitudes are independent of distance in the direction perpendicular to the sagittal plane*. In the coordinate system of Fig. 2.2, the propagation vector [k] is parallel to the $x_1 = x$ axis and thus the sagittal plane is the (x,z) plane. Hence, all $\partial U/\partial y = 0$.

The equations (2.4) and (2.5) can then be written as

---

* This results from the assumption that both media are of infinite extent in the (x,y) plane, and no reflecting boundaries exist in the y-direction.

$$\begin{bmatrix} \Gamma_{11}-\rho\frac{\partial^2}{\partial t^2} & \Gamma_{12} & \Gamma_{13} & \Gamma_{14} \\ \Gamma_{12} & \Gamma_{22}-\rho\frac{\partial^2}{\partial t^2} & \Gamma_{23} & \Gamma_{24} \\ \Gamma_{13} & \Gamma_{23} & \Gamma_{33}-\rho\frac{\partial^2}{\partial t^2} & \Gamma_{34} \\ \Gamma_{14} & \Gamma_{24} & \Gamma_{34} & \Gamma_{44} \end{bmatrix} \times \begin{bmatrix} U_1 \\ U_2 \\ U_3 \\ \phi \end{bmatrix} = 0. \quad (2.6)$$

Using contracted matrix notation, the Γ_{ij} are:

$$\Gamma_{11} = c_{11}\frac{\partial^2}{\partial x^2} + 2c_{15}\frac{\partial^2}{\partial x\partial z} + c_{55}\frac{\partial^2}{\partial z^2}$$

$$\Gamma_{22} = c_{66}\frac{\partial^2}{\partial x^2} + 2c_{46}\frac{\partial^2}{\partial x\partial z} + c_{44}\frac{\partial^2}{\partial z^2}$$

$$\Gamma_{33} = c_{55}\frac{\partial^2}{\partial x^2} + 2c_{35}\frac{\partial^2}{\partial x\partial z} + c_{33}\frac{\partial^2}{\partial z^2}$$

$$\Gamma_{12} = c_{16}\frac{\partial^2}{\partial x^2} + (c_{14}+c_{56})\frac{\partial^2}{\partial x\partial z} + c_{45}\frac{\partial^2}{\partial z^2}$$

$$\Gamma_{13} = c_{15}\frac{\partial^2}{\partial x^2} + (c_{55}+c_{13})\frac{\partial^2}{\partial x\partial z} + c_{35}\frac{\partial^2}{\partial z^2}$$

$$\Gamma_{23} = c_{56}\frac{\partial^2}{\partial x^2} + (c_{36}+c_{45})\frac{\partial^2}{\partial x\partial z} + c_{34}\frac{\partial^2}{\partial z^2}$$

$$\Gamma_{14} = e_{11}\frac{\partial^2}{\partial x^2} + (e_{15}+e_{31})\frac{\partial^2}{\partial x\partial z} + e_{35}\frac{\partial^2}{\partial z^2}$$

$$\Gamma_{24} = e_{16}\frac{\partial^2}{\partial x^2} + (e_{14}+e_{36})\frac{\partial^2}{\partial x\partial z} + e_{34}\frac{\partial^2}{\partial z^2}$$

$$\Gamma_{34} = e_{15}\frac{\partial^2}{\partial x^2} + (e_{13}+e_{35})\frac{\partial^2}{\partial x\partial z} + e_{33}\frac{\partial^2}{\partial z^2}$$

$$\Gamma_{44} = -\left[\varepsilon_1\frac{\partial^2}{\partial x^2} + 2\varepsilon_5\frac{\partial^2}{\partial x\partial z} + \varepsilon_3\frac{\partial^2}{\partial z^2}\right] .$$

The equations (2.6) are valid for both substrate and layer materials and circumflexes will be used to denote the layer parameters when necessary. It is assumed that the material tensors for both regions have been rotated to the coordinate system of Fig. 2.2. It will be observed that Maxwell's equations have been ignored in the derivation of equations (2.6). This is based on the assumption that the acoustic wave velocity is much less than that of electromagnetic waves, and thus those waves which propagate with the velocity of light in the material can be ignored[50].

The equations (2.5) are valid in the region external to the transducer, the homogeneous problem, as well as within the transducer region, the inhomogeneous problem. As will be shown, the only difference in these two regions lies in the formulation of the boundary conditions. The homogeneous problem has been considered previously[23], and it has shown that the equations (2.6) lead to an eighth order secular equation in each region. In the substrate, only the four decaying roots are allowed; however, in the layer all eight roots are acceptable because of the finite thickness of this region. Thus, a total of twelve arbitrary constants must be determined from the boundary conditions.

The necessary mechanical boundary conditions for the homogeneous problem include the continuity of the displacements and the traction components of stress (T_{13}, T_{23} and T_{33}) at the interface, as well as the vanishing of the latter stress components at the layer surface[23]. These mechanical requirements provide nine boundary conditions and the remaining three are found in the electrical requirements. These require both the potential and the normal component of the electric displacement vector, D_3, to be continuous at the interface and at the layer surface[23]. In the presence of a metallic plating at either the layer surface or interface, the continuity of D_3 will be replaced by the condition that $E_1 = 0$. These boundary conditions are "homogeneous" and thus the constants evaluated from them lack an absolute scale factor. (The effect of mass loading by the metallic plating will be ignored.)

When solving the inhomogeneous problem within the transducer region the same equations (2.6) are used, as well as the same mechanical boundary conditions. The only changes are in the electrical boundary conditions to account for the presence of the metallic fingers of the transducer (neglecting the mass loading of the fingers). Assuming, for the moment, that the transducer is located at the layer substrate interface, these conditions become:

(1) continuity of D_3 and ϕ at the layer surface, as before

(2) continuity of D_3 and ϕ in the region between the transducer fingers, and $E_1 = 0$ on the fingers.

The presence of a metallic plating on the layer surface would require that $E_1 = 0$ at $z = H$ as in the homogeneous case. These boundary conditions are also "homogeneous" and thus they do not provide an absolute scale factor for the coefficients. This is provided by the additional requirement that the voltage between adjacent electrodes is equal to the applied voltage. When the transducer fingers are driven in a "push-pull" fashion, as is the usual case, this requires that

$$-\int_{n_i L + d/2}^{n_{i-1} L - d/2} E_1(x,0)\,dx = V_o \;;$$

where $n_i L$ and $n_{i-1} L$ represent the location of the centers of adjacent fingers of the ID transducer, with respect to $x = 0$, and V_o is the applied voltage.

In spite of the ease with which one can describe the formulation of the complete inhomogeneous problem, the actual solution is an involved process as a result of the periodic electric boundary conditions. (Periodic as a result of the transducer structure.) Hence, the complete exact solution will not be attempted; rather a simpler, but approximate, problem which can be solved will be considered. This approximate problem could be used as the first step in the solution of the exact problem by an iterative technique.

It is apparent that the equations (2.6) separate into a purely mechanical part and a purely electrical part if the elements of the piezoelectric tensor are zero. The electrical equation is

$$\left(\varepsilon_1 \frac{\partial^2}{\partial x^2} + 2\varepsilon_5 \frac{\partial^2}{\partial x \partial z} + \varepsilon_3 \frac{\partial^2}{\partial z^2}\right)\phi = 0 \,, \tag{2.7}$$

which is the usual form taken by Laplace's equation. In this context, equation (2.7) describes the electric potential function $\phi(x,z)$ of the ID transducer, for a given applied voltage, in the absence of any piezoelectric effects. If one now allows the elements of the piezoelectric tensor to be non-zero, but sufficiently small that they do not affect the solution ϕ of (2.7), the elastic equations of (2.6) can be approximated by

$$\begin{bmatrix} \Gamma_{11} - \rho \frac{\partial^2}{\partial t^2} & \Gamma_{12} & \Gamma_{13} \\ \Gamma_{12} & \Gamma_{22} - \rho \frac{\partial^2}{\partial t^2} & \Gamma_{23} \\ \Gamma_{13} & \Gamma_{23} & \Gamma_{33} - \rho \frac{\partial^2}{\partial t^2} \end{bmatrix} \times \begin{bmatrix} U_1 \\ U_2 \\ U_3 \end{bmatrix} = \begin{bmatrix} \theta_1 \\ \theta_2 \\ \theta_3 \end{bmatrix} , \tag{2.8}$$

where

$$\theta_1 = -\Gamma_{14}\phi, \quad \theta_2 = -\Gamma_{24}\phi, \quad \theta_3 = -\Gamma_{34}\phi \,.$$

Equations (2.7) and (2.8) describe the essence of the "low coupling approximation". It is assumed that the electric potential function of the transducer can be separated and solved independently of the elastic equations, and then used as the forcing term in the inhomogeneous elastic equations. One is thus considering the effect of the electric potential upon the elastic waves, but not the reverse. When solving the homogeneous problem only, the right-hand side of equations (2.8) is identically zero.

From this point on we shall assume the "low coupling approximation". Equation (2.7) will be used to describe the electric potential function, associated with the ID transducer, which is used as the driving term in the elastic equations (2.8). Since the low coupling approximation has separated the inhomogeneous problem into two parts, only electrical boundary conditions are used in the solution of equation (2.7) while only mechanical boundary conditions will appear in the solution of equations (2.8).

2.1.4 Applied Potential Function of the Transducer

In the work to follow, it will be assumed that the ID transducer is located at the layer-substrate interface, with or without a metallic plating on the free surface; however, this is not a restriction on the analysis as such. By suitable alteration of the electric potential function of the transducer, it can also be located, from an analysis standpoint, on the free surface with or without a conducting plate at the interface. The analysis of this paper has been performed in such a way as to allow all of these configurations to be considered.

As observed in section 2.1.1, the most common method of excitation is to drive the fingers of the ID transducer in a push-pull fashion, although the fingers can also be operated in phase. In the work of Cermak et al.[12,24], these drive schemes are referred to as "bipolar" and "unipolar", respectively.

Several authors have recently published "closed form" solutions of equation (2.7) for an ID transducer located on the free surface of a dielectric non-piezoelectric medium with the restriction that $\epsilon_{13} = \epsilon_5 = 0$[19,36,68]. The more involved problem of determining the field of such a transducer located at the interface of an infinitely thick substrate and a layer of finite thickness is not as easily solved. Nevertheless, the solution of equation (2.7) for such a situation ($\epsilon_5 = 0$ in both regions) is a problem which can be handled by numerical methods using a high speed digital computer with a "boundary relaxation" technique[12,24]. Cermak et al. have prepared a computer program, known as "CAPAX"*, which assumes an ID transducer of infinite extent along the x-axis located at the interface of a finite layer and an infinite substrate[12]. The value of the electric potential, resulting from an applied voltage, is calculated at every point on a grid which occupies the region shown in Fig. 2.4. This grid consists of mesh points equally spaced along the x and z axes and symmetry allows it to be extended along the x-axis to cover as many fingers as desired.

Once the potential has been calculated at every point on the grid, it can be expanded in a Fourier series along the x-axis at every level of the grid on the z-axis. In this fashion it is possible to write the potential function for such an array as**

$$\Phi(x,z_i) = \sum_n A_n \delta_n(z_i) \cos(n\pi x/L) \quad . \qquad (2.9a)$$

The potential is an even function of "x" as a result of the assumption that the origin is located at the center of a finger. The functions

---

* ASIS-NAPS Document No. NAPS-00700.

** For "bipolar" drive, n=1,3,5, ... ; for "unipolar" drive, n=2,4,6, ...

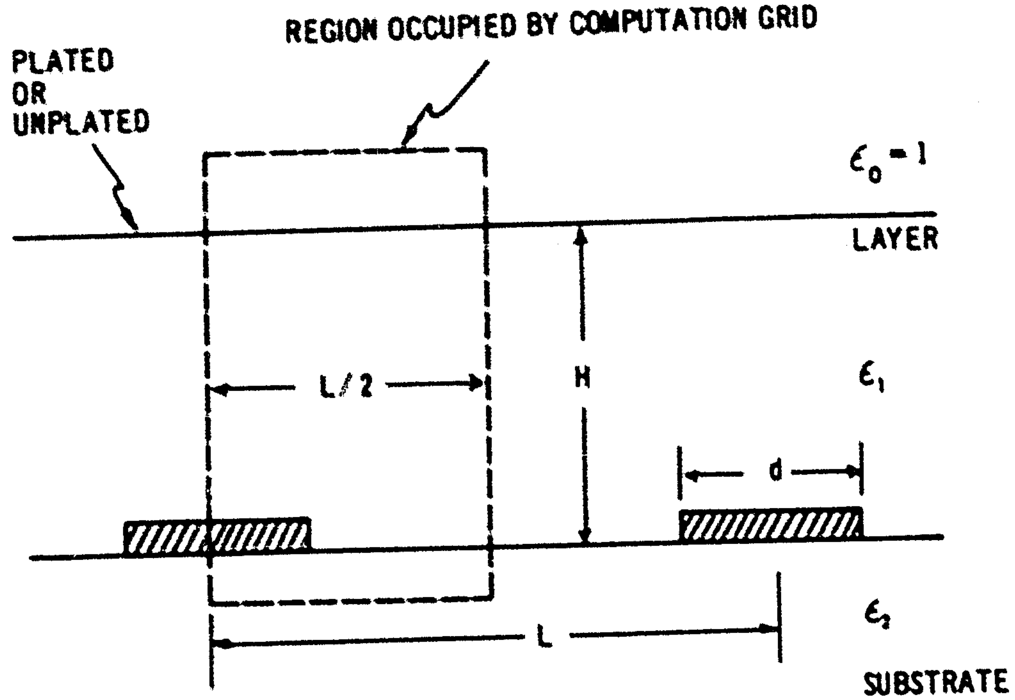
REGION OCCUPIED BY COMPUTATION GRID
PLATED
OR
UNPLATED
$\epsilon_0 = 1$
LAYER
L/2
H
ϵ_1
d
L
ϵ_2
SUBSTRATE

Figure 2.4

$\delta_n(z_i)$ are "discrete", and are defined by the numbers

$$\delta_n(z_1),\ \delta_n(z_2), \ldots\ldots,\ \delta_n(z_M)\ ;$$

which are the Fourier coefficients of the n^{th} harmonic at the level z_i on the grid, normalized to the constant A_n. There are M levels on the grid. As will be shown in Appendix B.1, it is possible to derive a continuous set of functions $f_n(z)$ which agree with the discrete functions $\delta_n(z_i)$ at every level of the grid, so that (2.9a) can be written

$$\phi(x,z) = \sum_n A_n f_n(z) \cos(n\pi x/L) \quad . \tag{2.9b}$$

Equation (2.9b) is derived for a transducer of infinite extent and for a transducer of finite length it is necessary to modify (2.9b) in a suitable manner to obtain the proper driving term for equations (2.8). There are various possible modifications; however, if one assumes a transducer of "reasonable length", the simplest is to define a transducer potential function $\phi(x,z)$ by[36]

$$\phi(x,z) = \begin{cases} \sum_n A_n f_n(z) \cos(n\pi x/L), & |x| < D/2 \\ 0, & |x| > D/2 \end{cases} \quad . \tag{2.10}$$

(It is possible to extend the potential function ϕ in a continuous fashion for $|x| > D/2$; however, this adds considerably to the mathematical complexity and actual computations indicate that it will not appreciably alter the final result*.)

Equation (2.10) can be used to describe the potential function $\phi(x,z)$ for both layer and substrate, on the assumption that $\varepsilon_3 = 0$ in both

---

* This point is considered in Chapter VII, section 7.4.

regions, and is applicable to any of the transducer configurations previously mentioned, only the harmonic content and the terms A_n and $f_n(z)$ will change. In Appendix B.2, the means of determining the harmonic content, as well as A_n and $f_n(z)$, for the different transducer configurations will be discussed. At this juncture the actual form of the functions $f_n(z)$ is unimportant; it is sufficient to know that they can be derived when required.

As shown in Nye[A9], the only materials with non-diagonal dielectric tensors are those of the triclinic and monoclinic systems, both of which are very anisotropic. Because of their high degree of anisotropy, materials of these two classes are usually of only academic interest and are not used in the fabrication of actual surface wave devices. Hence, we can assume, with reasonable certainty, that the materials to be analyzed will have only diagonal dielectric tensors and the restriction applied to ϵ_3 is a reasonable one.

The "CAPAX" program imposes two additional restrictions on the solution of equation (2.7), neither of which is serious:

(1) It cannot calculate the potential function for layer thickness, H, in the range $0 < H < 0.5\ L$; and, for reasonable computational accuracy, the layer thickness, H, must be equal to an integral number of steps on the computational grid; also,

(2) it assumes that the materials are dielectrically isotropic.

The first restriction does not affect the theoretical derivations to follow, only the computation of actual results, and arises from the finite mesh size used in the calculations. Zero layer thickness does not present any problems. The second restriction requires some form of "averaging" of the elements of the dielectric tensor to obtain an effective isotropic value for the materials. With $\varepsilon_5 = 0$, the only elements to be "averaged" are ε_1 and ε_3. The "averaging" can be done in several ways, and the method to be used in this thesis is to define an isotropic dielectric constant for each of the materials as the geometric mean of the appropriate ε_1 and ε_3[2]. Thus,

$$\varepsilon_{\text{isotropic}} = (\varepsilon_1 \varepsilon_3)^{\frac{1}{2}} .$$

A method of correcting the potential function calculated by "CAPAX" for the isotropic dielectric assumption is described in Appendix B.3.

2.1.5 Outline of the Method of Solution

The solution of the inhomogeneous layer problem for materials with general symmetry is an extremely involved process, even with the "low coupling approximation". However, by applying some minor restrictions to the symmetry of the materials to be analyzed, the task can be considerably simplified. The restrictions to be made in the following sections will restrict the analysis to those materials in which the direction of surface wave energy flow is along the x-axis. The solutions thus obtained can be used as a guide for other cases, or the general case if so desired.

It will be assumed that both layer and substrate are piezoelectric, and thus a large number of the equations in the theory will be valid for both regions. When this situation occurs, the equation in question will not be written out in duplicate; instead, it will be indicated that the equation is valid for both regions and different notations will be used where necessary.

The steps which are involved in the solution of the "inhomogeneous layer problem" can be outlined as follows:

(1) derivation of the inhomogeneous wave equations with the "low coupling approximation" (2.1.3)

(2) derivation of the electric potential function (low coupling) (2.1.4 and Appendix B)

(3) derivation of the inhomogeneous wave equations with symmetry considerations (low coupling) (2.2.1)

(4) application of the one-dimensional Fourier transform to the wave equations (this follows the method of Joshi and White[3]*, as well as that of Miller and Pursey[4]*) (2.2.2)

(5) solution of the transformed homogeneous equations (2.2.3)

(6) derivation of the transformed "particular integral" solutions to the inhomogeneous equations (2.2.4)

(7) statement of the transformed boundary conditions and the solution of the resulting equations (2.2.5)

(8) application of the inverse Fourier transform (2.2.6).

2.1.6 Summary

In this section we have introduced the interdigital (ID) transducer and the coordinate system to be used. The "low coupling approximation" has been applied to the general equations of motion and the set of equations (2.7) and (2.9), which describe this approximation, have been derived. The potential function which is a solution of the low coupling electrostatic problem has been determined and the steps required to solve the inhomogeneous problem have been outlined.

2.2 Low Coupling Inhomogeneous Problem

2.2.1 Application of Symmetry Considerations

In section 2.1.3 the "low coupling" wave equations (2.8) were derived, and it is these equations which will be used to obtain solutions to the "inhomogeneous layer problem":

$$\begin{bmatrix} \Gamma_{11}-\rho\frac{\partial^2}{\partial t^2} & \Gamma_{12} & \Gamma_{13} \\ \Gamma_{12} & \Gamma_{22}-\rho\frac{\partial^2}{\partial t^2} & \Gamma_{23} \\ \Gamma_{13} & \Gamma_{23} & \Gamma_{33}-\rho\frac{\partial^2}{\partial t^2} \end{bmatrix} \times \begin{bmatrix} U_1 \\ U_2 \\ U_3 \end{bmatrix} = \begin{bmatrix} \theta_1 \\ \theta_2 \\ \theta_3 \end{bmatrix} . \quad (2.8)$$

The electric potential function of the ID transducer ϕ, which appears in the terms $[\theta_i]$, was derived in section 2.1.4 and is given by equation (2.10):

$$\phi = \begin{cases} \sum_n A_n f_n(z) \cos(n\pi x/L), & |x| < D/2 \\ 0 \quad |x| > D/2 \end{cases} . \quad (2.10)$$

The equations (2.8) can be used to obtain the wave solutions for the general symmetry case; however, it is possible to make some simplifying assumptions which do not seriously restrict the usefulness of these equations. In most surface wave devices it is desirable that the direction of surface wave energy flow be along the x-axis, for this is the direction in which the wave is launched by the ID transducer. In this situation, the x-axis is referred to as a "pure mode axis" for surface waves; and requires that the elements

c_{16}, c_{14}, c_{56}, c_{36}, c_{34}, c_{45} (matrix notation)

of the stiffness tensor be equal to zero in our coordinate system. Most of those materials which are used for surface wave devices can be oriented in such a way as to allow this restriction on the c_{kl}. From a piezoelectric standpoint, only those materials for which the elements

$$e_{16},\ e_{14},\ e_{36},\ e_{34}\ \text{(matrix notation)}$$

of the piezoelectric tensor are always zero, in our reference frame, will be considered. (Those elements of the form e_{2j} were dropped in the derivation of (2.8) since $\partial\phi/\partial y = 0$.) The latter assumption on the e_{ij} eliminates both Love[43] and Bleustein[9] waves from the analysis. Thus, the analysis is restricted to those waves which have displacements in the sagittal plane only.

With the application of these additional assumptions, one finds that

$$\Gamma_{12} = \Gamma_{23} = \theta_2 = 0$$

and the equations (2.8) can be reduced to

$$\begin{bmatrix} \Gamma_{11} - \rho \frac{\partial^2}{\partial t^2} & 0 & \Gamma_{13} \\ 0 & \Gamma_{22} - \rho \frac{\partial^2}{\partial t^2} & 0 \\ \Gamma_{13} & 0 & \Gamma_{33} - \rho \frac{\partial^2}{\partial t^2} \end{bmatrix} \times \begin{bmatrix} U_1 \\ U_2 \\ U_3 \end{bmatrix} = \begin{bmatrix} \theta_1 \\ 0 \\ \theta_3 \end{bmatrix} . \qquad (2.11)$$

It can be seen that the U_2 displacement is uncoupled from the others and, in the absence of a θ_2 driving term, it will not be excited. Thus, the U_2 displacement is of no further use and it can be dropped. The equations (2.11) can then be written

$$\begin{bmatrix} \Gamma_{11} - \rho \frac{\partial^2}{\partial t^2} & \Gamma_{13} \\ \Gamma_{13} & \Gamma_{33} - \rho \frac{\partial^2}{\partial t^2} \end{bmatrix} \times \begin{bmatrix} U_1 \\ U_3 \end{bmatrix} = \begin{bmatrix} \theta_1 \\ \theta_3 \end{bmatrix} . \qquad (2.12)$$

As was observed in section 2.1.3, the exclusion of Maxwell's equations in the derivation of equations (2.6) is an implicit assumption that the mechanical wave velocity is much less than that for electromagnetic waves in the medium. Therefore, it is reasonable to assume that a time dependence $\exp(-i\omega t)$ can be used for both the U_j and the θ_j throughout the regions of interest. The operator $-\rho\partial^2/\partial t^2$ can then be written $\rho\omega^2$, and both the U_j and θ_j become functions of the spatial variables only. This is known as the "quasi-static approximation".

The equations (2.12) are valid for both the layer and substrate, with the substitution of the appropriate elastic and piezoelectric elements. If either layer or substrate is non-piezoelectric, the right hand side of equation (2.12) for that particular region, will be identically zero.

2.2.2 Application of the One-Dimensional Fourier Transform

Following the method of Joshi and White[36], as well as that of Miller and Pursey[46], consider the one-dimensional Fourier transform given by

$$P(k) = \int_{-\infty}^{\infty} p(x)e^{-ikx}dx \quad , \qquad (2.13)$$

where k must be real to insure the convergence of the integral at infinity[59]. The inverse Fourier transform is then given by

$$p(x) = \left(\frac{1}{2\pi}\right) \int_{-\infty}^{\infty} P(k)e^{ikx}dk \quad , \qquad (2.14)$$

where the range of integration is along the real axis[59].

If the transform, defined by (2.13), is applied to the equations (2.12), the variable "x" is eliminated, giving the equations

$$\begin{bmatrix} y_{11} & y_{12} \\ y_{12} & y_{22} \end{bmatrix} \times \begin{bmatrix} \overline{U}_1 \\ \overline{U}_3 \end{bmatrix} = \begin{bmatrix} \overline{\theta}_1 \\ \overline{\theta}_3 \end{bmatrix} \quad . \qquad (2.15)$$

The bar, "-", appearing over a variable implies that it is the variable in (k,z) space. As is shown in Appendix A, the elements of (2.15) are defined by:

$$Y_{11} = c_{55}\frac{\partial^2}{\partial z^2} + 2c_{15}\,ik\frac{\partial}{\partial z} - c_{11}k^2 + \rho\omega^2$$

$$Y_{22} = c_{33}\frac{\partial^2}{\partial z^2} + 2c_{35}\,ik\frac{\partial}{\partial z} - c_{55}k^2 + \rho\omega^2$$

$$Y_{12} = c_{35}\frac{\partial^2}{\partial z^2} + (c_{55} + c_{13})ik\frac{\partial}{\partial z} - c_{15}k^2$$

$$\bar{\theta}_1 = -\left[e_{35}\frac{\partial^2}{\partial z^2} + (e_{15} + e_{31})ik\frac{\partial}{\partial z} - k^2e_{11}\right]\bar{\phi}$$

$$+ \left[2ie_{15}\frac{\partial}{\partial z} - 2ke_{11}\right]\phi(D/2)\sin(k\,D/2)$$

$$\bar{\theta}_3 = -\left[e_{33}\frac{\partial^2}{\partial z^2} + (e_{13} + e_{35})ik\frac{\partial}{\partial z} - k^2e_{15}\right]\bar{\phi}$$

$$+ \left[2ie_{13}\frac{\partial}{\partial z} - 2ke_{15}\right]\phi(D/2)\sin(k\,D/2) \;;$$

where:

$$\bar{U}_j = \bar{U}_j(k,z), \quad \bar{\phi} = \bar{\phi}(k,z) = \sum_n A_nF_n(k)f_n(z)$$

$$F_n(k) = \frac{\sin[(k - n\,\pi/L)D/2]}{(k - n\,\pi/L)} + \frac{\sin[(k + n\,\pi/L)D/2]}{(k + n\,\pi/L)}$$

$$\phi(D/2) = \phi(D/2,z) = \sum_n A_nN_nf_n(z)$$

$$N_n = \begin{cases} -1, & \text{if } n+m_o \text{ is odd} \\ 1, & \text{if } n+m_o \text{ is even} \end{cases}$$

$D/2 = m_oL$, 'm_o' is an integer .

The terms involving sin(kD/2) appear because the potential function, ϕ, as defined by (2.10), is not a continuous function of x at $|x| = D/2$.

Equations (2.15) are the transformed, low-coupling wave equations which are valid in both the layer and substrate, with appropriate values of the c_{ij} and the e_{kl}. These equations, (2.15), are differential equations in the variable "z" and, in general, the solution will consist of a solution to the homogeneous form of (2.15) plus a particular solution to the inhomogeneous equations, often referred to as the "particular integral" solution.

The application of the Fourier transform,(2.13), to the wave equations,(2.12),is not a superfluous step, as it might appear. Without this step it would still be possible to solve the equations (2.12), however, the process would become much more involved. Without the transformation, homogeneous solutions in the two regions $|x| > D/2$ $(\theta_1 = \theta_3 = 0)$ would have to be obtained in addition to the solutions for the region $|x| < D/2$. These three separate sets of solutions must each satisfy the usual mechanical boundary conditions at the interface and free surface, in addition to being matched at the boundaries, $x = \pm D/2$. This would result in a total of thirty-four boundary condition equations! By applying the Fourier transform in the proper fashion, the necessary continuity at $x = \pm D/2$ has been assured and the mechanical boundary conditions at the interface and free surface, in the three separate regions, have been combined.

2.2.3 Homogeneous Solutions

The homogeneous solutions to the equations (2.15) are obtained by setting the right hand side of the equations equal to zero, and assuming a trial solution of the form

$$\bar{U}_j^{II} = a_j e^{iklz} .$$

Substituting this solution into the homogeneous form of equation (2.15) yields

$$\begin{bmatrix} (c_{55}l^2 + 2c_{15}l + c_{11} - \rho\omega^2/k^2) & (c_{35}l^2 + (c_{55} + c_{13})l + c_{15}) \\ (c_{35}l^2 + (c_{55} + c_{13})l + c_{15}) & (c_{33}l^2 + 2c_{35}l + c_{55} - \rho\omega^2/k^2) \end{bmatrix} \times \begin{bmatrix} a_1 \\ a_3 \end{bmatrix} = 0 . \quad (2.16)$$

To avoid trivial solutions for a_1 and a_3, it is necessary that the determinant of the equations (2.16) vanish. This requirement gives the so-called "secular equation" which is valid for either layer or substrate, with the appropriate values of the c_{kl}:

$$\begin{aligned} &(c_{55}c_{33} - c_{35}^2)l^4 + 2(c_{15}c_{33} - c_{35}c_{13})l^3 \\ &+[c_{11}c_{33} + c_{55}^2 + 2c_{15}c_{35} - (c_{55} + c_{13})^2 - (c_{33} + c_{55})(\rho\omega^2/k^2)]l^2 \\ &+2[c_{11}c_{35} - c_{15}c_{13} - (c_{35} + c_{15})(\rho\omega^2/k^2)]l \\ &+[c_{11}c_{55} - c_{15}^2 - (c_{55} + c_{11})(\rho\omega^2/k^2) + (\rho\omega^2/k^2)^2] = 0 \quad . \end{aligned} \quad (2.17)$$

For a given ω, this equation is quartic in l, with the parameter k. In general, there will exist four roots and since the coefficients are real, any complex root will appear in conjugate pairs. The roots l_m can be considered "eigenvalues" of the homogeneous form of equations (2.15) and the functions e^{ikl_mz} as the "eigenfunctions" of the homogeneous problem. Associated with each "eigenvalue" there is an "eigenvector",

$$\begin{bmatrix} a_{1_m} \\ a_{3_m} \end{bmatrix} ,$$

which can be determined from either of the equations (2.16). The complete transformed homogeneous solutions can then be written

$$\bar{U}_j^H = \sum C_m \alpha_{jm} e^{ikl_m z},$$

where the C_m are, as yet, arbitrary constants.

Since the solutions to the inhomogeneous equations represent the "far field" or propagating solutions, it is necessary to impose the surface wave condition that the solutions in the substrate vanish as $z \to -\infty$. Thus, the substrate roots l_m with positive imaginary parts must be discarded for $k > 0$, and those with negative imaginary parts for $k < 0$*. Therefore, one is left with only two valid "eigenfunctions" for the homogeneous solutions in the substrate, at a particular value of k. All four "eigenfunctions" are valid in the layer, due to the finite thickness of this region.

To avoid future confusion, it is best to number the roots l_m so that it will be clear whether the layer or substrate solutions are being discussed. Those roots in the substrate are l_1 and l_2, while the four roots in the layer are $l_3, \ldots, l_6$. Introducing the notation $\bar{W}_j^H$ and $\bar{U}_j^H$, to refer to the transformed homogeneous solutions in the substrate and layer, respectively, one can write:

$$\begin{aligned}
\bar{W}_1^H &= \sum_{m=1}^{2} C_m \alpha_{1m} e^{ikl_m z} \\
\bar{W}_3^H &= \sum_{m=1}^{2} C_m \alpha_{3m} e^{ikl_m z} \\
\bar{U}_1^H &= \sum_{m=3}^{6} C_m \alpha_{1m} e^{ikl_m z} \\
\bar{U}_3^H &= \sum_{m=3}^{6} C_m \alpha_{3m} e^{ikl_m z}
\end{aligned} \qquad (2.18)$$

.

---

* 'k' is purely real at this juncture.

The evaluation of the C_m will be considered in section 2.2.5.

2.2.4 Determination of the Particular Integral Solution

The particular integral solution to an inhomogeneous differential equation is that solution which can be found to satisfy the given equation and is not a solution of the homogeneous equation. In the physical sense, the particular integral solution represents the response of the system to a given "forcing function" and usually is damped out with either time or distance. This solution is usually functionally related to the "forcing function". In our case, solutions which satisfy the set of equations (2.15) are required. As shown in section 2.2.2, the functions $\bar{\phi}$ and $\phi(D/2)$, which appear on the right hand side of the equations (2.15), are represented by a summation of terms. Thus, it is logical to look for a particular integral solution which is represented by a summation consisting of the same number of terms:

$$\bar{U}_1^P = \sum_n \bar{U}_{1n}^P$$

$$\bar{U}_3^P = \sum_n \bar{U}_{3n}^P \quad .$$

Since the differential operators of (2.15) are linear, they can be applied to each term of the solutions $\bar{U}_j^P$ and the right hand side separately[37]. Thus, it is possible to write equation (2.15) for the n^{th} term of the solutions $\bar{U}_j^P$ as

$$\begin{bmatrix} Y_{11} & Y_{12} \\ Y_{12} & Y_{22} \end{bmatrix} \times \begin{bmatrix} \bar{U}_{1n}^P \\ \bar{U}_{3n}^P \end{bmatrix} = \begin{bmatrix} \bar{\theta}_1 \\ \bar{\theta}_{3n} \end{bmatrix} \; ; \qquad (2.19)$$

where:

$$\bar{a}_{1_n} = -\left[e_{35}\frac{\partial^2}{\partial z^2} + (e_{15}+e_{31})ik\frac{\partial}{\partial z} - k^2 e_{11}\right]\bar{\phi}_n$$
$$+\left[2ie_{15}\frac{\partial}{\partial z} - 2ke_{11}\right]\phi_n(D/2)\sin(k\,D/2)$$

$$\bar{a}_{3_n} = -\left[e_{33}\frac{\partial^2}{\partial z^2} + (e_{13}+e_{35})ik\frac{\partial}{\partial z} - k^2 e_{15}\right]\bar{\phi}_n$$
$$+\left[2ie_{13}\frac{\partial}{\partial z} - 2ke_{15}\right]\phi_n(D/2)\sin(k\,D/2)\ .$$

The terms $\bar{\phi}_n$ and $\phi_n(D/2)$ are the n^{th} terms of the summations for $\bar{\phi}$ and $\phi(D/2)$, respectively. The right hand side of (2.19) consists of two general terms, one involving $\bar{\phi}_n$ and one with $\phi_n(D/2)$. Thus, the n^{th} term of the solutions can be further divided, and one can write:

$$\bar{U}_{1_n}^{p} = R_{1_n} + S_{1_n}$$
$$\bar{U}_{3_n}^{p} = R_{3_n} + S_{3_n}\quad .$$

Where the terms R_{jn} are solutions of the equations

$$\begin{bmatrix} y_{11} & y_{12} \\ y_{12} & y_{22} \end{bmatrix} \times \begin{bmatrix} R_{1_n} \\ R_{3_n} \end{bmatrix} = \begin{bmatrix} -\left[e_{35}\frac{\partial^2}{\partial z^2} + ik(e_{15}+e_{31})\frac{\partial}{\partial z} - e_{11}k^2\right] \\ -\left[e_{33}\frac{\partial^2}{\partial z^2} + ik(e_{13}+e_{35})\frac{\partial}{\partial z} - e_{15}k^2\right] \end{bmatrix}\bar{\phi}_n \quad (2.20)$$

and the terms S_{jn} are solutions of

$$\begin{bmatrix} y_{11} & y_{12} \\ y_{12} & y_{22} \end{bmatrix} \times \begin{bmatrix} S_{1_n} \\ S_{3_n} \end{bmatrix} = \begin{bmatrix} 2ie_{15}\frac{\partial}{\partial z} - 2ke_{11} \\ 2ie_{13}\frac{\partial}{\partial z} - 2ke_{15} \end{bmatrix}\phi_n(D/2)\sin(k\,D/2)\,. \quad (2.21)$$

From this point there are numerous methods which can be used to obtain the desired solutions, R_{jn} and S_{jn}; however, before proceeding to that step it is necessary that the functions $f_n(z)$, which appear in both $\overline{\phi}_n$ and $\phi_n(D/2)$, be defined. These functions were introduced briefly in section 2.1.4 and are discussed in considerable detail in Appendix B. It is shown, in Appendix B, that the general form of these functions, applicable to both layer and substrate, is

$$f_n(z) = e^{-M_n z} + r_n e^{M_n z} \quad , \qquad (2.22)$$

where

$$M_n = \pm n\pi\,(\epsilon_1/\epsilon_3)^{\frac{1}{2}}/L \; .$$

The choice of sign for M_n depends on the location of the transducer and the region in question, as shown in Appendix B. The value of r_n for the substrate is zero in all cases; however, when a metallic plating is used, this is not true for the layer. Again, this point is covered in detail in Appendix B. For the purpose of obtaining the solutions R_{jn} and S_{jn}, the most general form of $f_n(z)$, given by (2.22) will be used. In this way, the restrictions which are peculiar to a particular region or transducer configuration can be easily applied to the final result. Using (2.22), $\overline{\phi}_n$ and $\phi_n(D/2)$ can be written:

$$\begin{aligned} \overline{\phi}_n &= A_n F_n(k)\,[e^{-M_n z} + r_n e^{M_n z}] \\ \phi_n\left(\frac{D}{2}\right) &= A_n N_n \quad [e^{-M_n z} + r_n e^{M_n z}] \end{aligned} \quad .$$

One can then assume solutions of the form:

$$R_{jn} = a_{jn} F_n(k) e^{-M_n z} + b_{jn} F_n(k) e^{M_n z}$$

$$S_{jn} = c_{jn} N_n \quad e^{-M_n z} + d_{jn} N_n \quad e^{M_n z} \quad .$$

Substituting the solutions R_{jn} into equation (2.20) and separating the terms, gives two equations:

$$\begin{bmatrix} \Delta_{11} & \Delta_{12} \\ \Delta_{12} & \Delta_{22} \end{bmatrix} \times \begin{bmatrix} a_{1n} \\ a_{3n} \end{bmatrix} = - \begin{bmatrix} \delta_1 \\ \delta_2 \end{bmatrix} A_n \qquad (2.23a)$$

and

$$\begin{bmatrix} \Delta_{11} & \Delta_{12} \\ \Delta_{12} & \Delta_{22} \end{bmatrix} \times \begin{bmatrix} b_{1n} \\ b_{3n} \end{bmatrix} = - \begin{bmatrix} \delta_1 \\ \delta_2 \end{bmatrix} A_n r_n \; ; \qquad (2.23b)$$

where:

$$\Delta_{11} = c_{33} M_n^2 (\mp) 2c_{13} ikM_n - c_{11} k^2 + \rho\omega^2$$

$$\Delta_{12} = c_{33} M_n^2 (\mp) (c_{33} + c_{13}) ikM_n - c_{13} k^2$$

$$\Delta_{22} = c_{33} M_n^2 (\mp) 2c_{33} ikM_n - c_{33} k^2 + \rho\omega^2$$

$$\delta_1 = e_{33} M_n^2 (\mp) (e_{13} + e_{31}) ikM_n - c_{11} k^2$$

$$\delta_2 = e_{33} M_n^2 (\mp) (e_{13} + e_{33}) ikM_n - c_{13} k^2 \; .$$

The minus sign is used in equation (2.23a) while the plus sign is used in (2.23b).

The substitution of the solutions S_{jn} into (2.21) also gives two equations:

$$\begin{bmatrix} \Delta_{11} & \Delta_{12} \\ \Delta_{12} & \Delta_{22} \end{bmatrix} \times \begin{bmatrix} c_{1n} \\ c_{3n} \end{bmatrix} = \begin{bmatrix} \delta_1' \\ \delta_2' \end{bmatrix} A_n N_n \qquad (2.24a)$$

and

$$\begin{bmatrix} \Delta_{11} & \Delta_{12} \\ \Delta_{12} & \Delta_{22} \end{bmatrix} \times \begin{bmatrix} d_{1n} \\ d_{3n} \end{bmatrix} = \begin{bmatrix} \delta_1' \\ \delta_2' \end{bmatrix} A_n N_n r_n \; . \qquad (2.24b)$$

The Δ_{kl} are the same as defined above, with the same alternation of sign for equation (2.24a) and (2.24b). The terms, δ_k', are defined by

$$\delta_1' = \left[(\mp) \; 2ie_{13} M_n - 2ke_{11} \right]$$

and

$$\delta_2' = \left[(\mp) \; 2ie_{13} M_n - 2kc_{13} \right] ,$$

with the same alternation of sign as the other terms.

The equations (2.23) can be solved for the term a_{jn} and b_{jn}, while equations (2.24) can be solved for the c_{jn} and d_{jn}. The solutions R_{jn} and S_{jn} can then be written:

$$R_{jn} = a_{jn} P_n(k) \left[e^{-M_n z} + Y_{jn} e^{M_n z} \right] \tag{2.25a}$$

$$S_{jn} = c_{jn} \sin (k\ D/2) \left[e^{-M_n z} + X_{jn} e^{M_n z} \right] ; \tag{2.25b}$$

where:

$$Y_{jn} = (b_{jn}/a_{jn})$$
$$X_{jn} = (d_{jn}/c_{jn}) \quad .$$

The particular integral solutions are then defined by

$$\overline{U}_j^P = \sum_n \left\{ P_n(k) \left[a_{jn} \left(e^{-M_n z} + Y_{jn} e^{M_n z} \right) \right] \right.$$
$$\left. + \sin k\ D/2 \left[c_{jn} \left(e^{-M_n z} + X_{jn} e^{M_n z} \right) \right] \right\} \quad . \tag{2.26}$$

From a computational standpoint, it is useful to observe that, if

$$a_{jn} = G(k) A_n \quad \text{and} \quad c_{jn} = H(k) A_n N_n$$

then

$$Y_{in} = (G^*/G) r_n \quad \text{and} \quad X_{jn} = (H^*/H) r_n$$

from equations (2.23) and (2.24). (Where '*' implies the complex conjugate.)

It will be observed, from equations (2.23) and (2.24), that there is the possibility that values of k will exist for which the left hand side of equations (2.23) and (2.24) will vanish. This does not mean, however, that the particular integral solutions do not exist at these values of k, merely that the form of the particular integral solution which has been chosen does not satisfy the equations (2.20) and (2.21). This situation occurs at those values of k for which the term $e^{\pm M_n z}$ is a solution of the homogeneous problem. The problem is eliminated by returning to the equations (2.20) and (2.21) and assuming new trial solutions of the form[13]

$$R_{jn} = z\left[a_{jn}P_n(k)e^{-M_n z} + b_{jn}P_n(k)e^{M_n z}\right]$$

and

$$S_{jn} = z\left[c_{jn}N_n e^{-M_n z} + d_{jn}N_n e^{M_n z}\right] .$$

It is worthwhile observing that the left hand side of equations (2.23) and (2.24) will vanish for k real only if $c_{15} = c_{35} = 0$.

2.2.5 Solution of the Boundary Condition Problem

It is now possible to determine the coefficients C_m of the homogeneous solutions (2.18) from the boundary conditions. Since the C_m are six in number, it is necessary to have a set of six boundary condition equations. Since the electrical boundary conditions have been eliminated in the "low coupling approximation", these equations are easily found in the mechanical restrictions on the problem:

(1) continuity of the displacements at the interface

(2) continuity of T_{33} and T_{13} at the interface

(3) $T_{33} = T_{13} = 0$, at the surface of the layer (free surface).

These conditions can be written as:

$$U_1(x,0) = W_1(x,0) \tag{2.27a}$$

$$U_3(x,0) = W_3(x,0) \tag{2.27b}$$

$$\hat{T}_3(x,0) = T_3(x,0) \tag{2.27c}$$

$$\hat{T}_5(x,0) = T_5(x,0) \tag{2.27d}$$

$$\hat{T}_3(x,H) = 0 \tag{2.27e}$$

$$\hat{T}_5(x,H) = 0 \quad , \tag{2.27f}$$

where the stresses are given in matrix notation[*]. The terms U_j and W_j represent the total solutions (homogeneous + particular integral) in the layer and substrate, respectively, while the superscript "^" refers to those terms evaluated in the layer, as mentioned previously.

Applying the Fourier transform of equation (2.13) to the equations (2.27) yields the transformed boundary condition equations:

$$\bar{U}_1(k,0) = \bar{W}_1(k,0) \tag{2.28a}$$

$$\bar{U}_3(k,0) = \bar{W}_3(k,0) \tag{2.28b}$$

$$\hat{\bar{T}}_3(k,0) = \bar{T}_3(k,0) \tag{2.28c}$$

$$\hat{\bar{T}}_5(k,0) = \bar{T}_5(k,0) \tag{2.28d}$$

$$\hat{\bar{T}}_3(k,H) = 0 \tag{2.28e}$$

$$\hat{\bar{T}}_5(k,H) = 0 \quad . \tag{2.28f}$$

The $\bar{T}_j$ can be determined by application of the Fourier transform of (2.13) to equation (2.1) in the manner shown in Appendix A. Substitution of the transformed wave solutions (homogeneous + particular integral) into equations (2.28) gives the following set of equations:

$$\sum_{m=1}^{2} \alpha_{1m} C_m - \sum_{m=3}^{6} \alpha_{1m} C_m = \left[\bar{U}_1^P - \bar{W}_1^P \right]_{z=0} \tag{2.29a}$$

---

[*] The equations (2.27) represent the boundary conditions for a "rigid" bond between layer and substrate, the most common case. The case of a "smooth" or "sliding" bond is considered in Appendix E.

$$\sum_{m=1}^{2} \alpha_{3m} C_m - \sum_{m=3}^{6} \alpha_{3m} C_m = \left[\bar{U}_3^P - \bar{W}_3^P \right]_{z=0} \tag{2.29b}$$

$$\begin{aligned}
&\sum_{m=1}^{2} ik \left\{ \begin{matrix} [c_{13} + c_{35} l_m]\alpha_{1m} \\ +[c_{35} + c_{33} l_m]\alpha_{3m} \end{matrix} \right\} C_m - \sum_{m=3}^{6} ik \left\{ \begin{matrix} [\hat{c}_{13} + \hat{c}_{35} l_m]\alpha_{1m} \\ +[\hat{c}_{35} + \hat{c}_{33} l_m]\alpha_{3m} \end{matrix} \right\} C_m = \\
&\left[\hat{c}_{13} \bar{U}_1^P ik + \hat{c}_{35} \frac{\partial \bar{U}_1^P}{\partial z} + \hat{c}_{35} \bar{U}_3^P ik + \hat{c}_{33} \frac{\partial \bar{U}_3^P}{\partial z} + \hat{e}_{13} \hat{\bar{\phi}} ik + \hat{e}_{33} \frac{\partial \hat{\bar{\phi}}}{\partial z} - 2i\hat{e}_{13} \hat{\phi}(D/2) \sin(kD/2) \right]_{z=0} \\
&- \left[c_{13} \bar{W}_1^P ik + c_{35} \frac{\partial \bar{W}_1^P}{\partial z} + c_{35} \bar{W}_3^P ik + c_{33} \frac{\partial \bar{W}_3^P}{\partial z} + e_{13} \bar{\phi} ik + e_{33} \frac{\partial \bar{\phi}}{\partial z} - 2ie_{13} \phi(D/2) \sin(kD/2) \right]_{z=0}
\end{aligned} \tag{2.29c}$$

$$\begin{aligned}
&\sum_{m=1}^{2} ik \left\{ \begin{matrix} [c_{15} + c_{55} l_m]\alpha_{1m} \\ +[c_{55} + c_{35} l_m]\alpha_{3m} \end{matrix} \right\} C_m - \sum_{m=3}^{6} ik \left\{ \begin{matrix} [\hat{c}_{15} + \hat{c}_{55} l_m]\alpha_{1m} \\ +[\hat{c}_{55} + \hat{c}_{35} l_m]\alpha_{3m} \end{matrix} \right\} C_m = \\
&\left[\hat{c}_{15} \bar{U}_1^P ik + \hat{c}_{55} \frac{\partial \bar{U}_1^P}{\partial z} + \hat{c}_{55} \bar{U}_3^P ik + \hat{c}_{35} \frac{\partial \bar{U}_3^P}{\partial z} + \hat{e}_{15} \hat{\bar{\phi}} ik + \hat{e}_{35} \frac{\partial \hat{\bar{\phi}}}{\partial z} - 2i\hat{e}_{15} \hat{\phi}(D/2) \sin(kD/2) \right]_{z=0} \\
&- \left[c_{15} \bar{W}_1^P ik + c_{55} \frac{\partial \bar{W}_1^P}{\partial z} + c_{55} \bar{W}_3^P ik + c_{35} \frac{\partial \bar{W}_3^P}{\partial z} + e_{15} \bar{\phi} ik + e_{35} \frac{\partial \bar{\phi}}{\partial z} - 2ie_{15} \phi(D/2) \sin(kD/2) \right]_{z=0}
\end{aligned} \tag{2.29d}$$

$$\begin{aligned}
&\sum_{m=1}^{2} ik(0) C_m - \sum_{m=3}^{6} ik \left\{ \begin{matrix} [\hat{c}_{13} + \hat{c}_{35} l_m]\alpha_{1m} \\ +[\hat{c}_{35} + \hat{c}_{33} l_m]\alpha_{3m} \end{matrix} \right\} e^{ikl_m H} C_m = \\
&\left[\hat{c}_{13} \bar{U}_1^P ik + \hat{c}_{35} \frac{\partial \bar{U}_1^P}{\partial z} + \hat{c}_{35} \bar{U}_3^P ik + \hat{c}_{33} \frac{\partial \bar{U}_3^P}{\partial z} + \hat{e}_{13} \hat{\bar{\phi}} ik + \hat{e}_{33} \frac{\partial \hat{\bar{\phi}}}{\partial z} - 2ie_{13} \hat{\phi}(D/2) \sin(kD/2) \right]_{z=H}
\end{aligned} \tag{2.29e}$$

$$\begin{aligned}
&\sum_{m=1}^{2} ik(0) C_m - \sum_{m=3}^{6} ik \left\{ \begin{matrix} [\hat{c}_{15} + \hat{c}_{55} l_m]\alpha_{1m} \\ +[\hat{c}_{55} + \hat{c}_{35} l_m]\alpha_{3m} \end{matrix} \right\} e^{ikl_m H} C_m = \\
&\left[\hat{c}_{15} \bar{U}_1^P ik + \hat{c}_{55} \frac{\partial \bar{U}_1^P}{\partial z} + \hat{c}_{55} \bar{U}_3^P ik + \hat{c}_{35} \frac{\partial \bar{U}_3^P}{\partial z} + \hat{e}_{15} \hat{\bar{\phi}} ik + \hat{e}_{35} \frac{\partial \hat{\bar{\phi}}}{\partial z} - 2i\hat{e}_{15} \hat{\phi}(D/2) \sin(kD/2) \right]_{z=H} .
\end{aligned} \tag{2.29f}$$

These six equations allow one to solve, in formal fashion using Cramer's Rule, for the coefficients C_m. It is useful to note that the left-hand coefficient matrix is the same as would be obtained in the solution of the "low coupling" homogeneous problem (no excitation terms) with the applied boundary conditions. If we represent the determinant of the left-hand side of the equations (2.29) by A, one can write

$$C_m = A_m/A,$$

where A_m is the determinant of the left-hand side of (2.29) with the m^{th} column replaced by the column vector of the right-hand side. The resulting expressions are very complicated and there is little purpose in writing them out in detail, it is sufficient to state that the complete transformed solutions in both layer and substrate are now known.

It should be remembered that, at this point, the $[C_m]$ are the coefficients of the transformed homogeneous solutions. In the following section the inverse transform of these terms will be considered and it will become apparent how they can be evaluated to obtain the homogeneous solution in "real-space". The actual computation procedure will be described in Chapter IV.

2.2.6 The Complete Solutions in "Real-Space"

2.2.6.1 Application of the Inverse Fourier Transform

Having obtained the complete transformed solutions in both layer and substrate, the solutions in terms of the spatial variables (x,z) are given by the application of the inverse Fourier transform, defined by (2.14). Thus, the solutions to equations (2.12) can be written:

$$U_1(x,z) = \frac{1}{2\pi}\int_{-\infty}^{\infty}\sum_{m=3}^{6} C_m a_{1m} e^{ikl_m z} e^{ikx} dk + \frac{1}{2\pi}\int_{-\infty}^{\infty}\overline{U}_1^P(k,z)e^{ikx}dk \qquad (2.30a)$$

$$U_3(x,z) = \frac{1}{2\pi}\int_{-\infty}^{\infty}\sum_{m=3}^{6} C_m a_{3m} e^{ikl_m z} e^{ikx} dk + \frac{1}{2\pi}\int_{-\infty}^{\infty}\overline{U}_3^P(k,z)e^{ikx}dk \qquad (2.30b)$$

$$W_1(x,z) = \frac{1}{2\pi}\int_{-\infty}^{\infty}\sum_{m=1}^{2} C_m a_{1m} e^{ikl_m z} e^{ikx} dk - \frac{1}{2\pi}\int_{-\infty}^{\infty}\overline{W}_1^P(k,z)e^{ikx}dk \qquad (2.30c)$$

$$W_3(x,z) = \frac{1}{2\pi}\int_{-\infty}^{\infty}\sum_{m=1}^{2} C_m a_{3m} e^{ikl_m z} e^{ikx} dk - \frac{1}{2\pi}\int_{-\infty}^{\infty}\overline{W}_3^P(k,z)e^{ikx}dk \ , \qquad (2.30d)$$

where the range of integration is along the real axis in k-space.[59] Though these integrals represent the complete theoretical solutions, the solution of any practical problem requires their evaluation.

Before continuing with the evaluation of the integrals (2.30), it is useful and enlightening to consider briefly some of the points concerning the "existence" of the solutions. In general, the existence of the solutions of (2.30) requires that the integrands satisfy Dirchlet's conditions for $-\infty < k < \infty$ and that the integrals be absolutely convergent*. The function f(k) is said to satisfy Dirchlet's conditions in the interval (a,b) if[59]:

(1) f(k) has only a finite number of maxima and minima in (a,b)

(2) f(k) has only a finite number of finite discontinuities and no infinite discontinuities in (a,b).

Keeping in mind the above requirements, let us now consider the solutions (2.30).

---

* See section 3.2, Theorem 7, of Ref. 59.

Consider first the particular integral portion of the equations (2.30), given by the general form

$$\frac{1}{2\pi}\int_{-\infty}^{\infty}\overline{V}_j^P\, e^{ikx}dk \,.$$

From (2.26) one has

$$\overline{V}_j^P = \sum_n \left\{ P_n(k)\left[a_{jn}e^{-M_n z} + b_{jn}e^{M_n z}\right] + \sin(k\, D/2)\left[c_{jn}e^{-M_n z} + d_{jn}e^{M_n z}\right]\right\}.$$

As can be seen from equations (2.23) and (2.24), the terms a_{jn}, b_{jn}, c_{jn} and d_{jn} are "piecewise" continuous and finite for all real k; and the terms c_{jn} and d_{jn} decay like $1/k$ as $|k| \to \infty$, not only for k real but for k complex as well. The situation where the left hand side of equations (2.23) and (2.24) vanishes at certain values of k, as mentioned earlier, allows the concept of "piecewise" continuity. The appropriate functions are redefined at these points and thus do not represent infinite discontinuities. There may, however, be an infinite number of these 'finite' discontinuities since the summation over the index 'n' represents the expansion of the applied potential function and may include an infinity of terms. Nevertheless, one should remember that these points can occur on the real axis only if $c_{12} = c_{33} = 0$ and because dissipation has been ignored in the preceeding derivations. In a true physical situation these points would not occur on the path of integration (the real axis) because of loss and thus one may consider them as being slightly removed from it.

As shown earlier, the terms b_{jn} and d_{jn} can only be non-zero in the layer region where z is finite. Hence, the expression for $\overline{V}_j^P$ remains finite, over the allowed range of z, for all |real k| > 0. Since the function $F_n(k)$ is continuous and converges to zero as $|k| \to \infty$ along the real axis, the term $\overline{V}_j^p$ is then continuous and converges to zero as $|k| \to \infty$ along the real axis, for all z. Examination of equations (2.23) and (2.24) also shows that k = 0 is not a pole, for the left hand side of these equations does not vanish; nor do the terms a_{jn}, b_{jn}, c_{jn} and d_{jn} vanish at k = 0. However, the term sin(kD/2) will vanish.

The homogeneous portion of equations (2.30) is represented by a summation of terms of the general form

$$\frac{1}{2\pi}\int_{-\infty}^{\infty} C_m \alpha_{jm} e^{ikl_m} e^{ikx} dk \quad .$$

The C_m are defined by the boundary condition equations, (2.29), while the α_{jm} are defined by the equations (2.16) and the l_m are the roots of the secular equation (2.17). The asymptotic behaviour of the l_m can be determined by examining equation (2.17). As $|k| \to \infty$ (k real), equation (2.17) reduces to

$$\begin{aligned}&[c_{55}c_{33} - c_{35}^2]l^4 + 2[c_{15}c_{33}c_{35}c_{13}]l^3 \\ &+ [c_{11}c_{33} + c_{55}^2 + 2c_{15}c_{35} - (c_{55} + c_{13})^2]l^2 + 2[c_{11}c_{35} - c_{15}c_{13}]l \\ &+ [c_{11}c_{55} - c_{15}^2] = 0 \; .\end{aligned}$$

The solutions of this equation are finite and in general will be complex. In the isotropic case, as shown in Appendix D.3, they have the values (±) i. As $|k| \to \infty$ along the real axis, the equation (2.16) can be written

$$\frac{\alpha_{3_m}}{\alpha_{1_m}} = \frac{-(c_{55}l_m^2 + 2c_{15}l_m + c_{11})}{[c_{35}l_m^2 + (c_{55} + c_{13})l_m + c_{15}]}$$

or

$$\frac{\alpha_{3_m}}{\alpha_{1_m}} = \frac{-\left[c_{35} l_m^2 + (c_{55} + c_{13}) l_m + c_{15}\right]}{(c_{33} l_m^2 + 2c_{35} l_m + c_{55})} \quad .$$

Since the l_m are finite for this situation, the α_{jm} will be bounded though not necessarily zero. Thus, the α_{jm} will be well behaved and continuous as $|k| \to \infty$ along the real axis.

In the substrate, where z can go to $-\infty$, only those values of l_m which give rise to decaying solutions are allowed; and it is this restriction which leads to the existence of "branch point contributions", as shown in Appendix D. Thus, when referring to the substrate solutions, the term $e^{ikl_m z}$ in the above integrand remains finite ($z = 0$) or converges to zero as $|k| \to \infty$. However, in the layer where z is finite, all four roots are allowed and there are two terms of the form $e^{ikl_m z}$ which can approach infinity as $|k| \to \infty$. Inspection shows that this situation will be countered by the appropriate C_m which contain the same terms in the form $e^{ikl_m H}$ in the denominator*. Thus, since the right-hand side of the equations (2.29) goes to zero as $|k| \to \infty$, the integrand

$$C_m \alpha_{jm} e^{ikl_m z} e^{ikx}$$

converges to zero as $|k| \to \infty$ along the real axis.

One should also consider the behaviour of the homogeneous solutions at $k = 0$. Multiplying the equation (2.17) by k^4, gives the following equation for $k_z = kl$:**

---

* H is the layer thickness, $z \leq H$, in the layer.

** Remembering that the 'k' being used is really k_x and kl represents k_z.

$$
\begin{aligned}
&(c_{55}c_{33} - c_{35}^2)k_z^4 + 2[k(c_{15}c_{33} - c_{35} - c_{13})]k_z^3 \\
&+ \left\{k^2[c_{11}c_{33} + c_{55}^2 + 2c_{15}c_{35} - (c_{55} + c_{13})^2] - (c_{33} + c_{55})\rho\omega^2\right\} k_z^2 \\
&+ [2k^3(c_{11}c_{35} - c_{15}c_{13}) - k(c_{35} + c_{15})\rho\omega^2]k_z \\
&+ [k^4(c_{11}c_{55} - c_{15}^2) - k^2(c_{11} + c_{55})\rho\omega^2 + (\rho\omega^2)^2] = 0 \ .
\end{aligned}
$$

In the limit, as $k \to 0$, the odd order coefficients vanish, and one has

$$(c_{55}c_{33} - c_{35}^2)k_z^4 - [(c_{33} + c_{55})\rho\omega^2]k_z^2 + (\rho\omega^2)^2 = 0 \ .$$

The solutions of this equation are finite and thus, as $k \to 0$, the values of $k_{zm} = (kl_m)$ remain finite. The α_{jm} are defined by equations (2.16) and can be written

$$\frac{\alpha_{3_m}}{\alpha_{1_m}} = \frac{-(c_{55}l_m^2 + 2c_{15}l_m + c_{11} - \rho\omega^2/k^2)}{[c_{35}l_m^2 + (c_{55} + c_{13})l_m + c_{15}]} \quad \text{or} \quad \frac{\alpha_{3_m}}{\alpha_{1_m}} = \frac{-[c_{35}l_m^2 + (c_{55} + c_{13})l_m + c_{15}]}{(c_{33}l_m^2 + 2c_{35}l_m + c_{55} - \rho\omega^2/k^2)} \ .$$

By multiplying both top and bottom of these expressions by k^2 they can be used for evaluating the α_{jm} at $k = 0$. In general, or at least when $c_{35} \neq 0$, there is no loss of generality in choosing $\alpha_{jm} = 1$. In this case, one can show that the α_{3_m} are all defined at $k = 0$ and that the left hand side of equations (2.29) does not vanish at $k = 0$, for there are no rows or columns which are repeated or identically zero. However, when $c_{35} = 0$, $k_z^2 = (\rho\omega^2/c_{33})$ or $(\rho\omega^2/c_{55})$ at $k = 0$, and the evaluation of the α_{jm} becomes more involved. In this situation, $\alpha_{1_m} = 1$ and $\alpha_{3_m} = 0$ for $k_z^2 = (\rho\omega^2/c_{55})$; and $\alpha_{1_m} = 0$, $\alpha_{3_m} = 1$ for $k_z^2 = (\rho\omega^2/c_{33})$. Hence, the left hand side of (2.29) still does not vanish at $k = 0$ and thus $k = 0$ is not a singularity (pole) for the homogeneous solutions.

There do exist, however, values of k(real) for which the left hand side of equations (2.29) does vanish and hence represent singularities (poles) in the C_m. It is these values of k which represent the propagating surface waves[23,36,46], and they will be discussed in detail in section 2.2.6.3. The locations of these discontinuities can be removed from the contour of integration (real axis) by assuming that they have a small positive imaginary part for Real(k) > 0 and a small negative imaginary part for Real(k) < 0. This is equivalent to indenting the contour of integration to pass above or below the poles, as is the usual procedure, and is consistant with the presence of loss in the system.

Thus, having examined the integrals (2.30) in some detail, one can be confident that they satisfy the necessary conditions for the application of the inverse transform, and hence the required solutions do exist.

2.2.6.2 Evaluation of the Particular Integral Solutions

The particular integral solutions represent the forced motion of the material, within the bounds of the transducer region, in response to the exciting electric field of the transducer. In this section we shall not solve for the particular integral solutions in both layer and substrate, rather a general solution will be obtained along the same lines as the transformed particular integral solution in section 2.2.4. The solutions thus obtained can then be applied to either layer or substrate. The problem is to evaluate the integral

$$\frac{1}{2\pi}\int_{-\infty}^{\infty} \overline{V}_j^P e^{ikx} dk \quad , \qquad (2.31$$

where $\overline{V}_j^P$ is a general transformed particular integral solution in either layer or substrate. It has been shown that $\overline{V}_j^P$ is given by equation (2.26),

$$\overline{V}_j^P = \sum_n \Big\{ a_{jn} F_n(k) \left[e^{-M_n z} + Y_{jn} e^{M_n z} \right] + c_{jn} \sin(kD/2) \left[e^{-M_n z} + X_{jn} e^{M_n z} \right] \Big\} \quad , \qquad (2.26)$$

providing the left-hand side coefficient determinant of equations (2.23) and (2.24) does not vanish. Hence, the inverse transform, (2.31), can be written

$$\frac{1}{2\pi} \sum_n \left\{ e^{-M_n z} \int_{-\infty}^{\infty} F_n(k) a_{jn} e^{ikx} dk + e^{M_n z} \int_{-\infty}^{\infty} F_n(k) b_{jn} e^{ikx} dk \right\}$$
$$+ \frac{1}{2\pi} \sum_n \left\{ e^{-M_n z} \int_{-\infty}^{\infty} \sin(kD/2) c_{jn} e^{ikx} dk + e^{M_n z} \int_{-\infty}^{\infty} \sin(kD/2) d_{jn} e^{ikx} dk \right\} \quad ; \qquad (2.32)$$

where

$b_{jn} = a_{jn} Y_{jn}$ and $d_{jn} = c_{jn} X_{jn}$, as before.

Thus, the problem reduces to that of finding the inverse transform of the functions

$F_n(k) a_{jn}$, $F_n(k) b_{jn}$, $\sin(kD/2) c_{jn}$ and $\sin(kD/2) d_{jn}$;

which represent an amplitude (the terms a_{jn}, b_{jn}, c_{jn} and d_{jn}) multiplied by functions which describe the behaviour of the electric potential function in k-space ($F_n(k)$ and $\sin(kD/2)$).

The discontinuities in the terms a_{jn}, b_{jn}, c_{jn}, d_{jn} represent so-called "removable singularities"[24]. The functions are still defined at these points, only the definition is different from that in other regions of k-space. Since the Fourier expansion converges to the average of the values on either side of a finite discontinuity[59], this form of singularity does not add any contribution to the integrals of (2.32). The integrals of (2.32) do not contain any branch points, and in the absence of other singularities, i.e. poles, the last two integrals of (2.32) will vanish, as shown in Appendix C.4. The first three integrals are evaluated as shown in Appendix C.3 and the particular integral contribution can be written

$$V_j^P(x,z) = P_o \sum_n \left\{ a_{jn}\left(\frac{n\pi}{L}\right)\left[e^{-M_n z} + Y_{jn}\left(\frac{n\pi}{L}\right) e^{M_n z}\right] e^{in\pi x/L} \right.$$

$$\left. + \, a_{jn}\left(-\frac{n\pi}{L}\right)\left[e^{-M_n z} + Y_{jn}\left(-\frac{n\pi}{L}\right) e^{M_n z}\right] e^{in\pi x/L} \right\} \; ; \quad (2.33)$$

where $\quad Y_{jn}(k) = b_{jn}(k)/a_{jn}(k)$, as before ,

and $\quad P_o = \begin{cases} \frac{1}{\pi}, & 0 \leq |x| < D/2 \\ 0, & |x| > D/2 \end{cases}$.

It is worthwhile noting that the solutions (2.33), for the range $0 \leq |x| < D/2$, are the same as would be obtained by solving equations (2.12) without the application of the Fourier transform and using

$$\cos(n\pi x/L) = \tfrac{1}{2}[e^{in\pi x/L} + e^{-in\pi x/L}] \; .$$

2.2.6.3 Evaluation of the Homogeneous Solutions

The homogeneous solutions are considerably more involved than the particular integral solutions, and there is little point in evaluating the complete solutions in both layer and substrate, since the approach is identical for the two regions. We shall consider a "general" homogeneous solution $V_j^H(x,z)$ which would apply to either region, and indicate those characteristics that apply only to a particular region. From equations (2.30), a typical homogeneous solution can be written

$$V_j^H(x,z) = \left(\tfrac{1}{2\pi}\right) \int_{-\infty}^{\infty} \sum_m C_m a_{jm} e^{ikl_m z} e^{ikx} dk \quad , \qquad (2.34)$$

where $C_m = A_m / A$. (For the substrate solutions, $W_j^H(x,z)$, $m = (1,2)$ while $m = (3,6)$ for the layer solutions, $U_j^H(x,z)$.) The term A_m is the determinant of the left-hand-side of equations (2.29) with the m^{th} column replaced by the column vector of the right-hand side, [RHS] , and A is the determinant of the left-hand side of (2.29).

Consider the right-hand side column vector of equations (2.29), [RHS]. There are six terms in [RHS], one for each of the equations (2.29a - 2.29f), and inspection of equations (2.24) shows that each term consists of linear operators (algebraic in 'k' and linear differential in 'z') operating on functions which are represented by summations of terms. Since the operators are linear they can be moved within the summation signs so that they act upon each individual term of the summations[37]. If one groups the resulting terms after performing this operation, it becomes apparent that they can be divided into two groups involving the familiar expressions $F_n(k)$ and sin (kD/2). Thus, after considerable algebraic manipulation, one can write the j^{th} term of [RHS] as

$$RHS_j = \sum_n \left[F_n(k)\beta_{jn1} + \sin(db/2)\beta_{jn2} \right] \; ;$$

where the terms β_{jn1} and β_{jn2} are functions involving the linear operators mentioned above, operating on the individual terms of the summations. The summation over 'n' is over the number of terms present in the original

Fourier expansion of the electric potential function, given by (2.10).

Invoking the familiar properties of determinants[44], one can then write

$$A_m = \sum_n \left[F_n(k) A_{mn1} + \sin(kD/2) A_{mn2} \right] ,$$

where

$$A_{mn1} = \begin{bmatrix} \beta_{1ni} \\ \beta_{2ni} \\ \beta_{3ni} \\ \beta_{4ni} \\ \beta_{5ni} \\ \beta_{6ni} \end{bmatrix} \longleftarrow \text{β_{jni} substituted into the m^{th} column of the left-hand side of (2.29)} .$$

Thus,

$$C_m = \sum_n \left[F_n(k) \frac{A_{mn1}}{A} + \sin(kD/2) \frac{A_{mn2}}{A} \right] ,$$

and (2.34) can be written

$$V_j^H(x,z) = \frac{1}{2\pi} \sum_n \sum_m \int_{-\infty}^{\infty} \left[F_n(k) \frac{A_{mn1}}{A} + \sin(kD/2) \frac{A_{mn2}}{A} \right] \alpha_{jm} e^{ikl_m z} e^{ikx} dk . \quad (2.35)$$

The function A has zeroes at $k = \pm k_s^*$, corresponding to those values of k which represent propagating surface waves[23,36,46]. These values of k occur on the real axis as a result of having neglected the effects of dissipation in the preceeding derivations. To correct for this fact, and to ensure outgoing waves which decay as $|x| \to \infty$, it must be assumed that k_s

---

* That the values are symmetric is, of course, required by physical symmetry.

has a small positive imaginary part for Real $(k_s) > 0$ and a small negative imaginary part for Real $(k_s) < 0$, as was observed in section 2.2.6.1. Since the roots l_m of equation (2.17) are multivalued functions of k, one expects to find values of $k = \pm k_b$* which are branch points of the integrand of (2.35) and represent the occurrence of bulk wave solutions[36]. The branch points are discussed in detail in Appendix D; however, due to the complexity of the integrands, no attempt will be made to obtain the exact branch point contributions to (2.35). As is also shown in Appendix D.1, it is only the substrate solutions $W_j^H(x,z)$ which have branch point contributions. There are no branch point contributions to the layer solutions.

Having observed that the function A has zeroes located at $k = \pm k_s$, it should be noted that the value of $|k_s|$ may not be unique. The propagation of numerous** surface wave "modes" in layered structures is possible when the substrate is a "faster" material than the layer[1,50]. We shall only consider the contributions arising from a particular mode, defined by $|k_s|$, and ignore the contributions from the other surface wave modes, if they exist†.

Before proceeding further, consider the behaviour of A in the vicinity of its zeroes. In the neighborhood of $k = k_s$, A can be defined by the Taylor's expansion,

---

* That the values are symmetric is, of course, required by physical symmetry.

** An infinite number of "modes" can, in fact, occur.

† This restriction allows the effect of each surface wave mode to be considered separately, and the complete solution will be a composite of all the modes present. It should also be observed that the 'multi-mode' situation can occur for the case of a 'smooth' bond between layer and substrate, as shown by Arenbach and Epstein[1].

$$A(k) = A'(k_s)(k-k_s) + A''(k_s)\frac{(k-k_s)^2}{2!} + A'''(k_s)\frac{(k-k_s)^3}{3!} + \dots ,$$

where $A'(k_s)$ implies $\left[\frac{dA}{dk}\right]_{k=k_s}$. The "order" of the zero of A at $k = k_s$ is determined by the first non-zero derivative of A evaluated at $k = k_s$. Hence, if $A'(k_s) \neq 0$, the zero is of first order. However, if $A'(k_s) = 0$ but $A''(k_s) \neq 0$, then the zero is of second order, etc. Replacing k by $-k$ in the left-hand side of (2.29) does not change the magnitude of A, though it does replace the terms $e^{ikl_m z}$ by their conjugates. Equation (2.17) shows that the l_m, and thus the α_{jm} are functions of k^2. Since the term 'ik' which appears in the last four rows represents a multiplying factor of k^4, these terms are not affected by a change of sign in k. Thus, one can expect the behaviour of A in the vicinity of $k = k_s$ and $k = -k_s$ to be similar, though the derivatives in the Taylor's expansion may be replaced by their conjugates. Nevertheless, the zeros of A at $k = k_s$ and $k = -k_s$ will be of the same order.

The terms A_{mn1}, A_{mn2} and α_{jm} are defined for all k and have no singularities (poles). Thus, the expressions

$$\frac{A_{mn1}}{A}\alpha_{jm}e^{ikl_m z} \quad \text{and} \quad \frac{A_{mn2}}{A}\alpha_{jn}e^{ikl_m z}$$

can be expanded about the singularities at $|k| = k_s$ as[40]

$$\frac{A_{mn1}}{A}\alpha_{jm}e^{ikl_m z} = \left\{ \sum_{r=1}^{N} \left[\frac{j_{A_{mn11}}^{(r)}(z)}{(k-k_s)^r} + \frac{j_{A_{mn12}}^{(r)}(z)}{(k+k_s)^r} \right] + j_{\eta_{1mn}}(k,z) \right\} \quad (2.36a)$$

and

$$\frac{A_{mn2}}{A}\alpha_{jm}e^{ikl_m z} = \left\{ \sum_{r=1}^{N} \left[\frac{j_{A_{mn21}}^{(r)}(z)}{(k-k_s)^r} + \frac{j_{A_{mn22}}^{(r)}(z)}{(k+k_s)^r} \right] + j_{\eta_{2mn}}(k,z) \right\}, \quad (2.36b)$$

where N is the order of the zero of A at $|k| = k_s$. (The equations (2.36) represent a 'partial fraction expansion'.) The terms ${}^{j}A_{mn}^{(r)}$ are evaluated in the usual fashion, as is shown by LePage[40]. The functions ${}^{j}\eta_{1mn}$ and ${}^{j}\eta_{2mn}$ contain the other singularities of (2.35) at different values of $|k_s|$ in the multi-mode case as well as the branch point information which was in (2.35). As observed earlier, it is only in the substrate that branch point contributions occur, and thus in the layer the functions ${}^{j}\eta_{1mn}$ and ${}^{j}\eta_{2mn}$ only contain information on other singularities which may exist.

Though not necessarily obvious, computation indicates that in most cases $N = 1$. In this situation one has:

$$ {}^{j}A_{mn11}^{(1)}(z) = {}^{j}A_{mn11}(z) = \lim_{k \to k_s} \left[(k-k_s) \frac{A_{mn1}}{A} \alpha_{jm} e^{ikl_m z} \right] \qquad (2.37a) $$

$$ {}^{j}A_{mn12}^{(1)}(z) = {}^{j}A_{mn12}(z) = \lim_{k \to -k_s} \left[(k+k_s) \frac{A_{mn1}}{A} \alpha_{jm} e^{ikl_m z} \right] \qquad (2.37b) $$

$$ {}^{j}A_{mn21}^{(1)}(z) = {}^{j}A_{mn21}(z) = \lim_{k \to k_s} \left[(k-k_s) \frac{A_{mn2}}{A} \alpha_{jm} e^{ikl_m z} \right] \qquad (2.37c) $$

$$ {}^{j}A_{mn22}^{(1)}(z) = {}^{j}A_{mn22}(z) = \lim_{k \to -k_s} \left[(k+k_s) \frac{A_{mn2}}{A} \alpha_{jm} e^{ikl_m z} \right] . \qquad (2.37d) $$

Assuming that the terms A_{mn1}, A_{mn2} and $\alpha_{jm} e^{ikl_m z}$ do not have zeroes located at $k = \pm k_s$, the above expressions evaluated by the use of L'Hospital's Rule give:

$$ {}^{j}A_{mn11}(z) = \left[A_{mn1} \alpha_{jm} e^{ikl_m z} / A' \right]_{k=k_s} \qquad (2.38a) $$

$$^{j}A_{mn12}(z) = \left[A_{mn1}\,a_{jm}\,e^{ikl_m z}/A'\right]_{k=-k_s} \tag{2.38b}$$

$$^{j}A_{mn21}(z) = \left[A_{mn2}\,a_{jm}\,e^{ikl_m z}/A'\right]_{k=k_s} \tag{2.38c}$$

$$^{j}A_{mn22}(z) = \left[A_{mn2}\,a_{jm}\,e^{ikl_m z}/A'\right]_{k=-k_s} \quad , \tag{2.38d}$$

where $A' = \frac{dA}{dk}$. Hence, for first order poles at $k = \pm k_s$, one can write (2.34) as

$$V_j^H(x,z) = \cancel{\frac{1}{2\pi}} \sum_n \sum_m \int_{-\infty}^{\infty} \left\{ F_n(k) \left[\frac{^{j}A_{mn11}}{(k-k_s)} + \frac{^{j}A_{mn12}}{(k+k_s)} + {}^{j}\eta_{1mn} \right] \right.$$

$$\left. + \sin(kD/2) \left[\frac{^{j}A_{mn21}}{(k-k_s)} + \frac{^{j}A_{mn22}}{(k+k_s)} + {}^{j}\eta_{2mn} \right] \right\} e^{ikx} dk \quad . \tag{2.39}$$

The function $F_n(k)$ has been defined in section 2.2.2 as

$$F_n(k) = \frac{\sin[(k-n\pi/L)D/2]}{(k-n\pi/L)} + \frac{\sin[(k+n\pi/L)D/2]}{(k+n\pi/L)} \quad .$$

The integrals of (2.39), with the substitution of the expression for $F_n(k)$, are evaluated in Appendix C.3-C.6 and there are two regions of interest:

(1) the region within the limits of the transducer, $|x| < D/2$
(2) the region external to the transducer, $|x| > D/2$.

Let us first consider the region $0 \leq |x| < D/2$.

Using the results of Appendix C, and grouping terms, one has [*]

---

[*] The branch point contributions have been neglected, as well as the possible occurance of other poles in the functions $^{j}\eta_{1mn}$ and $^{j}\eta_{2mn}$, to allow consideration of the poles at $|k| = k_s$ only.

$$
\begin{aligned}
V_j^H(x,z) = \left(\tfrac{1}{2}\right) \sum_n \sum_m \Bigg\{ & \left[\frac{{}^jA_{mn11}}{(k-k_s)} + \frac{{}^jA_{mn12}}{(k+k_s)} + {}^j\eta_{1mn}(k,z) \right]_{k = n\pi/L} e^{in\pi x/L} \\
& + \left[\frac{{}^jA_{mn11}}{(k-k_s)} + \frac{{}^jA_{mn12}}{(k+k_s)} + {}^j\eta_{1mn}(k,z) \right]_{k = -n\pi/L} e^{-in\pi x/L} \\
& + \left[{}^jA_{mn11} G_n(k) + {}^jA_{mn21} \cos(kD/2) \right]_{k = k_s} e^{ik_s x} \\
& + \left[{}^jA_{mn12} G_n(k) + {}^jA_{mn22} \cos(kD/2) \right]_{k = -k_s} e^{-ik_s x} \\
& + i \left[{}^jA_{mn11} F_n(k) + {}^jA_{mn21} \sin(kD/2) \right]_{k = k_s} e^{ik_s x} \\
& - i \left[{}^jA_{mn12} F_n(k) + {}^jA_{mn22} \sin(kD/2) \right]_{k = -k_s} e^{-ik_s x} \Bigg\} , \qquad (2.40)
\end{aligned}
$$

where

$$G_n(k) = \frac{\cos[(k-n\pi/L)D/2]}{(k-n\pi/L)} + \frac{\cos[(k+n\pi/L)D/2]}{(k+n\pi/L)} .$$

(It should be remembered that k_s has been assumed to have a small imaginary part, and thus $(k_s \pm n\pi/L) \neq 0$.) Using equations (2.36) and (2.38), equation (2.40) gives

$$
\begin{aligned}
V_j^H(x,z) = \sum_n \sum_m \Bigg\{ & \left[\left(\tfrac{1}{2}\right) \frac{A_{mn1}}{A} \alpha_{jm} e^{ikl_m z} \right]_{k = n\pi/L} e^{in\pi x/L} \\
& + \left[\left(\tfrac{1}{2}\right) \frac{A_{mn1}}{A} \alpha_{jm} e^{ikl_m z} \right]_{k = -n\pi/L} e^{-in\pi x/L} \Bigg\} \qquad (2.41) \\
+ \sum_m \Bigg\{ & D_m^+ \left[\alpha_{jm} e^{ikl_m z} \right]_{k = k_s} e^{ik_s x} + D_m^- \left[\alpha_{jm} e^{ikl_m z} \right]_{k = -k_s} e^{-ik_s x} \Bigg\} .
\end{aligned}
$$

The terms D_m^+ and D_m^- are defined by

$$D_m^{(\pm)} = \sum_n \left(\tfrac{1}{2}\right) \left\{ \left[\frac{A_{mn1}}{A'} G_n(k) + \frac{A_{mn2}}{A'} \cos(kD/2)\right] \right.$$

$$\left. (\pm) i \left[\frac{A_{mn1}}{A'} F_n(k) + \frac{A_{mn2}}{A'} \sin(kD/2)\right] \right\}_{k = (\pm)k_s} .$$

In the region $x > D/2$*

$$V_j^H(x,z) = i \sum_m \left[C_m'(k) \alpha_{jm} e^{ikl_m z} \right] e^{ik_s x}_{k = k_s} \tag{2.42a}$$

and in the region $x < -D/2$

$$V_j^H(x,z) = -i \sum_m \left[C_m'(k) \alpha_{jm} e^{ikl_m z} \right] e^{-ik_s x}_{k = -k_s} . \tag{2.42b}$$

(Again the contributions from branch points and other possible values of $|k_s|$ have been ignored.) The term $C_m'(k)$ is given by

$$C_m'(k) = \sum_n \left\{ \left[F_n(k) A_{mn1} + \sin(kD/2) A_{mn2} \right] / A'(k) \right\}$$

$$= A_m(k)/A'(k) \quad . \tag{2.42c}$$

It may appear that we have performed an excessive amount of work to obtain the results (2.42), which would be obtained by the immediate application of Cauchy's Theorem to equation (2.34); however, approaching the problem in the latter fashion does not give the homogeneous solutions within the transducer region.

---

*Ignoring the contributions from branch points and other possible values of $|k_s|$.

The results (2.41) and (2.42) are, of course, valid only for first order poles at a particular $|k| = k_s$. If the poles are of higher order, as indicated by the fact that $A'(k_s) = 0$, the process for the evaluation of (2.36) and the functions which follow is a well established, though involved, procedure. (See, for example, Refs. 37 and 40). As indicated in Chapter IV, when computing solutions, the occurrence of a higher order pole is handled in a somewhat different fashion.

2.2.7 Summary

This completes the algebraic solution of the inhomogeneous layer problem, as outlined in section 2.1.5, for a particular value of $|k_s|$. The complete wave solutions (2.30) are now known in both the transducer region and outside, with the exception of the branch point contributions (bulk wave solutions in the substrate). In the region $x > D/2$, the solutions for layer and substrate are, respectively,

$$U_j^H(x,z) = i \sum_{m=3}^{6} \left[C_m'(k) \alpha_{jm} e^{ikl_m z} \right]_{k=k_s} e^{ik_s x} \qquad (2.43a)$$

and

$$W_j^H(x,z) = i \sum_{m=1}^{2} \left[C_m'(k) \alpha_{jm} e^{ikl_m z} \right]_{k=k_s} e^{ik_s x} \quad , \qquad (2.43b)$$

from equation (2.42a). For $x < -D/2$, the solutions are

$$U_j^H(x,z) = -i \sum_{m=3}^{6} \left[C_m'(k) \alpha_{jm} e^{ikl_m z} \right]_{k=-k_s} e^{-ik_s x} \qquad (2.44a)$$

and

$$W_j^H(x,z) = -i \sum_{m=1}^{2} \left[C_m'(k) \alpha_{jm} e^{ikl_m z} \right]_{k=-k_s} e^{-ik_s x} \qquad (2.44b)$$

from (2.42b). Within the transducer region, $-D/2 < x < D/2$, the solutions consist of both homogeneous and particular integral solutions. Using equations (2.33) and (2.41), the general form of the wave solutions within this region can be divided into a "wave packet" propagating in the positive x-direction, $V_j^+(x,z)$, and one propagating in the negative x-direction, $V_j^-(x,z)$. These can be written

$$\begin{aligned} V_j^+(x,z) = \sum_n \Bigg\{ & \left(\tfrac{1}{2}\right) a_{jn}(k) \left[e^{-M_n z} + Y_{jn}(k) e^{M_n z} \right] \\ & + \sum_m \left(\tfrac{1}{2}\right) \frac{A_{mnl}}{A} \alpha_{jm} e^{ikl_m z} \Bigg\} e^{in\pi x/L} \Bigg|_{k = n\pi/L} \\ & + \sum_m D_m^+ \left[\alpha_{jm} e^{ikl_m z} \right] e^{ik_s x} \Big|_{k = k_s} \end{aligned} \qquad (2.45a)$$

and

$$\begin{aligned} V_j^-(x,z) = \sum_n \Bigg\{ & \left(\tfrac{1}{2}\right) a_{jn}(k) \left[e^{-M_n z} + Y_n(k) e^{M_n z} \right] \\ & + \sum_m \left(\tfrac{1}{2}\right) \frac{A_{mnl}}{A} \alpha_{jm} e^{ikl_m z} \Bigg\} e^{-in\pi x/L} \Bigg|_{k = -n\pi/L} \\ & + \sum_m D_m^- \left[\alpha_{jm} e^{ikl_m z} \right] e^{-ik_s x} \Big|_{k = -k_s} \quad . \end{aligned} \qquad (2.45b)$$

The equations (2.45) are applicable to either the layer or substrate with the proper range of the index 'm' and the correct choice of the coefficients a_{jn} and Y_{jn}, as well as the decay factor M_n.

By factoring the term $e^{ik_s x}$ from (2.45a) and $e^{-ik_s x}$ from (2.45b), one can define "amplitude factors", $AF_j^+(x,z)$ and $AF_j^-(x,z)$, for the "wave packets" propagating in the positive and negative directions, respectively, as

$$AP_j^+(x,z) = V_j^+(x,z)/e^{ik_s x} \tag{2.46a}$$

and

$$AP_j^-(x,z) = V_j^-(x,z)/e^{-ik_s x} \quad . \tag{2.46b}$$

More will be said about these "amplitude factors" in Chapters VI and VII, where their full significance will become apparent.

CHAPTER III

TRANSDUCER ADMITTANCE

3.1 Introduction

In Chapter II the "low coupling inhomogeneous layer problem" has been solved. Mathematical expressions for the amplitude of the generated surface waves both inside and outside the transducer region, as functions of applied voltage and frequency, have been presented in section 2.2.6. In this chapter a method by which the total transducer admittance can be determined will be presented. There is no separation between bulk and surface waves in the following analysis; however, it will be assumed that the results obtained will be applied only to the surface wave solutions of section 2.2.6. The bulk wave contributions to the transducer admittance will be discussed briefly in Appendix D which is devoted to the discussion of branch points and bulk waves.

3.2 Transducer Admittance Using Complex Poynting's Theorem

Assuming a time dependence exp(-iωt) and in the absence of magnetic fields within the material, the complex Poynting's Theorem for a piezoelectric material is[3]

$$\int_V \left[F_i^* \frac{\partial U_i}{\partial t}\right] dV = \int_V [E_i^* J_i] dV - \int_A \left[T_{ij}^* \frac{\partial U_j}{\partial t}\right] n_i dA$$

$$-i\omega \int_V \left[E_i^* D_i + T_{ij}^* S_{ij} - \rho \frac{\partial U_i^*}{\partial t} \frac{\partial U_i}{\partial t}\right] dV, \quad (3.1)$$

where: J_i are the components of the conduction current density within V

F_i are the components of internal body force density

T_{ij} are the usual components of stress, defined by equation (2.1)

U_i are the displacement components

S_{ij} are the usual components of strain

E_i and D_i are the components of electric field and displacement, respectively

ρ is the mass density

V is the volume of material under consideration

A is the surface of V

n is the outward normal vector for the incremental area dA

$*$ represents the complex conjugate.

Equation (3.1) represents the energy balance within the volume V. The term on the left hand side is the complex power delivered to V by internal mechanical sources. The right hand side contains the power lost in electrical heating of the volume V, the power lost by radiation and the rate of change in the net stored energy within V. The surface integral on the right hand side will be recognized as the familiar complex acoustic Poynting vector. Applying equations (2.1) and (2.2) to the last term on the right hand side of (3.1), one can write

$$\int_V \left[F_i^* \frac{\partial U_i}{\partial t}\right] dV = \int_V [E_i^* J_i] dV - \int_A \left[T_{ij}^* \frac{\partial U_i}{\partial t}\right] n_i dA \qquad (3.2)$$

$$-i\omega \int_V \left[c_{ijkl} S_{ij}^* S_{kl} + E_i^* \varepsilon_i E_i - \rho \frac{\partial U_i^*}{\partial t} \frac{\partial U_i}{\partial t}\right] dV .$$

Only one subscript is required for the dielectric constants ε_i since we have assumed that the dielectric tensor is diagonal, in section 2.1.4.

In the case of a piezoelectric material being excited by an external source, one can think of the material as being filled with internal mechanical sources (F_i), coupled to the source by the electric field of the transducer. The complex power provided by these "sources" must be equal to that supplied by the external generator connected to the transducer electrodes. Hence, the integral

$$\int_V \left[F_i^* \frac{\partial U_i}{\partial t} \right] dV$$

can be replaced by the term $V_\delta^* I_\delta$, where V_δ and I_δ are the applied voltage and current from the generator, respectively. Thus,

$$P_\delta = V_\delta^* I_\delta = \int_V [E_i^* J_i] dV - \int_A \left[T_{ij}^* \frac{\partial U_j}{\partial t} \right] n_i dA \tag{3.3}$$

$$-i\omega \int_V \left[c_{ijkl} S_{ij}^* S_{kl} + E_i^* \epsilon_i E_i - \rho \frac{\partial U_i^*}{\partial t} \frac{\partial U_i}{\partial t} \right] dV \, .$$

The complex electrical power into the transducer is written $V_\delta^* I_\delta$ to be consistent with the term $E_i^* J_i$. If the transducer admittance is Y, it can be defined by

$$Y = P_\delta^* / |V_\delta|^2 \quad . \tag{3.4}$$

The complex conjugate of P_δ appears in (3.4) because electrical admittance is normally defined for an exp(iωt) time dependence, and we have used exp(−iωt) [47].

In the situation where the material enclosed by volume V is an insulator, $J_i = 0$, and equation (3.3) is written

$$P_\delta = - \int_A \left[T_{ij}^* \frac{\partial U_j}{\partial t} \right] n_i dA - i\omega \int_V \left[c_{ijkl} S_{ij}^* S_{kl} + E_i^* \epsilon_i E_i - \rho \frac{\partial U_i^*}{\partial t} \frac{\partial U_i}{\partial t} \right] dV \, . \tag{3.5}$$

The calculation of the transducer admittance by the use of equations (3.4) and (3.5) is analogous to the "Poynting Vector Method" used in the determination of the impedance of electro-magnetic antennas[38].

The time average power delivered by the generator is given by

$$\frac{1}{2}\,\mathrm{Real}(P_g) = -\frac{1}{2}\,\mathrm{Real}\left[\int_A \left(T^*_{ij}\,\frac{\partial U_j}{\partial t}\right) n_i\,dA\right] \quad , \qquad (3.6)$$

which is a well known result. Inspection shows that the integrand of the volume integral in (3.5) is purely real, and hence the volume integral is not included in (3.6).

In general, the field E_i appearing in equation (3.5) will contain the driving term resulting from the applied voltage as well as a field component coupled to the particle displacements. However, in the low coupling approximation it is this latter field which has been ignored, and thus the electric field term appearing in (3.5) is only the driving field.

To determine the transducer admittance from equations (3.4) and (3.5), it is necessary to use a volume V that totally encloses the transducer region. The obvious volume for this purpose is shown in Fig. 3.1. The "ends" of the volume V are planes A_1 and A_2, parallel to the (y,z) plane and located outside the transducer region. The "top" of the volume is plane A_3, parallel to the layer-substrate interface and located at $z > H$, while the "bottom" is located at $z = -\infty$. The two "sides" are planes parallel to the (x,z) plane and located at the ends of the transducer fingers. In the strictest sense, the transducer fingers should be excluded from the volume V; however, since we assumed that the fingers have negligible thickness in section 2.1.1, their inclusion in the volume described by Fig. 3.1 has no effect on the results of (3.5).

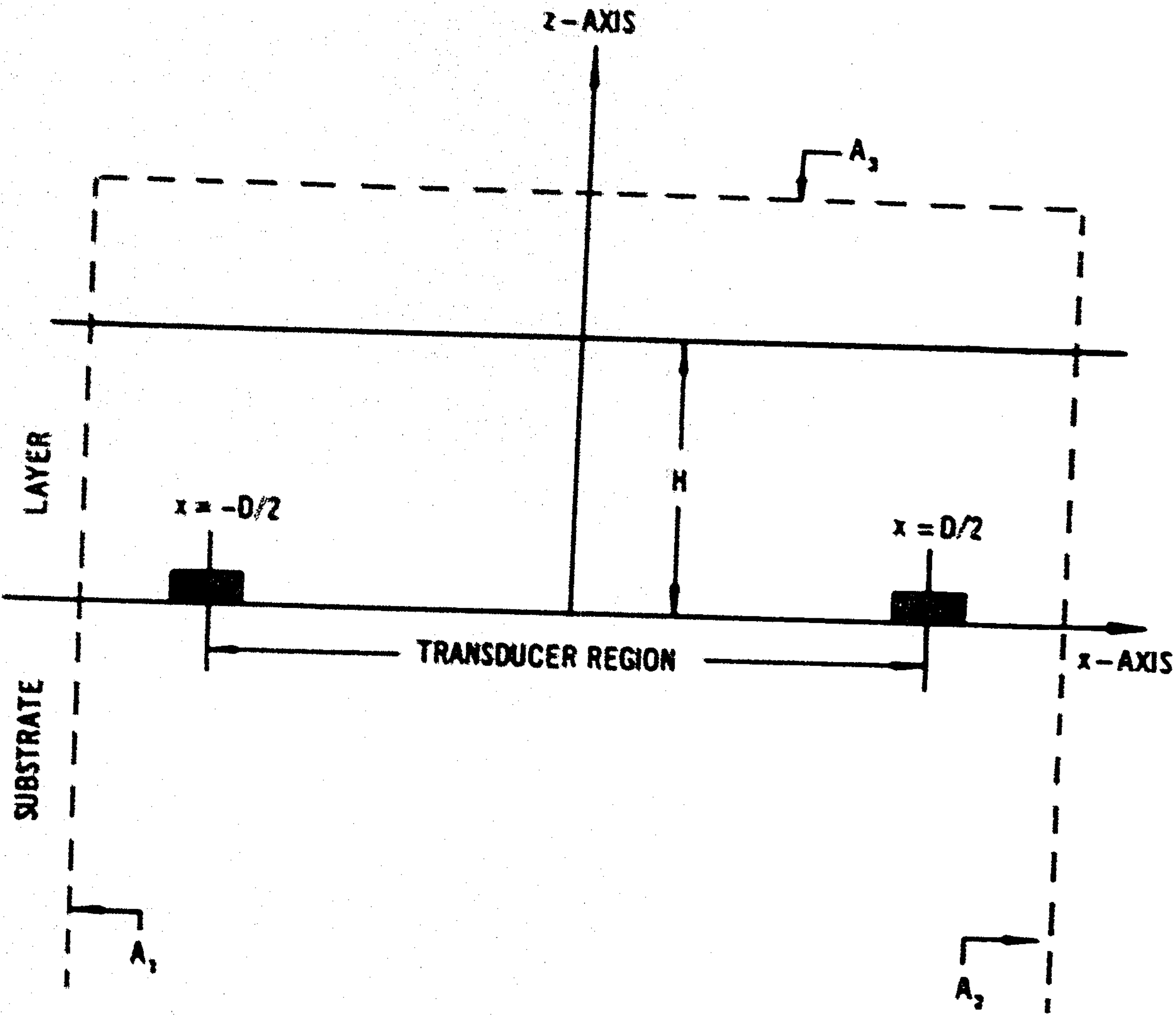

Figure 3.1 – Boundaries of region used for evaluation of Equation (3.5)

Because of the elastic and piezoelectric symmetry restrictions introduced in section 2.2.1, the components T_{21} and T_{23} are zero; and since the U_2 component has not been excited, there is no contribution to the surface integral of (3.5) from the "sides" of V. No acoustic waves are launched into the region above $z = H$; and since the particle displacements are zero at $z = -\infty$, the only contribution to the surface integral of (3.5) comes from the T_{1j} component over the surfaces A_1 and A_2. Since the surfaces A_1 and A_2 are located outside the transducer region, only the homogeneous wave solutions, given by equation (2.42), are used in the evaluation of the surface integral in (3.5)*.

In the regions $|x| > D/2$ the volume integral of (3.5) is zero. This is easily proved by considering the small volume V' formed by placing the plane A_4, parallel to A_2, at $x = D/2$, as shown in Fig. 3.2.

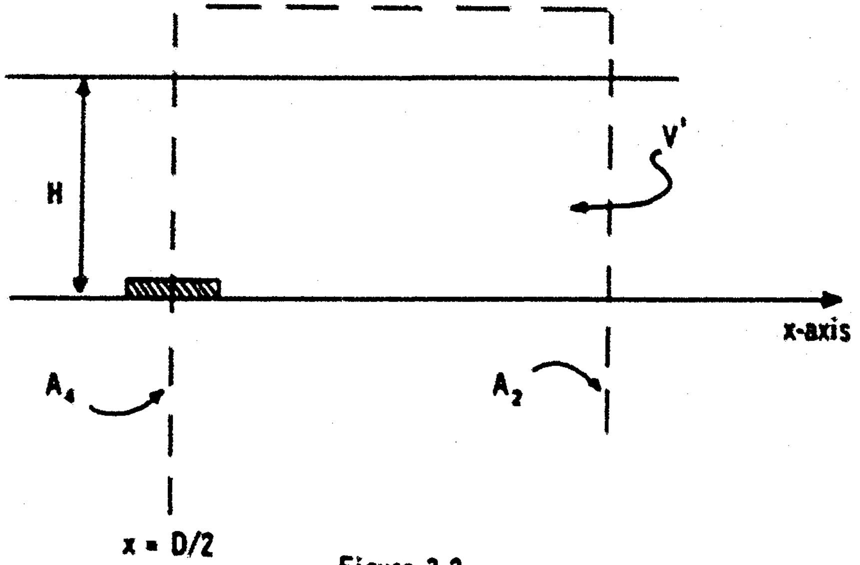

Figure 3.2

---

* Since T_{1j} is evaluated outside the transducer region, $T_{1j} = c_{1jkl}S_{kl}$ only, in the low coupling approximation.

Within this region there is no applied power from the generator and the left hand side of equation (3.5) for this region is zero. In the absence of loss, the surface integral of (3.5) for this region will also be zero and hence the volume integral must also vanish. Therefore, the only contribution to the volume integral of (3.5) comes from the volume bounded by $|x| = D/2$, the plane A_3 and the "sides" located at the ends of the transducer fingers. In evaluating the volume integral of (3.5) the solutions within the transducer region, given by (2.45) are used.

The means of performing the actual computations required to determine the transducer admittance Y is discussed in Chapter IV.

CHAPTER IV

COMPUTATIONAL METHODS

4.1 Introduction

In the preceeding chapters, a considerable amount of theoretical analysis has been presented. This analysis is not of much use unless it can lead to answers to specific problems. Due to the complexity of the analysis, one is forced to rely on a high-speed digital computer for the actual calculation of results. A Fortran-IV G-level program known as "LAYER" was prepared for performing the numerical analysis; however, due to the size of the program, it will not be described in detail. Rather, the important functions of the program will be considered, and the way in which answers are obtained will be discussed. A simplified flow chart showing the major steps is shown in Fig. 4.1.

4.2 Solution of the Electrostatic Problem

After checking the input parameters to be certain that the complete problem can be solved and performing a few routine computations to determine the bulk wave velocities in both layer and substrate, as well as the location of the substrate branch points, the "low coupling" electrostatic problem is solved. As described in section 2.1.4, the solution to this problem is performed by the program "CAPAX" prepared by Cermak et al.[12] The steps involved in the use of "CAPAX" are described in Appendix B. The call of "CAPAX" fills the grid which overlays an adjacent pair of fingers, as described in section 2.1.4, with the values of the "low coupling" electrostatic potential function for the chosen transducer configuration. The level z_1 on the grid, corresponding to the level at which the transducer is located, is chosen for the expansion of the potential function in

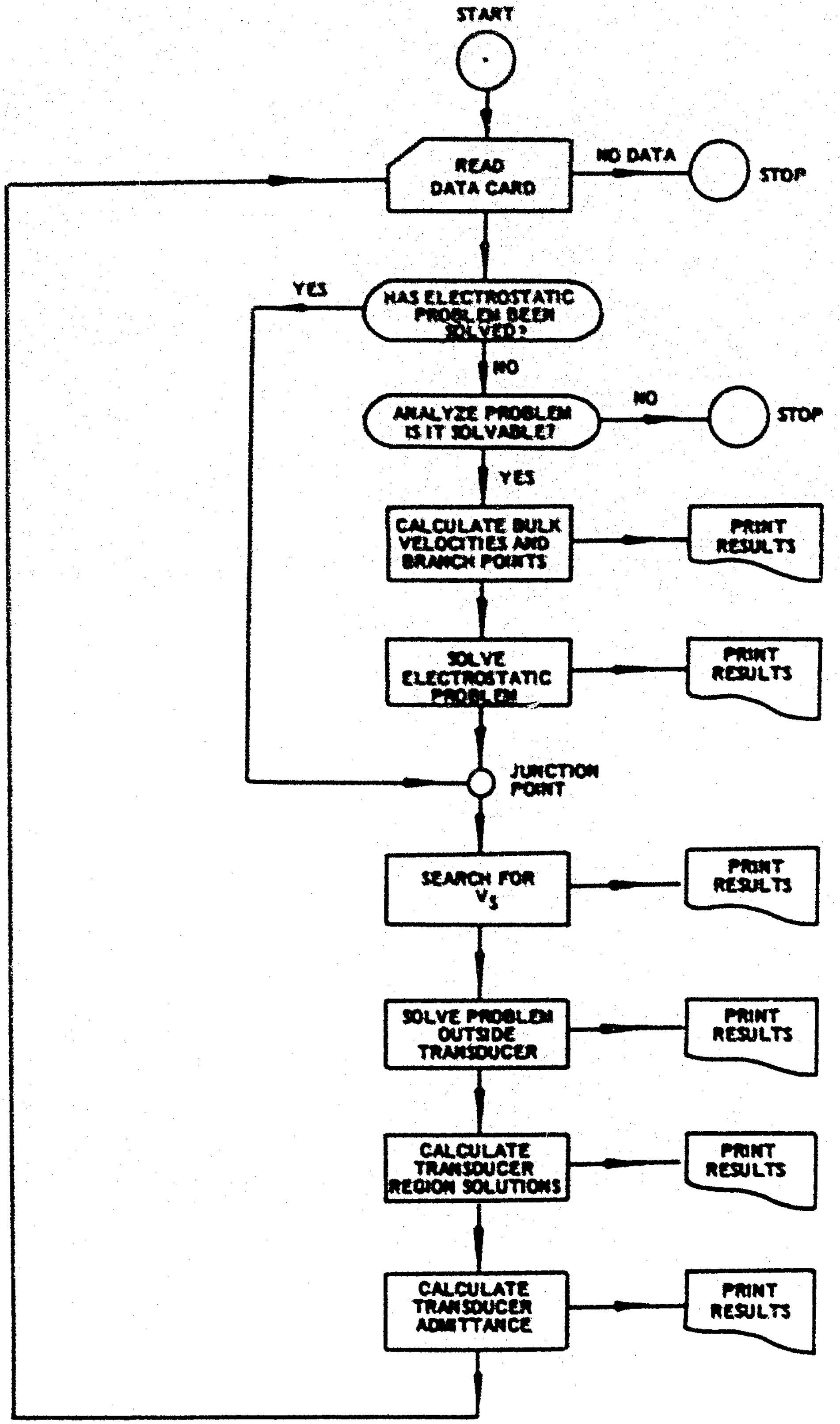

Figure 4.1 – Flow Chart of Computer Program

a Fourier series along the x-axis. Once the harmonic analysis is performed, the potential function within the transducer region, defined by equation (2.9b), can be written

$$\phi(x,z) = \sum_n A_n\left(e^{-M_n z} + r_n e^{M_n z}\right)\cos\left(n\pi\, x/L\right) , \qquad (4.1)$$

as shown in Appendix B.3, equation (B.10). The coefficients A_n are normalized for a potential of 1-volt (peak) between adjacent electrodes. "Adjacent" electrodes refers to adjacent fingers in the case of "bipolar" drive, and the fingers and plating in the case of "unipolar" drive.

After normalization of the A_n, the largest one is chosen and its harmonic number stored. As many as six more coefficients are then chosen, providing they are equal to or greater than a certain percentage (an input parameter, usually chosen to be 5%) of the largest. Thus, at most, the summation (4.1) will contain seven terms. Though this may appear to be an excessive simplification, in all cases analysed the magnitude of A_n is found to decrease very rapidly with increasing n. Nor does increasing the number of harmonics, by including additional smaller terms, significantly alter the final results*. The appropriate values of M_n and r_n are then computed and stored for later use, and the program proceeds to the next step.

4.3 Solution of the Homogeneous Problem Outside the Transducer Region

In the calculation of wave solutions, the homogeneous solutions outside of the transducer region represent a convenient starting point. Recalling from Chapter II, these particular solutions are defined for either layer or substrate by equations (2.42):

---

* This is discussed in Appendix F.

$$V_j(x,z) = i \sum_m \left[C'_m(k) a_{jm} e^{ikl_m z} \right]_{k=k_s} e^{ik_s x} \qquad (2.42a)$$

for waves propagating in the positive x direction, and by

$$V_j(x,z) = -i \sum_m \left[C'_m(k) a_{jm} e^{ikl_m z} \right]_{k=-k_s} e^{-ik_s x} \qquad (2.42b)$$

for waves propagating in the negative x direction. The term $C'_m(k)$ is defined by

$$C'_m(k) = A_m(k)/A'(k) \quad , \qquad (2.42c)$$

where A_m is the left-hand side coefficient determinant of the boundary condition equations, (2.29), with the m^{th} column replaced by the right-hand side column of the same equations. The term A' is the derivative of A, the left-hand side coefficient determinant of equations (2.29), taken at the value of $k = \pm k_s$ at which A vanishes. Hence, the first problem to be tackled is that of finding the value of $k = \pm k_s$ at which the determinant A will vanish. From a computational standpoint it is much easier to choose a frequency f_o and then find the value of phase velocity v_s at which A will vanish. Once the value of v_s is determined, one has $k_s = \pm 2\pi f_o/v_s$.

There is no easy method of locating the velocity v_s, and the method which has been adopted is to use a convergent numerical search technique known as a "Golden Section" search[76]. A judicious guess at the approximate value of v_s is made and an upper and lower bound for the search are specified. The range covered by these limits is then subdivided into finite intervals (original step size), and the value of $|A|$ is calculated at each one. This calculation involves computing the roots, l_m, for both layer and substrate, using the secular equation, (2.17), and the "eigenvector", $\begin{bmatrix} \alpha_{1m} \\ \alpha_{3m} \end{bmatrix}$, for each value of velocity. These values are then assembled according to equations (2.29), and the value of $|A|$ calculated. Since the values of α_{1m} and α_{3m} in the "eigenvector" are relative, α_{1m} is always chosen to be unity.

If the initial guess at the search range was a good one, the value of $|A|$ will have a minimum at some value of velocity $v = v_{min}$. The two values of velocity which bracket v_{min} are then chosen as new boundaries for the search, and the process is repeated in the appropriate fashion. In this manner, the program will rapidly converge toward the value of velocity for which $|A|$ is approximately zero. Of course, perfect convergence would require an almost unlimited amount of computing time, and thus "convergence" is defined as the point at which the variation from one value of velocity to the next is less than a preset fraction of the original step size. This fraction is usually chosen to be 10^{-3}. In spite of the many computations to be performed, convergence in this fashion is obtained within a matter of seconds using an IBM 360/75 system. If, perchance, the initial guess at the search range was a poor one and the minimum of A lies outside the chosen range, the program has a built in adjustment feature that will alter the original search range by as much as ± 1000 m/sec.

As pointed out in section 2.2.6.3, there may be several "modes" of propagation for a particular configuration, and hence different possible values of $|k_s|$. These will correspond to different values of v_s and, since only one "mode" can be considered at a time, the search range must be chosen so that the value of v_s for the desired "mode" will be found. If two or more "modes" exist within the chosen search range, the one which will be selected is uncertain.

Once the value of $v = v_s$ for the desired "mode" has been chosen, the values of the roots, l_m, and the "eigenvectors", $\begin{bmatrix} \alpha_{1m} \\ \alpha_{3m} \end{bmatrix}$, for the layer and substrate are recalculated at that velocity and stored for future use. So that the homogeneous solutions propagating in the negative x direction can also be determined, a separate set of roots, l_m^-, and "eigenvectors", $\begin{bmatrix} \alpha_{1m}^- \\ \alpha_{3m}^- \end{bmatrix}$, are calculated and stored for $v = -v_s$.

Continuing with the homogeneous solutions for $x > D/2$, the next step is to determine the derivative of A at $k = k_s$. The derivative, which is complex, is found numerically by evaluating A at $k = k_s$ and at points equally spaced on either side. As mentioned in section 2.2.6.3, in most cases the derivative of A at $k = k_s$ is not equal to zero. However, in certain cases, the derivative may vanish. Rather than evaluate a second order pole in this situation, it is far easier to change the frequency f_o slightly and repeat the process, beginning at the start of this section. Since all calculations are done at a fixed frequency, the changing of the frequency by a small amount, when second order poles occur, is found to eliminate the problem.

The final step in obtaining the solutions for $x > D/2$ involves calculating the right hand side of the boundary condition equations, (2.29), so that $A_m(k_s)$, as defined by (2.42c), can be evaluated. This requires the determination of $\bar{\phi}\,(k,z)$ and $\phi(D/2)$ in both the layer and substrate, as well as the transformed particular integral solutions. The values of $\bar{\phi}(k,z)$ and $\phi(D/2)$ are given in the definitions accompanying equations (2.15):

$$\bar{\phi}(k,z) = \sum_n A_n F_n(k) f_n(z)$$

where

$$F_n(k) = \frac{\sin[(k-n\pi/L)D/2]}{(k-n\pi/L)} + \frac{\sin[(k+n\pi/L)D/2]}{(k+n\pi/L)}$$

and

$$\phi(D/2) = \sum A_n N_n f_n(z)$$

$$N_n = \begin{cases} -1, & m_o+n \text{ odd} \\ +1, & m_o+n \text{ even} \end{cases} \quad , \quad D/2 = m_o L \; .$$

The functions $f_n(z) = \left[e^{-M_n z} + r_n e^{M_n z}\right]$, as shown in Appendix B.3. Since the values of A_n and the harmonic number n have already been calculated and stored, as described in the preceeding section, the functions $F_n(k_s)$ and N_n are readily evaluated. Thus, the functions $\bar{\phi}(k,z)$ and $\phi(D/2)$ evaluated at $k = k_s$ are determined. Next the transformed particular integral solutions are obtained by solving equations (2.23) and (2.24) for each harmonic n. The terms on the right hand side of equations (2.29) are then assembled from their component parts, all of which have now been determined. The terms on the left hand side of equations (2.29) are then assembled using the previously stored roots, l_m, and "eigenvectors", $\begin{bmatrix} \alpha'_{1m} \\ \alpha'_{3m} \end{bmatrix}$. One can then calculate the values of $A_m(k_s)$ by substituting the right hand side of (2.29) into each column of the left hand side and evaluating the determinant. The coefficients $C'_m(k_s)$ are then found by dividing $A_m(k_s)$ by A', which was previously determined. In this fashion the complete homogeneous solutions, for waves external to the transducer region and propagating in the positive x direction, are specified.

To determine the same solutions for the waves propagating in the negative x direction, one returns to the calculation of A' and repeats the entire process using $k = -k_s$, the roots, l_m^-, and the "eigenvectors", $\begin{bmatrix} \alpha_{1m}^- \\ \alpha_{3m}^- \end{bmatrix}$.

4.4 Solutions Within the Transducer Region

The solutions within the transducer region consist of several different parts. First to be considered is the particular integral solution, given in general form by equation (2.33):

$$V_j^P = P_o \sum_n \left\{ a_{jn}(n\pi/L) \left[e^{-M_n z} - Y_{jn}(n\pi/L) e^{M_n z} \right] e^{-in\pi x/L} \right.$$

$$\left. + \, a_{jn}(-n\pi/L) \left[e^{-M_n z} + Y_{jn}(-n\pi/L) e^{M_n z} \right] e^{-in\pi x/L} \right\} , \quad (2.33)$$

where

$$Y_{jn} = b_{jn}/a_{jn} \quad \text{and} \quad P_o = \begin{cases} \frac{1}{2} , & 0 < |x| < D/2 \\ 0 , & |x| > D/2 \end{cases} .$$

The terms a_{jn} and b_{jn} are determined by solving equations (2.23) with $k = \pm n\pi/L$. The same computer subroutine is used to perform this function as was used to determine the transformed particular integral solution in the previous section. A change of variable in the argument list allows the subroutine to perform these somewhat different, but related, functions.

After determining the particular integral solutions, the homogeneous solutions within the transducer region, of the general form given by (2.41),

$$V_j^H(x,z) = \sum_n \sum_m \left\{ \left[\left(\tfrac{1}{2}\right) \frac{A_{mn1}}{\Lambda} \alpha_{jm} e^{ikl_m z} \right]_{k = n\pi/L} e^{-in\pi x/L} \right.$$

$$\left. + \left[\left(\tfrac{1}{2}\right) \frac{A_{mn1}}{\Lambda} \alpha_{jm} e^{ikl_m z} \right]_{k = -n\pi/L} e^{-in\pi x/L} \right\}$$

$$+ \sum_m \left\{ D_m^+ \left[\alpha_{jm} e^{ikl_m z} \right]_{k = k_s} e^{ik_s x} + D_m^- \left[\alpha_{jm} e^{ikl_m z} \right]_{k = -k_s} e^{-ik_s x} \right\} , \quad (2.41)$$

are calculated. The coefficients of the terms $e^{\pm in\pi x/L}$ are calculated immediately after determining the particular integral solutions. First the roots, l_m, and the "eigenvectors", $\begin{bmatrix}\alpha_{1m}\\ \alpha_{3m}\end{bmatrix}$, are evaluated and stored for $k=n\pi/L$. The value of A for $k=n\pi/L$ involves calculating the determinant of the left-hand side of equations (2.29) using only those roots and "eigenvectors" associated with $k=n\pi/L$. To evaluate the term A_{mn1}, the right-hand side of equation (2.29) must be constructed using the n^{th} terms of $\bar{\phi}(k,z)$, $\phi(D/2)$ and the particular integral solution, only. This specially constructed column vector is then substituted in each column of the left-hand side of (2.29) which uses only the values of l_m and $\begin{bmatrix}\alpha_{1m}\\ \alpha_{3m}\end{bmatrix}$ calculated at $k=n\pi/L$, and the resulting determinants calculated. In this way A_{mn1}/A is calculated for every value of n (maximum of seven different values). The entire process is then repeated for $k=-n\pi/L$, beginning at the calculation of the roots and "eigenvectors".

For the terms which propagate with the surface wave $k=\pm k_s$, the coefficients D_m^+ and D_m^- are defined by (see equations (2.41))

$$D_m^{(\pm)} = \sum_n (\tfrac{1}{2}) \left\{ \left[\frac{A_{mn1}}{A'} G_n(k) + \frac{A_{mn2}}{A'} \cos(kD/2)\right] (\pm)\, i \left[\frac{A_{mn1}}{A'} F_n(k) + \frac{A_{mn2}}{A'} \sin(kD/2)\right]\right\}_{k=(\pm)k_s} .$$

One can recognize the terms C'_m, calculated in the previous section, as defined by (except for the factor '$(\frac{1}{2})$')

$$C'_m = \sum_n \left[\frac{A_{mn1}}{A'} F_n(k) + \frac{A_{mn2}}{A'} \sin(kD/2)\right]_{k=k_s}$$

for the wave $e^{ik_s x}$, and

$$C'_m = \sum_n \left[\frac{A_{mn1}}{A'} F_n(k) + \frac{A_{mn2}}{A'} \sin(kD/2)\right]_{k=-k_s}$$

for the wave $e^{-ik_s x}$, from equation (2.42c). The other terms, given by

$$\sum_n (\pm) \left[\frac{A_{mn1}}{A'} G_n(k) + \frac{A_{mn2}}{A'} \cos(kD/2)\right]_{k=(\pm)k_s}$$

where

$$G_n(k) = \frac{\cos[(k-n\pi/L)D/2]}{(k-n\pi/L)} + \frac{\cos[(k+n\pi/L)D/2]}{(k+n\pi/L)} \quad ,$$

differ from the terms C'_m only in the factors $G_n(k)$ and $\cos(kD/2)$. These additional terms are calculated in the same manner as the C'_m were in the previous section, except that the functions $G_n(k)$ and $\cos(kD/2)$ are substituted into the right-hand side of the equations (2.26) in place of the functions $F_n(k)$ and $\sin(kD/2)$. In actual fact, the calculation of these additional terms is performed simultaneously with the calculation of the C'_m.

We have thus far outlined how numerical values for the wave solutions, both inside and outside the transducer region, are obtained. In spite of the very large number of calculations required, the determination of these solutions, at a single frequency, requires about 10 seconds of CPU time using an IBM 360/75 system.

4.5 Calculation of Transducer Admittance

The calculation of the transducer admittance, at a particular frequency f_o, is the last step in a long chain of operations. Since it depends on the values of the wave solutions both inside and outside the transducer region, it must be calculated after the other values are determined.

It will be recalled that the transducer admittance Y is defined by equations (3.4) and (3.5):

$$Y = P_G^*/|V_G|^2 \tag{3.4}$$

and

$$P_G = -\int_A \left[T_{ij}^* \frac{\partial U_j}{\partial t}\right] n_i dA$$
$$-i\omega \int_V \left[c_{ijkl} S_{ij}^* S_{kl} + E_i^* \epsilon_i E_i - \rho \frac{\partial U_i^*}{\partial t} \frac{\partial U_i}{\partial t}\right] dV \; . \tag{3.5}$$

As mentioned in section 4.2, all of the wave solutions are calculated with a voltage of one-volt (peak) between adjacent electrodes. Thus, $|V_G|^2 = 1$, in (3.4). It was observed, in section 3.2, that the electric field E_i, appearing in (3.5), is only the driving field when using the low coupling approximation. Therefore, the term

$$-i\omega \int [E_i^* \epsilon_i E_i] \, dV$$

represents the admittance of the static capacitance of the transducer only. The program "CAPAX", which is used to calculate the electric potential function, also calculates the transducer capacitance so that the admittance of this capacitance can be deleted from (3.5). The expression to be used in calculating the transducer admittance will then be

$$Y' = P_G'^* \quad , \tag{4.2}$$

where

$$P_G' = -\int_A \left[T_{ij}^* \frac{\partial U_j}{\partial t}\right] n_i dA - i\omega \int_V \left[c_{ijkl} S_{ij}^* S_{kl} - \rho \frac{\partial U_i^*}{\partial t} \frac{\partial U_i}{\partial t}\right] dV \tag{4.3}$$

and the admittance of the static capacitance will be added at the end of the computation. From a comparison standpoint, it is also convenient to have the admittance of the static capacitance separated from the other contributions.

It was shown, in section 3.2, that the only contributions to the surface integral of (4.3) came from integrating over the "end" faces of the enclosed volume V, while only the volume of the transducer region contributes to the volume integral of (4.3). However, because of the symmetry of our system, the surface integral need only be evaluated over the plane located at $x > D/2$, while the volume integral need only consider the volume in the range $0 \leq x \leq D/2$. Thus, one can write

$$P'_6 = -2\left\{ \int_{-W_o/2}^{W_o/2} \int_{-\infty}^{H} \left[T^*_{ij} \frac{\partial U_i}{\partial t} \right] dzdy + i\omega \int_{-W_o/2}^{W_o/2} \int_{-\infty}^{H} \int_{0}^{D/2} \left[c_{ijkl} S^*_{ij} S_{kl} - \rho \frac{\partial U^*_i}{\partial t} \frac{\partial U_i}{\partial t} \right] dxdzdy \right\}, \tag{4.4}$$

where W_o equals the overlap of the transducer fingers. Since only "straight crested" waves have been considered in the analysis, the integration along the y-axis introduces the multiplying factor W_o only. Therefore,

$$P'_6 = -2W_o \left\{ \int_{-\infty}^{H} \left[T^*_{ij} \frac{\partial U_i}{\partial t} \right] dz + i\omega \int_{-\infty}^{H} \int_{0}^{D/2} \left[c_{ijkl} S^*_{ij} S_{kl} - \rho \frac{\partial U^*_i}{\partial t} \frac{\partial U_i}{\partial t} \right] dxdz \right\}. \tag{4.5}$$

The first of these integrals, involving $T^*_{ij} \frac{\partial U_i}{\partial t}$ must be broken into two parts, one for the substrate and one for the layer. Each is readily evaluated algebraically using the "external" homogeneous solutions given by equation (2.42) and evaluated as described in section 4.3. The evaluation of this term is a trivial programming exercise, once the algebra has been performed, and it will not be considered further.

The second integral is not such a simple problem. It is an integral over two variables and the complexity of the solutions within the transducer region further complicate the situation. Without becoming involved in lengthy algebraic derivations, it can be shown that it is possible to integrate this function directly from $x = 0$ to $x = D/2$, at any fixed value of z. This fact is useful since several terms always integrate to zero over this range. Thus, the latter integral of (4.5) can be evaluated by a combination of numerical and direct integration. The z-axis from $z = 0$ to $z = H$ is subdivided into a number of points and at each point, z_i, the value of the integral along the x-axis is determined. Then the resulting vector of values along the z-axis is integrated by Simpson's Rule. The same procedure is repeated in the substrate, but starting at $z = 0$ and going down into the material. This allows one to terminate the integration when the terms are sufficiently small that the remaining ones will not appreciably alter the value of the final result.

4.6 Summary

In this chapter we have presented, in reasonable depth, the computational methods involved in the attaining of numerical results to the "low coupling inhomogeneous layer problem". Any further description would involve one in explaining the particular steps in detail from a programming standpoint, and that is not the purpose of this chapter.

CHAPTER V

COMPARISON BETWEEN COMPUTED AND MEASURED ADMITTANCE DATA

5.1 Introduction

Having comleted a considerable amount of analysis in the preceeding sections, one requires some form of experiment to test the validity of the theoretical results. From a measurement standpoint, perhaps the easiest parameter to accurately determine is the admittance (impedance) of the ID transducer. A comparison between measured and calculated admittance for a given configuration, as a function of frequency, serves as a test for all parts of the theoretical analysis and the computer program.

This chapter describes the experimental procedure used to perform the measurements and the comparison between measurement and theory. Both non-layered and layered structures were measured, and in all cases the interdigital transducer was located at the layer-substrate interface (on the free surface in the absence of a layer) and the transducer was driven in the common "push-pull" (bipolar) fashion.

It will be assumed that the ID transducer is represented by the following "equivalent circuit."

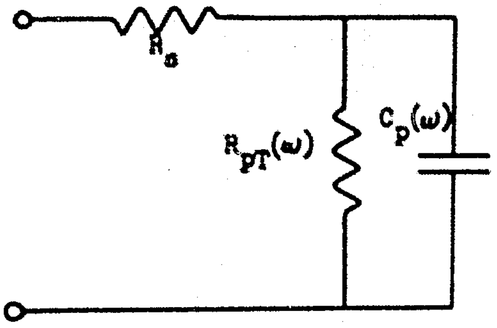

R_s = series electrical loss in the transducer and connections

R_{pT} = transducer radiation resistance

C_p = total transducer capacitance

Transposing the series resistance R_s, gives the circuit

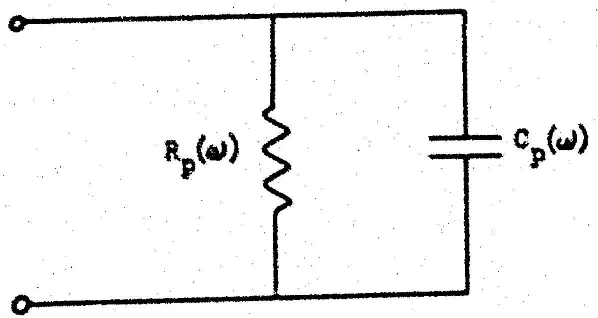

where

$$R_p(\omega) = \frac{R_s y + G}{y} + \frac{\omega^2 C_p^2}{y(R_s y + G} \quad ,$$

$$y = G^2 + \omega^2 C_p^2, \quad G = 1/R_{pT} \quad .$$

5.2 Experimental Procedure

The instrument used for performing the admittance measurements of the ID transducer was a Boonton RX-Meter, type 250-A. This unit provides a direct measurement of the parallel resistance (R_p) and capacitance (C_p) which represent the network being measured at the desired frequency. The frequency range of the RX-Meter extends from .5 MHz to 250 MHz. To enable accurate frequency measurements, a tap was placed on the output of the signal oscillator in the RX-Meter so that the test frequency could be continuously monitored with a Hewlett-Packard frequency counter, type 5245L. A 10 dB pad was used in the line between oscillator and counter to isolate the counter and prevent "pulling" of the oscillator frequency. For test frequencies greater than 50 MHz, the counter was used in conjunction with a type 5253-B frequency converter which extends the range to 500 MHz. Both the RX-Meter and the counter were the property of RCA

Limited, Montreal, and received calibration by their Instrument Services Division at regular intervals.

The tolerance of error in the measurement of R_p and C_p by the RX-Meter is given by the manufacturer as

$$\Delta R_p = \pm(2.0 + F/200 + R_p/5000 + Q/20)\% \pm 0.2\,\Omega \qquad (5.1)$$

and

$$\Delta C_p = \pm(0.5 + 0.5F^2 \times C_p \times 10^{-3})\% \pm 0.15\text{pf} \; ; \qquad (5.2)$$

where:

R_p and C_p are the measured values in ohms and pf

F is the frequency in MHz

$Q = 2\pi R_p C_p F \times 10^{-6}$.

In all cases, the $\pm 0.2\Omega$ appearing in (5.1) can be neglected. With the use of the external counter, the test frequency could be easily maintained to within ±10 kHz of the desired value. Since the test frequencies of interest are in the tens of MHz, this represents an imperceptible error in the test frequency. The limits of measurement accuracy will be shown for each case that follows, and are derived from the above equations.

To facilitate the connection of the surface wave devices to the RX-Meter, small printed circuit boards of the type shown in Fig. 5.1 were prepared. These boards were cut from 1/16" copper-clad phenolic laminate and the connecting pads were prepared by standard photo-etching procedures. After etching, the copper pads were nickel plated to ensure low resistance contact to the RX-Meter. The surface wave devices were mounted using black wax* and connection from the pads on the circuit board to the ID transducer was made with a doubled length of 0.010" gold wire which

---

* Black wax was also used at the edges of each sample to prevent undesirable reflections, and as an absorber between transducers when more than one transducer was present on the same surface.

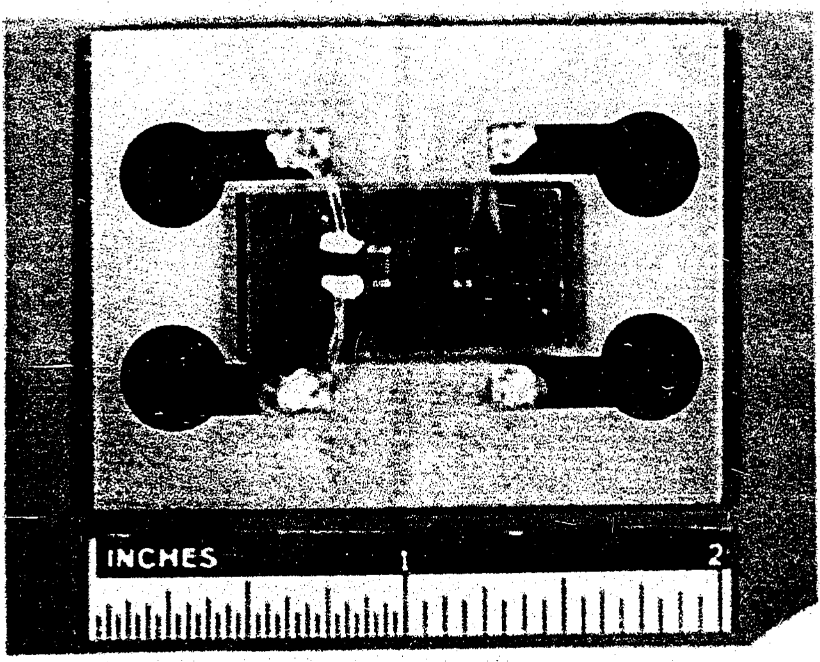

Figure 5.1 ZnO – SiO_2 structure mounted for use with RX-meter showing one transducer connected.

was soldered to the circuit board, and connected to the ID transducer with a pressed piece of freshly cleaved indium. The indium, when freshly cleaved, is very "sticky" and forms a very good, low resistance contact that can be removed without serious difficulty or damage to the device. Fig. 5.1 shows a mounted surface wave device with one of the transducers connected in the manner described. The circuit board with the mounted device was then connected to the thumb-screw terminals of the RX-Meter.

Measurements were carried out at appropriate frequency intervals for each device, with the circuit board being removed at each interval for proper balancing of the RX-Meter. The static capacitance of the circuit board was measured with the surface wave device mounted but electrically disconnected. The value of this additional capacitance was on the order of 0.5 pf, which was subsequently subtracted from the measured values of C_p to obtain the true value of C_p for the device. The only variation in this procedure was with a free surface $LiNbO_3$ device. Due to the high dielectric constant of this material, the static capacitance of the transducer was too large to be measured directly by the RX-Meter. To counter this difficulty, a small coil of approximately 0.7μH with a $Q > 100$ was prepared and soldered across the pads on the circuit board to parallel tune the transducer. After performing the measurements of R_p and C_p of the coil-ID transducer combination, the transducer was disconnected and the measurements were repeated for the coil and circuit board alone. With these two sets of measurements, it is a simple task to extract the true admittance characteristics of the ID transducer.

The series resistance, R_s, which represents the losses in the connections to the ID transducer and in the transducer itself, can be determined by measurement of R_p at several points either outside the "pass band" of the device or at the "nulls" in the response curve. In these instances, one can assume that the transducer is not launching surface waves ($R_{pr} = \infty$) and the value of R_s is given by

$$R_s = 1/(R_p \omega^2 C_p^2) \quad ,$$

providing

$$R_s^2 \omega^2 C_p^2 << 1 \quad .$$

5.3 Free Surface $LiNbO_3$

The excitation of acoustic surface waves on the free surface of $LiNbO_3$ has been well documented and analyzed[18,54,58]. For the analysis presented herein, it represents an interesting test case since $LiNbO_3$ is known to be a "high coupling" material, whereas we have considered only a "low coupling" theory.

A piece of XY cut Z propagating $LiNbO_3$ of dimensions 1." × 0.5" × 0.04" with one surface flat and polished was used for this measurement. The material was supplied by Crystal Technology Inc. and the z-axis was parallel to the long dimension to within ± 1°. A pair of ID transducers, aligned so as to launch surface waves along the z-axis, were fabricated on the polished surface. The transducers were fabricated by evaporating a 3000 Å layer of aluminum and then photo-etching. The transducer dimensions were:

$L = 50.8\ \mu m$ ($\lambda_r = 101.6\ \mu m$, λ_r = fundamental "resonant" wavelength)
$d = 25.4\ \mu m$
$W_o = 4.5\ mm$ (W_o is the finger overlap, or "aperture"),

and consisted of 15 finger pairs.

The measured behavior of the R_p and C_p is shown in Fig. 5.2a and Fig. 5.2b, respectively, for both transducers, and is compared with theoreti-

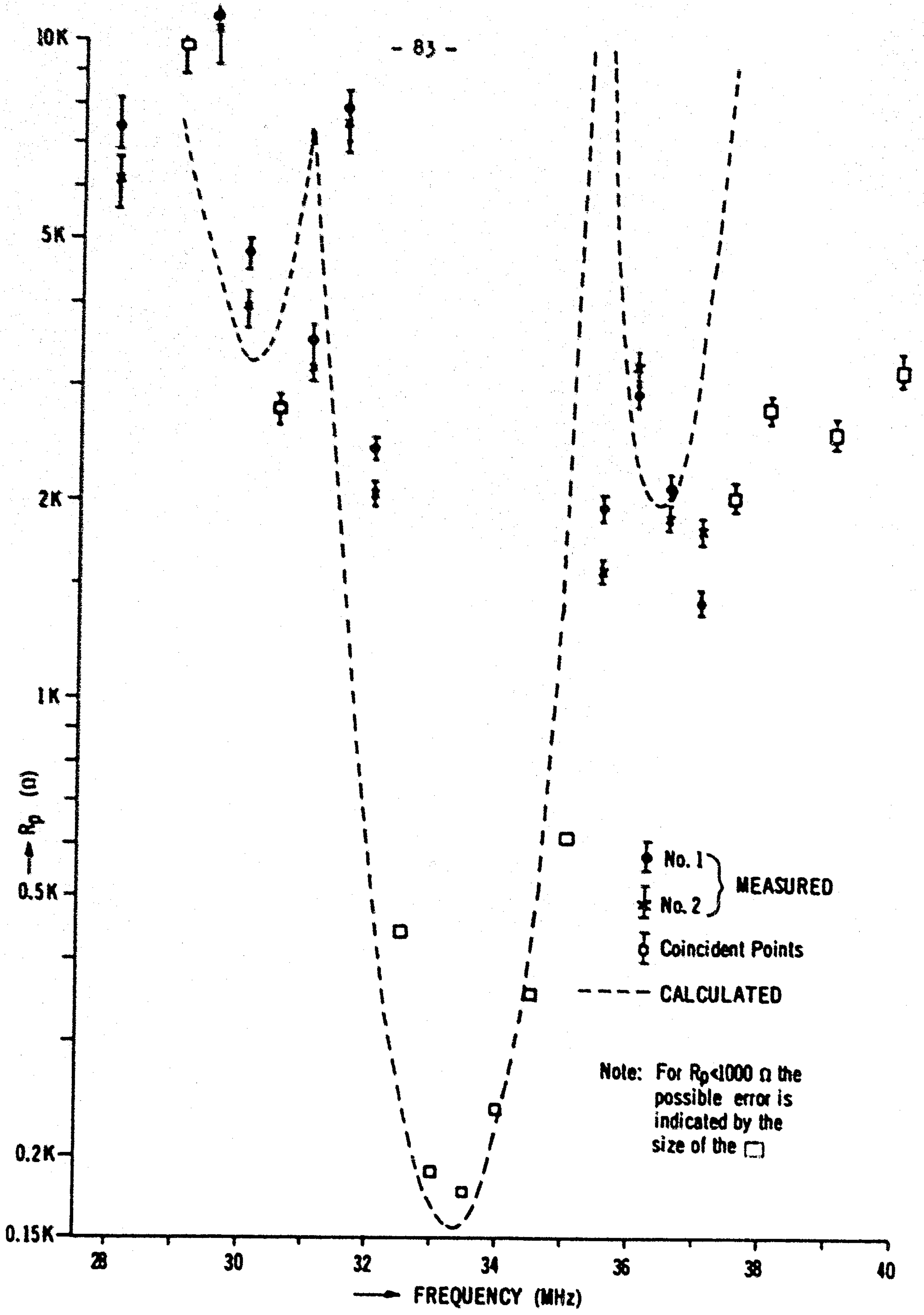

Note: For R_p<1000 Ω the possible error is indicated by the size of the □

Figure 5.2(a) – R_p for free surface $LiNbO_3$

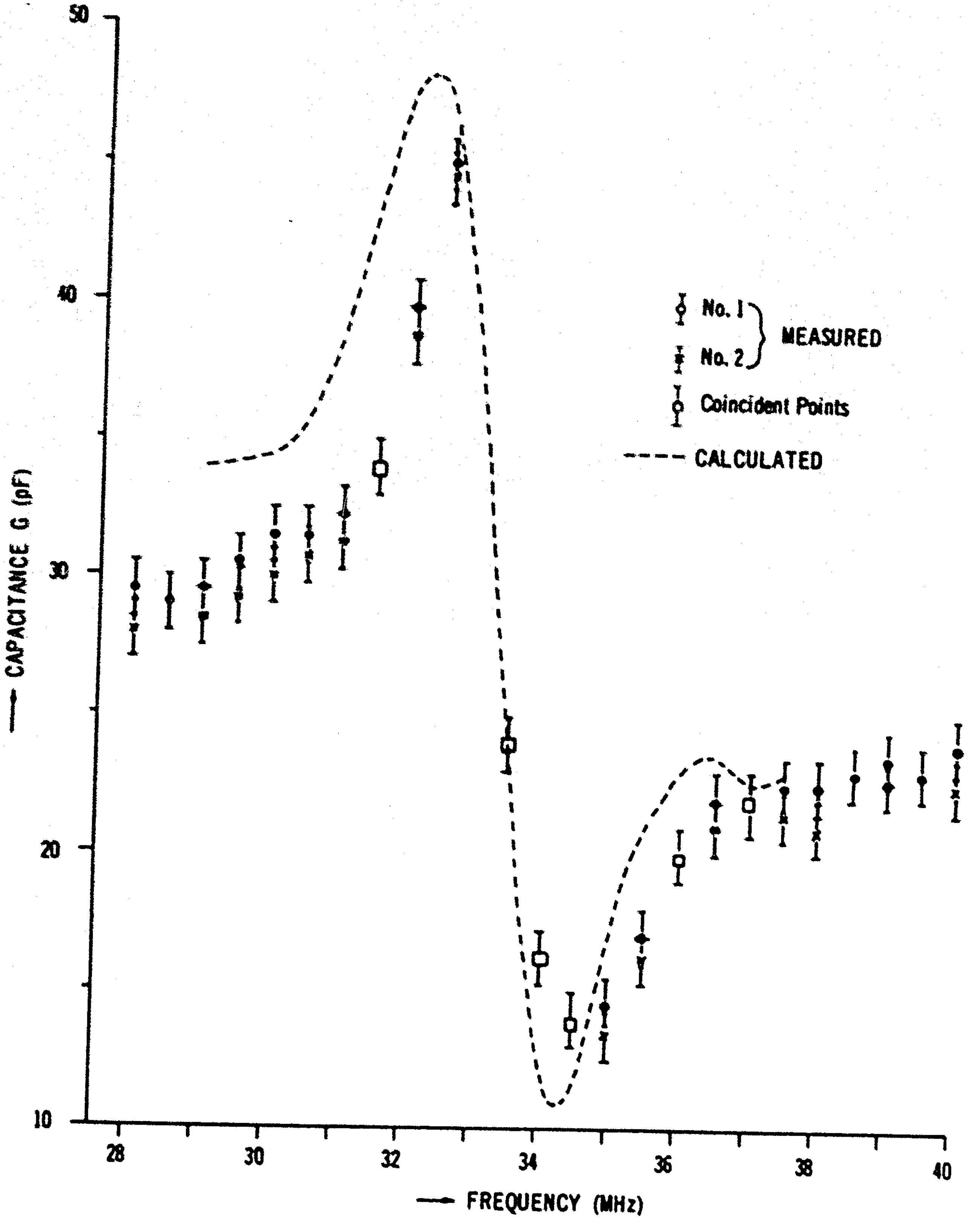

Figure 5.2(b) – C_p for free surface $LiNbO_3$

cal calculations. Measurements of R_p at frequencies below the "pass band" indicated that both devices, in their mounting, had an R_s of approximately 3 Ω, and this value was used in the calculation of the theoretical curve. The values of elastic and piezoelectric constants appropriate to this orientation of $LiNbO_3$ are:*

$$\begin{array}{ll} c_{11} = 2.45\times10^{11}\ N/m^2 & e_{11} = 1.3\ C/m^2 \\ c_{33} = 2.03 & e_{13} = 0.2 \\ c_{55} = 0.6 & e_{33} = 2.5 \\ c_{13} = 0.75 & e_{35} = 3.7 \\ c_{35} = -0.09 & \end{array} \qquad (5.3)$$

$$\rho = 4700\ kg/m^3, \quad \epsilon_1 = 29, \quad \epsilon_3 = 44 \ ,$$

and represent the values used in the calculation of the theoretical curve.

By observing the relative positions of the "nulls" on the two curves, it can be seen that the theoretical curve is shifted by about .5 MHz with respect to the measured values. This shift results from the fact that the theoretical curve is for a "low coupling" material and hence the presence of piezoelectricity does not alter the surface wave velocity. As is well known, the true surface wave velocity for $LiNbO_3$ is somewhat higher than that predicted by a low coupling theory. Hence, the measured points appear to lie on a curve that is shifted to a slightly higher frequency than that of the predicted curve. Nevertheless, the comparisons between the values of R_p at the "resonant" point as well as the peak to peak variation in C_p agree reasonably well. As discussed in Appendix D, the branch points for $LiNbO_3$ may occur at the values of the transverse and longitudinal bulk wave velocities, or slightly less since the material is not isotropic in the XZ plane. This implies that bulk wave generation by this

---

* The values given by (5.3) are obtained by applying the proper tensor rotation to the unrotated single crystal values given by Warner et al.[70].

ID transducer-material combination can begin at about 35 MHz, and may be the reason for the apparent asymmetry of the measured points for frequencies greater than 35 MHz. Behaviour of this nature has been observed by de Klerk and Daniel[18]. Skeie[54] has also observed asymetrical behaviour on $LiNbO_3$ and explains it on the basis of internal reflections and mass loading of the transducer fingers. Since none of these additional effects (bulk waves, internal reflections or mass loading by the fingers) have been considered in the analysis presented here, they are not included in the calculated curve.

As a test case, however, the comparison between the measured points and the theoretical curve indicates reasonable agreement in spite of the "low coupling" approximation used in the theory.

5.4 Free Surface ZnO

Another material, suitable for free surface acoustic wave propagation, and more in keeping with the approximations which have been made in the theory, is ZnO. Three slices of high resistivity single crystal ZnO, 1cm × 1cm × 1mm, with the c-axis normal to the surface were obtained from Airtron Corp. The three pieces were acquired without polishing and hence it was necessary to prepare the surfaces for the fabrication of ID transducers. Both surfaces of each slice were mechanically lapped and polished, the final polishing being done with 0.3 micron (Linde "A") powder. A single ID transducer was fabricated on one surface of each slice and measured with the RX-Meter in the manner previously described; however, since ZnO is a photoconductor, the measurements had to be performed in the dark. After performing a complete set of measurements on each device, the transducers were removed, and a new set fabricated on the reverse side of the slices.

The measurements were then repeated. In this fashion, a set of six ID transducers were measured, using both surfaces of the ZnO slices. The transducer dimensions were:

$$L = 101.6\ \mu m,\ (\lambda_r = 203.2\ \mu m)$$
$$d = 50.8\ \mu m$$
$$W_o = 3.5\ mm\ ,$$

and consisted of 15 finger pairs. The transducers were produced by the evaporation of 1500 Å of aluminum followed by photoetching.

From the measurements it soon became obvious that though ZnO may be a suitable material for our theory, it is far from being suitable in practice. This situation is evident in Figs. 5.3a and 5.3b, in which only three of the six sets of measurements have been presented to avoid excessive confusion. The reasons for the wide variation in performance from one device to another, particularly in the side lobe response seen in Fig. 5.3a, are unknown. (It should be noted that the theoretical side lobe response is much less than was actually observed, i.e., the theoretical R_p was much greater than the measured R_p in the side lobes.) The spread in the measurements appeared to be independent of the side of the slice used for the measurement; but rather, may be caused by "work damaged" surfaces as the result of the mechanical lapping and polishing of the material. Damage of this nature could create mobile carriers at the surface of the devices, resulting in changes in the piezoelectric activity and the addition of conduction loss. Another possibility is that the samples were not kept in the dark for a sufficiently long period of time before the measurements commenced, and the spread in the results is caused by latent photocarriers.

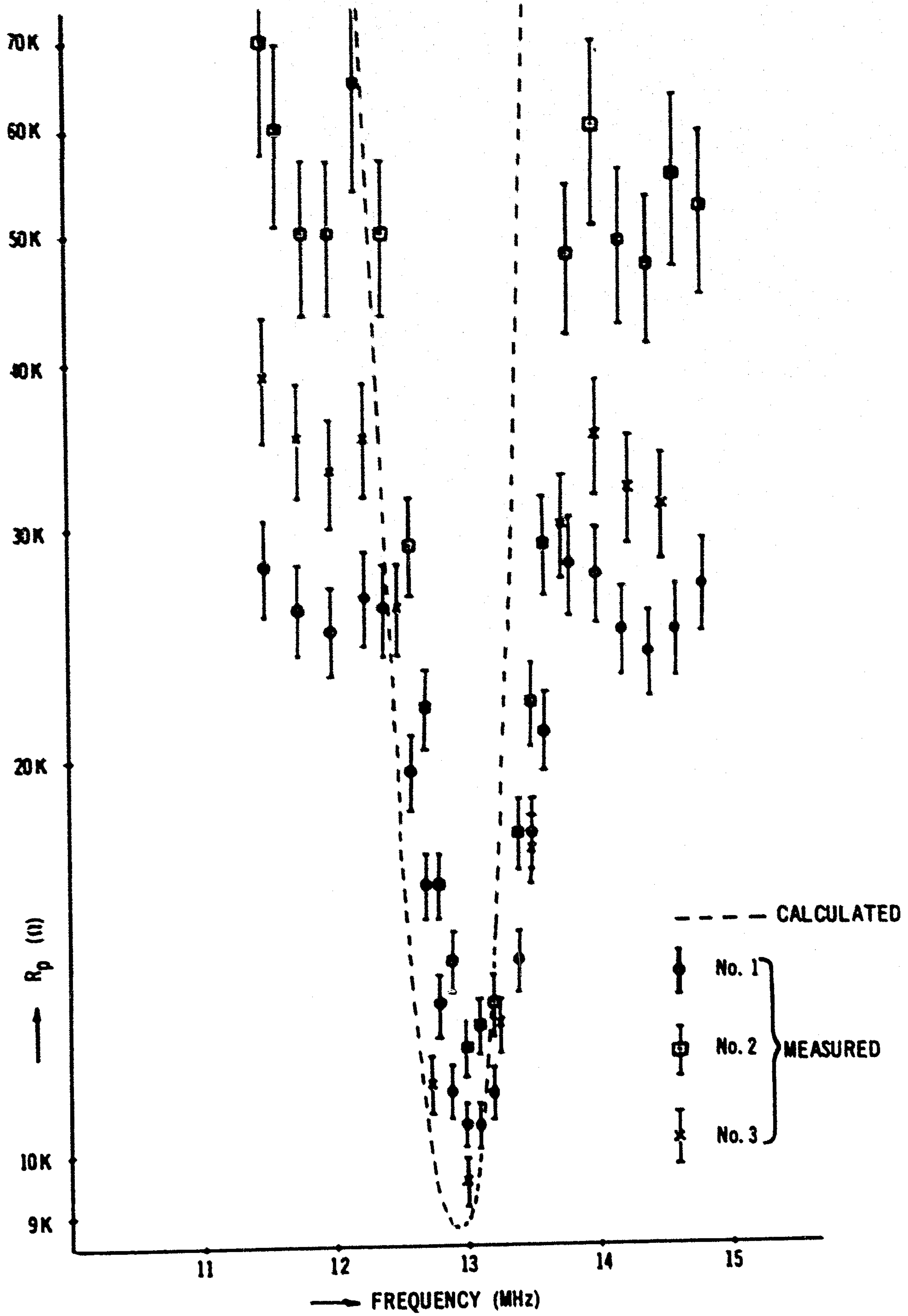

Figure 5.3(a) – R_p for free surface ZnO

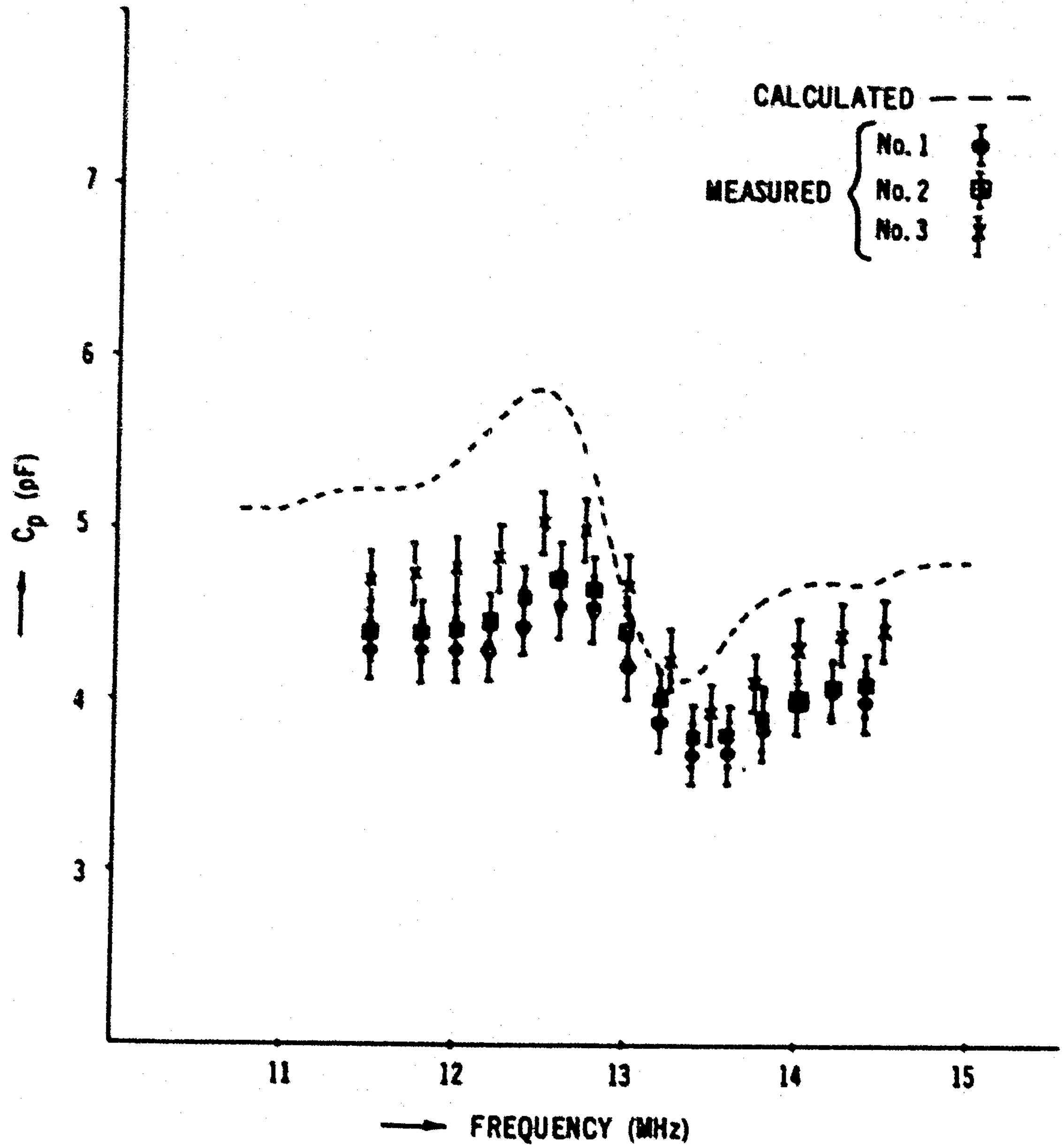

Figure 5.3(b) – C_p for free surface ZnO

Whatever the reason for the spread in results, it made the task of determining the R_s of the transducer very difficult, and an alternative approach was used. An ID transducer was fabricated on a clean glass slide, using the same thickness of aluminum as before, the only difference being that the fingers were continuous from one side to the other; hence, the transducer consisted of a number of thin electrical conductors, all in parallel. This "dummy" transducer was connected in the same fashion as the others and the DC resistance of the device and connections was found to be approximately 10 Ω. This value of R_s was used in the theoretical calculations which appear in Figs. 5.3a and 5.3b.

There has been some degree of conflict in the literature regarding the piezoelectric and elastic constants of ZnO[16,57]; and more will be said about this point in the following chapter, section 6.3. The constants which were used to provide the theoretical curves of Figs. 5.3a and 5.3b are[5,34]:

$$\begin{array}{llll} c_{11} = 2.097 \times 10^{11}\,\mathrm{N/m^2} & & e_{15} = -0.59\ \mathrm{C/m^2} & \\ c_{33} = 2.109 & & e_{31} = -0.61 & \qquad (5.4) \\ c_{44} = 0.425 & & e_{33} = \ \ 1.14 & \\ c_{13} = 1.051 & & \rho = 5676\ \mathrm{kg/m^3} & \end{array}$$

$$\epsilon_1 = 8.33, \quad \epsilon_3 = 8.84 \quad .$$

One can observe that there is reasonable agreement between the measured and calculated values of R_p at resonance and in the peak to peak variation in C_p. The calculated and measured resonant frequency are in good agreement, although there may be some evidence of "stiffening" of the ZnO by the piezoelectric effect.

Unfortunately there are problems which are not fully understood, but which are affecting, to a very large extent, the measurements of the ID transducer characteristics. Hence, the agreement between theory and experiment for this particular case is not as good as one would expect; in fact, it appears worse than the comparison for $LiNbO_3$ presented in the previous section. It would thus appear that single crystal ZnO, though a suitable material for free surface propagation from the standpoint of our "low coupling" theory, is not very satisfactory for experimental purposes.

5.5 Thin Films of ZnO on SiO_2

Since the goal of this analysis has been the study of acoustic surface wave generation in layered structures, it is desirable to have some experimental results which can be compared with theoretical calculations on layered structures. Through the courtesy of M. Holland (Raytheon Research Division, Waltham, Mass.), several samples of thin sputtered layers of ZnO on fused quartz were obtained*. The samples were identical, except for the thickness of the ZnO layer, and consisted of two ID transducers on a fused quartz substrate 1."× 0.5"× 0.040", with the ZnO sputtered over the surfaces. (Figure 5.1 showed one of these samples mounted for measurement.) The samples were designated as follows:

Sample Number	Layer Thickness
ZMU-50C	10.4 μm
ZMU-63/58	13.5 μm
ZMU-68/50B	31.3 μm

(Those samples with a / in the number indicate that the sample had its ZnO

---

* These samples were among those used by M. Holland in the paper presented at the IEEE Ultrasonics Symposium, December 1971, ref. no. 32.

layer produced by two separate depositions, with exposure to air between.) The ID transducers were of the following dimensions:

$$L = 19.5\ \mu m\ (\lambda_r = 39\ \mu m)$$

$$d = 9.75\ \mu m$$

$$W_o = 1.5\ mm \quad ,$$

and consisted of 20 finger pairs.

5.5.1 Sample ZMO-50C

The first of the samples to be received and analyzed was ZMO-50C. Of the two transducers on this sample, one of them contained a defect which caused the transducer to appear shunted by a DC resistance of several kilohms. Though this would not seriously affect the operation of the transducer as a generator or detector of acoustic surface waves, it complicates the admittance measurements. As a result, this transducer was not measured and the experimental points in Fig. 5.4 are from one transducer only.

Preliminary calculations, using the single crystal elastic and piezoelectric constants for ZnO given by (5.4), indicated that the sample was not performing as it should. However, it is a well known fact that the bulk wave coupling constants (K^2) for thin evaporated or sputtered films of ZnO are 12 - 80% lower than the corresponding single crystal values, indicating reduced values of the piezoelectric constants[17,22,25,29]. In order to clarify the situation with respect to this sample, it was decided to measure the piezoelectric element e_{33}. Since the c-axis of the film was normal to the substrate, to within a few degrees , this measurement required that the ZnO film be operated in the bulk "thickness" mode. This was achieved by the evaporation of four aluminum dots, 0.015" in diameter,

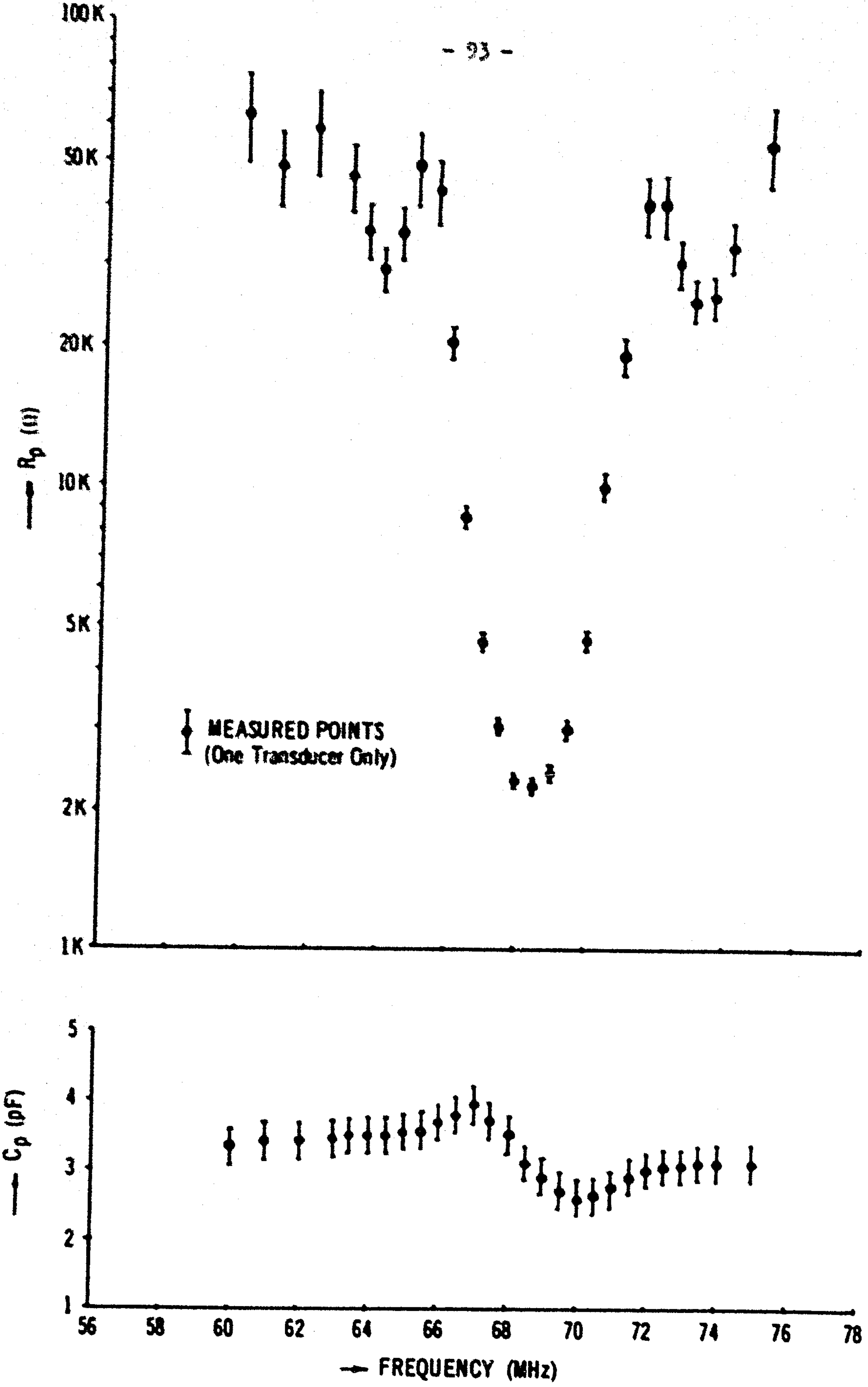

Figure 5.4 ZnO – SiO_2 sample ZMU – 50C

on the surface of the ZnO, each dot being located over one of the "side bars" of the ID transducer. By connecting a source between one of the "side bars" and the dot above, it was possible to launch longitudinal bulk waves into the substrate. Severe problems were initially encountered with reflections from the back surface of the substrate; however, these were almost totally eliminated by sand-blasting the back surface until it was sufficiently roughened to scatter the incident waves.

The resonant frequency of the bulk mode transducers on this sample was beyond the range of the RX-Meter and thus another technique had to be used. A special mounting was prepared for the sample and is shown in Fig. 5.5 with the sample in place. Connection was made to the "side bars" of the ID transducer as before, using a doubled length of 0.010" gold wire and a pressed indium contact. Contact to the center dot was by means of a pointed probe. All of the parts of the special holder shown in Fig. 5.5 were gold plated for minimum resistance. The instrument used to determine the bulk wave characteristics was a Hewlett-Packard Network Analyzer, type 8410A, with a type 8741A Reflection Test Unit. The signal source was a Wavetek, model 2001, sweep oscillator. It was expected that the reflection coefficients determined by the network analyzer would be very close to unity; and thus extreme care had to be taken in performing the measurements, for a small error in the observations could result in a large error in the final result. For accurate reading and interpolation, both reflection coefficient and phase were plotted on graph paper using a dual-pen Hewlett Packard X-Y recorder. (One pen provided frequency marker points from the oscillator, while the other recorded the desired information.) The measurements proceeded in the following manner:

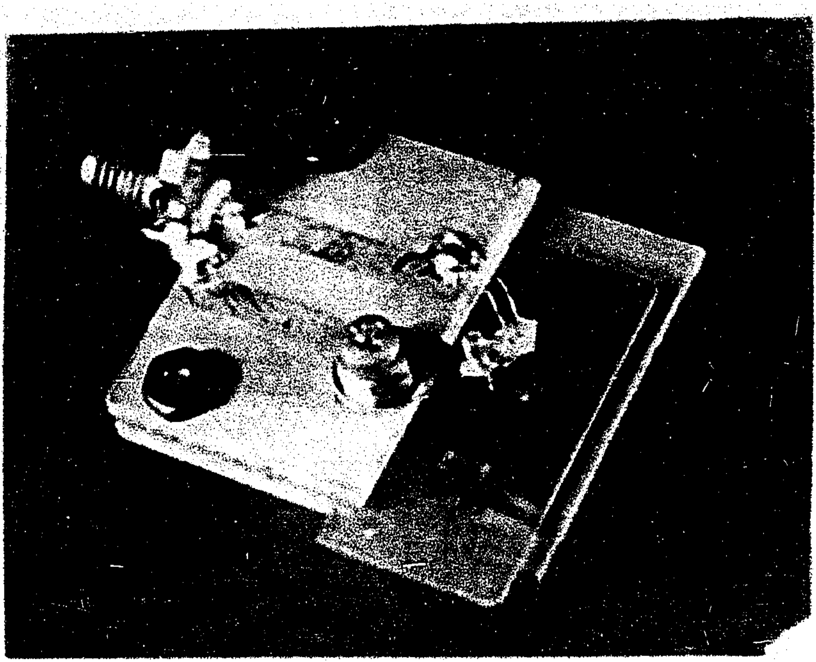

Figure 5.5 – Showing the method of mounting the surface wave samples to perform bulk wave measurements

(1) With the oscillator adjusted for a slow sweep rate, the output of the Reflection Test Unit was terminated in a short circuit and the reflection coefficient recorded as a function of frequency.

(2) Using an OSM to APC-7 adapter, the holder with sample was connected to the Reflection Test Unit, but with the probe shorted to the pressed indium contact. In this mode the reflection coefficient was measured.

Steps (1) and (2) allow the reflection coefficient of the holder, up to the probe tip which contacts the sample, to be determined.

(3) Step (1) was repeated using another piece of graph paper.

(4) Step (2) was repeated, but this time with the probe tip contacting the metallized dot on the ZnO.

Steps (3) and (4) give the reflection coefficient of both holder and sample. Steps (1) - (4) were then repeated for the phase angle associated with the reflection coefficient.

By following this procedure one can then calculate the values of R_p and C_p for the bulk wave transducer as a function of frequency. Figure 5.6 shows the measured points for R_p, with estimated maximum experimental error*, for one of the bulk wave transducers. There is some spread evident in the measured points, which may still be caused by reflections from the back surface; however, the points are clustered reasonably well around the resonant point. The area of the metallic dot was accurately measured using a microscope with a micrometer eyepiece. In order to calculate the response of the bulk wave transducer, one must know the material constants of SiO_2, and the following values were used[10]:

---

*This error is estimated on the basis of the probable error in measuring the reflection coefficient and phase angle.

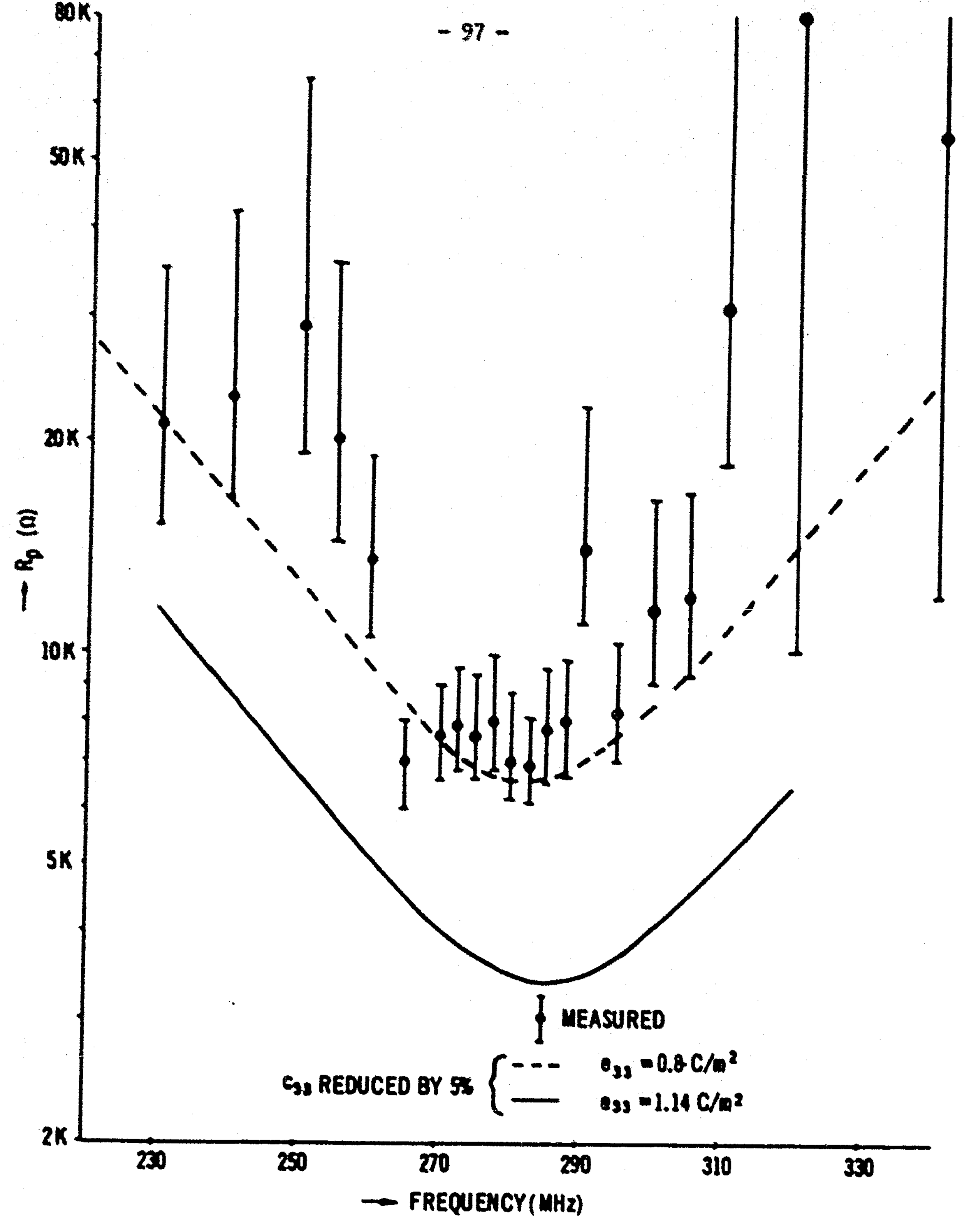

Figure 5.6 – Bulk wave measurements on sample ZMU – 50C

$$\begin{aligned} c_{11} = c_{33} &= 0.784 \times 10^{11}\ \mathrm{N/m^2} \\ c_{44} &= 0.313 \\ c_{13} &= 0.158 \\ \rho &= 2202\ \mathrm{Kg/m^3}\ . \end{aligned} \tag{5.5}$$

(These values were also used for the surface wave calculations.) To obtain the fitted curve shown in Fig. 5.6, it was necessary to use a value of $e_{33} = 0.8\ \mathrm{C/m^2}$ for the ZnO, and to reduce the elastic constant c_{33} for ZnO by about 5%. (The reduction in c_{33} was required to bring the calculated and measured resonant frequencies into correspondance. Since sputtered or evaporated films are composed of "micro-crystallites", it is not surprising to observe that the sputtered film is slightly "softer" than the single crystal material.) A calculated curve using the values given by (5.4) for single crystal ZnO is included for comparison in Fig. 5.6. The required reduction in e_{33}, to obtain the fitted curve, is about 30% and represents a reduction in the bulk wave coupling constant (K^2) of about 50%. Applying the 30% reduction to all of the piezoelectric elements of ZnO previously given, and reducing the elastic constants by 5%, gives the following for the "reduced" values of the ZnO crystal constants*:

$$\begin{aligned} c_{11} &= 1.990 \times 10^{11}\ \mathrm{N/m^2} & e_{15} &= -0.413\ \mathrm{C/m^2} \\ c_{33} &= 2.01 & e_{31} &= -0.426 \\ c_{44} &= 0.404 & e_{33} &= 0.8 \\ c_{13} &= 1.0\ . \end{aligned} \tag{5.6}$$

(The density and the dielectric constants were not altered.)

Using the method previously described, the R_s of the transducer on

---

* Due to the "quasi-isotropic" nature of ZnO, it is logical to assume that all of the constants of a similar type will be affected in the same manner.

this sample was found to be about 10 Ω. The calculations for the sample ZMU-50C were then repeated, using the reduced crystal constants in (5.6) above and the measured value of R_s, resulting in the theoretical curve shown in Fig. 5.7. Also included in Fig. 5.7 are the experimental points from Fig. 5.4 and a calculated curve using the single crystal values of (5.4). It should also be mentioned that these samples did not show any obvious photoelectric effects, and hence the measurements were carried out in subdued light but not in the dark as was the case for the ZnO free surface samples.

As can be seen from Fig. 5.7, the agreement between the calculated values, using the reduced material constants, and the measured values is very good. Not only is the resonant value of R_p correctly predicted but the peak-to-peak variation in C_p is also correct, as well as the general shape of both R_p and C_p curves.

5.5.2 Sample ZMU-63/58

Both of the transducers on this sample were measured, and were found to be identical with respect to their admittance characteristics. Thus, the experimental points shown in Fig. 5.8 apply to both transducers. The theoretical curve shown in Fig. 5.8 was calculated using the reduced values of piezoelectric and elastic constants, given by (5.6), that were used for the sample ZMU-50C. The value of R_s was determined in the manner described previously, and employed in the theoretical calculations. One can see that, except for a relative frequency shift of about 1 MHz (1.5%), the agreement between the calculated curve and the measured points is very close, even in the side lobes of the R_p curve. The exact origin of the relative frequency shift between the two curves is not known. The thickness/

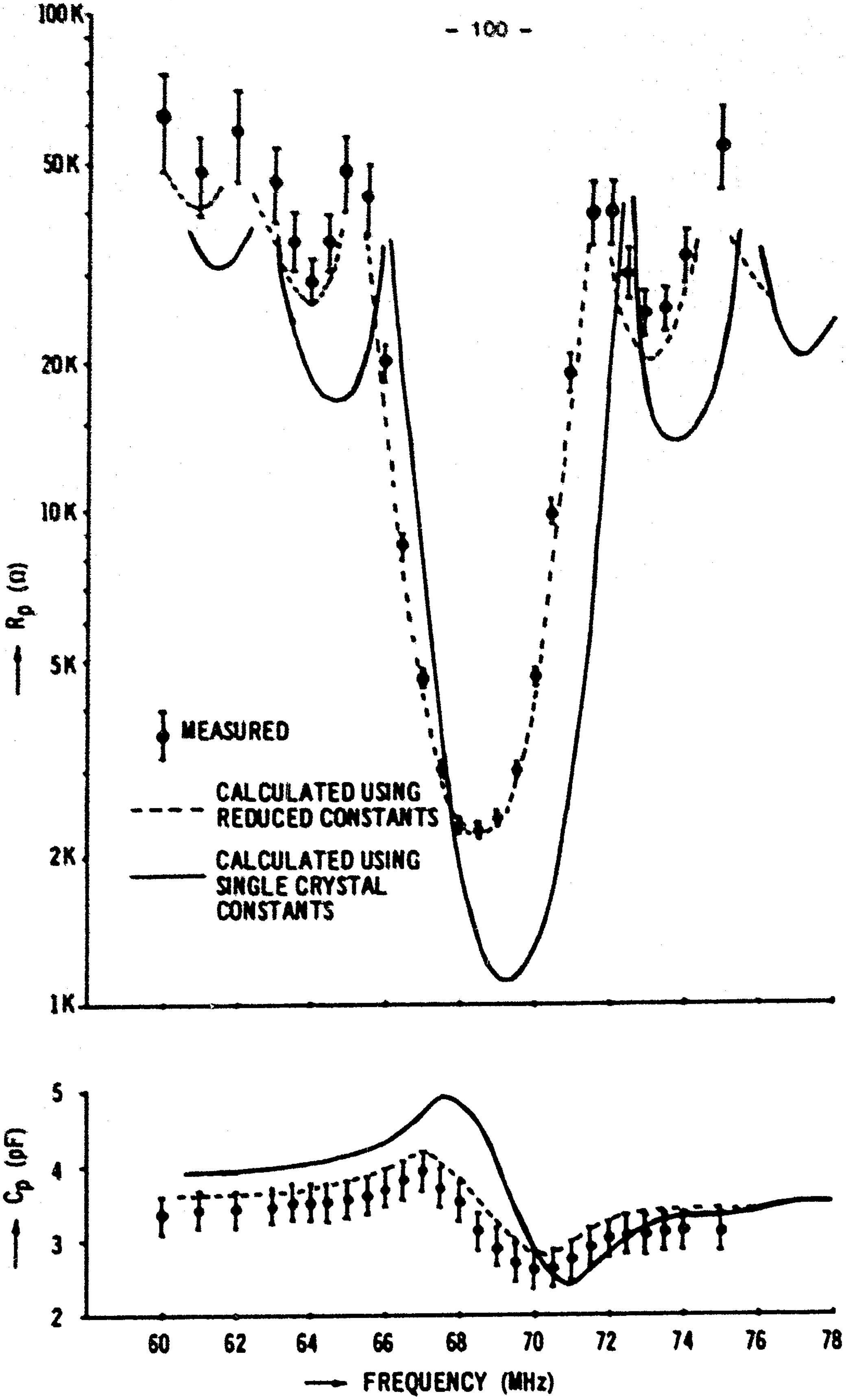

Figure 5.7 ZnO – SiO_2 sample ZMU – 50C

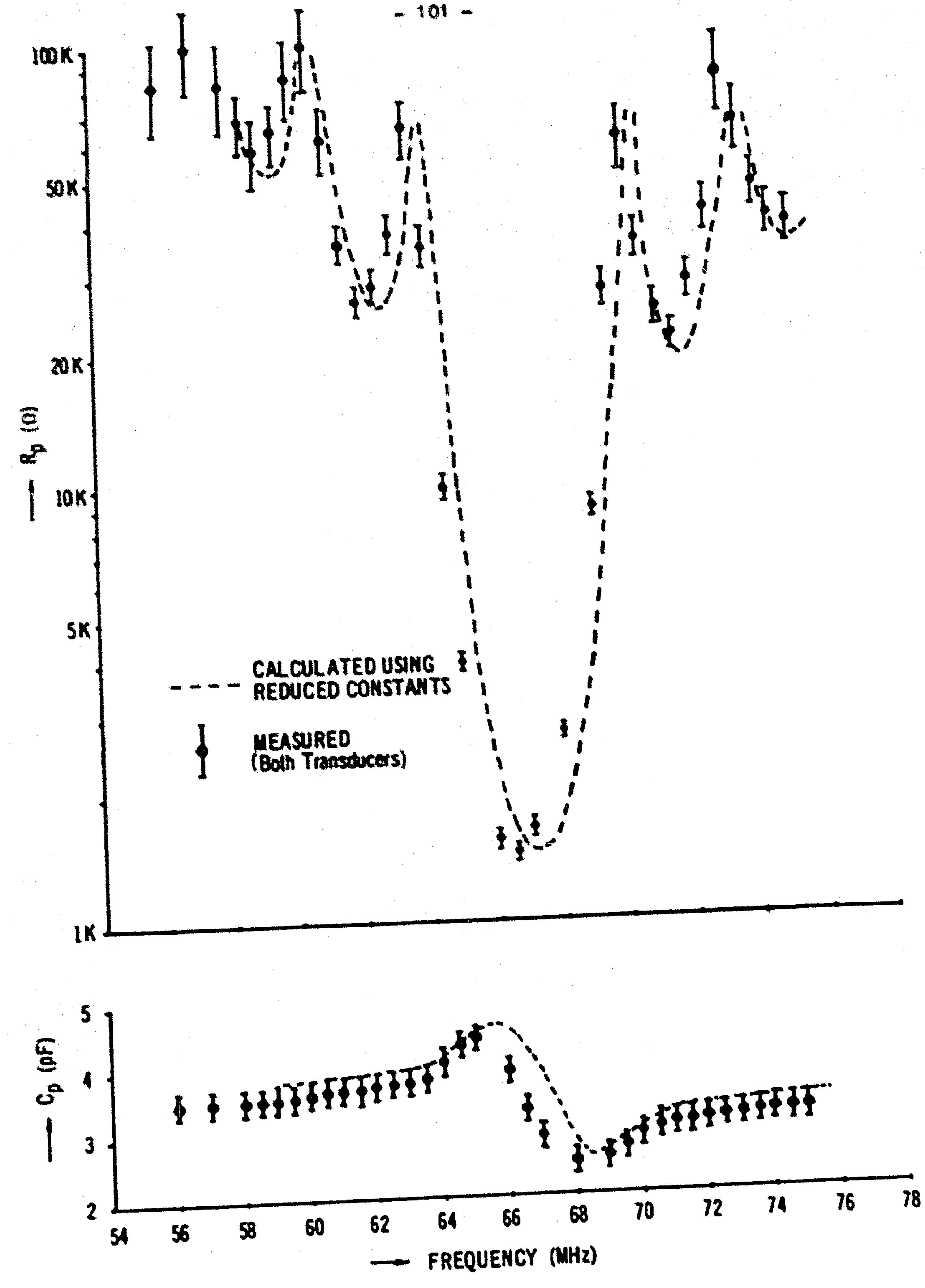

Figure 5.8 ZnO – SiO_2 sample ZMU – 63/58

wavelength ratio for this structure is about 0.3 at resonance; and the system of $ZnO-SiO_2$ is not sufficiently dispersive*, at that value of H/λ, to explain the shift by an error in the thickness measurement[30]. Rather, it may be the result of having produced the ZnO layer by two separate depositions. If the bond between the separate depositions was slightly "softer" than the rest of the film, the resulting surface wave velocity could be depressed, as is known to be the case with a "sliding bond"[1].

5.5.3 Sample ZMO-68/50B

The two transducers on this sample were measured in the manner used for the previous two samples and were found to be almost identical. The experimental points for both transducers are shown in Fig. 5.9, along with the theoretical curve. The value of 14 Ω for R_s was determined in the usual fashion and accounted for in the calculated curve. An attempt was made to measure the piezoelectric constant e_{33} for this sample, in the same manner used for the sample ZMO-50C. However, due to the greater thickness and hence increased wavelength of the bulk wave, the reflections from the back surface could not be sufficiently eliminated to enable an accurate measurement. Thus, the values of the piezoelectric and elastic constants used in the calculated curve for this sample were the same as those used previously and given by (5.6).

As can be seen, the agreement between the measured results and theory is very good, even assuming that the material constants for the thick film are the same as those for the thinner films. There is very little evidence of a relative frequency shift between the measured and calculated curves

---

* See Fig. 6.4, page 119.

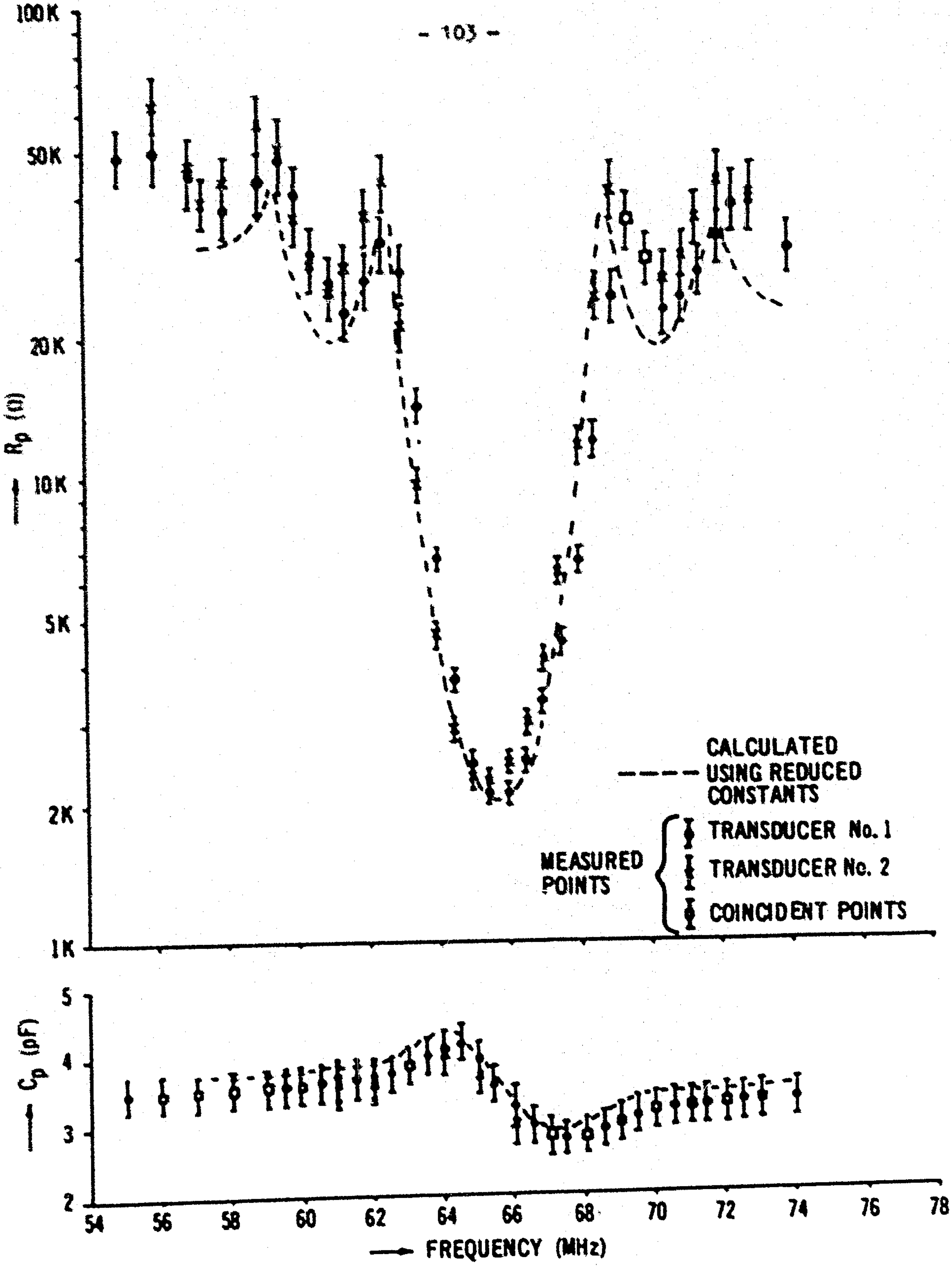

Figure 5.9 ZnO – SiO_2 sample ZMU 68/50B

for this sample, since even the positions of the nulls in the measured and calculated R_p curves agree very closely.

5.5.4 Comparison with an "Equivalent Circuit" Approach

Another form of comparison can be obtained from the single crystal curve of Fig. 5.7 for the sample ZMU-50C. The "resonant" frequency for this structure, using single crystal constants for ZnO, is 69.2 MHz, with an R_p of 1.1 KΩ, a capacitance of 3.5 pF and a 'kH' of 1.67. (Since the "active" portion of the transducer susceptance equals zero at "resonance", the total static capacitance of the transducer, C_T, equals 3.5 pF.) From the "equivalent circuit" approach of Smith et al.[58], the radiation conductance at "resonance" can be written

$$G(\omega_r) = (4/\pi)K^2(\omega_r C_T N) \qquad ; \qquad (5.7)$$

where K is the "electro-mechanical coupling constant", and N is the number of finger pairs (periodic sections) in the transducer. The term K^2 is defined by[58]

$$K^2 = 2F|\Delta v/v| \qquad , \qquad (5.8)$$

where F is the "filling factor".

Substituting the above calculated values into (5.7) yields a value of $K^2 = 2.34 \times 10^{-2}$. That we have assumed an R_s of 10 ohms for this transducer has negligible effect on the value of K^2. For a structure of ZnO on fused quartz, the theoretical analysis of Solie[61] predicts a value of $\Delta v/v$ equal to 1.1×10^{-2}, for this value of 'kH'*. The "filling factor" necessary to relate our theoretically determined value of K^2 to the value of

---

* See Fig. III.19, pp. 77 of ref. 61.

$\Delta v/v$ determined by Solie is

$$P = \frac{K^2}{2(\Delta v/v)} = 1.06 \;;$$

which compares favorably with $P = 1.0$, the value commonly used for $LiNbO_3$ free surface excitation[58].

5.6 Summary

The results presented in this chapter have shown that, knowing only the material parameters, it is possible to accurately predict the complex admittance characteristics of an ID transducer used to launch acoustic surface waves in layered structures. While the real part of the admittance has been previously determined in this fashion for free surface propagation[36], we have also determined the imaginary part. The extension of the theory to layered structures provides for implicit inclusion of the dispersion present in such structures. Although the analysis has been concerned with low coupling materials, it is useful to observe that the approximations which have been made do not seriously affect the accuracy of the results when compared to measurements made on X-Y cut Z propagating $LiNbO_3$. (It may be that with other orientations of $LiNbO_3$ the theoretical and measured results would not agree so well.) It is not surprising to observe that the calculated real and imaginary parts of the admittance of the ID transducer appear to have the same form that is predicted by the familiar "Stanford Model"[58]; however, more will be said concerning this fact in a later section.

The results using the $ZnO-SiO_2$ structures indicate that the ZnO films deposited by M. Holland are consistent in their quality and probably represent the current "state-of-the-art", in spite of their reduced piezoelectric activity.

We have also shown that theoretical results using single crystal constants for layered structures compare favorably with attempts to use an "equivalent circuit" approach[61].

CHAPTER VI

SURFACE WAVE BEHAVIOUR WITHIN THE TRANSDUCER

6.1 Introduction

The preceding chapter used comparison between the measured and calculated admittance characteristics of ID transducers to give credence to the theoretical analysis. However, the calculation of such simple curves, though useful in its own right, was not a primary aim of this work. Rather, we are interested in the more basic wave behaviour associated with an ID transducer when used as a launching structure for acoustic surface waves. The use of an equivalent circuit model[58] enables one to predict, with reasonable accuracy, the admittance curves that have been presented in Chapter V; however, such an approach does not show wave behaviour within the transducer region. Joshi and White[36] were able to predict the real part of the transducer admittance; however, their analysis was not extended into the transducer region and hence they did not calculate the "active" portion of the transducer susceptance or demonstrate the wave behaviour inside the ID transducer. On the other hand, our analysis has been extended into the transducer region and hence is capable of calculating the "active" portion of the transducer susceptance, as was demonstrated in Chapter V, as well as describing the wave behaviour within the transducer region.

This chapter is devoted, primarily, to the presentation of wave behaviour within the ID transducer and explanations thereof. We will show how the basic wave behaviour can be described on the basis of a simple physical "model" involving two surface waves which propagate in opposite directions and whose magnitude changes as they travel through the ID transducer. In Chapter VII, these same results will be derived on the basis of a simple mathematical "model".

The computational procedure which has been developed will also be used to demonstrate the effect of dispersion on the transducer characteristics and to study the effect of different piezoelectric constants for ZnO on the transducer admittance of a free surface and layered structure.

6.2 Surface Waves Within the ID Transducer

The analytical and computational procedure developed in Chapters II and IV allow one to calculate and plot the total particle displacements* within the transducer region as a function of frequency. In this section we will present results calculated for the layered structure ZMU-58/63, discussed in section 5.5.2. These results are presented as being typical of both the particle displacements and surface wave behaviour within the region of the ID transducer for both layered and free surface structures.

Figure 6.1 shows the magnitude of the x and z components of the total particle displacements, $|V_x|$ and $|V_z|$, at $z = 0$, over the range $-D/2 \leq x \leq 0$, for five different frequencies. The structure ZMU-58/63 has a total of twenty finger pairs, hence, there are twenty fingers in the range $-D/2 \leq x \leq 0$. Since symmetry about $x = 0$ has been assumed, it is not necessary to present the particle displacements for $x > 0$. The analytical procedure determines the true particle displacements for a signal of 1-volt (peak) across the fingers of the ID transducer; and thus the displacements shown in Fig. 6.1 are absolute, however, a logarithmic amplitude scale has been used for ease of presentation. The horizontal scale indicates the relative

---

* The "total particle displacements" represent the sum of both particular integral and homogeneous wave solutions within the transducer region, given by (2.45) in section 2.2.7.

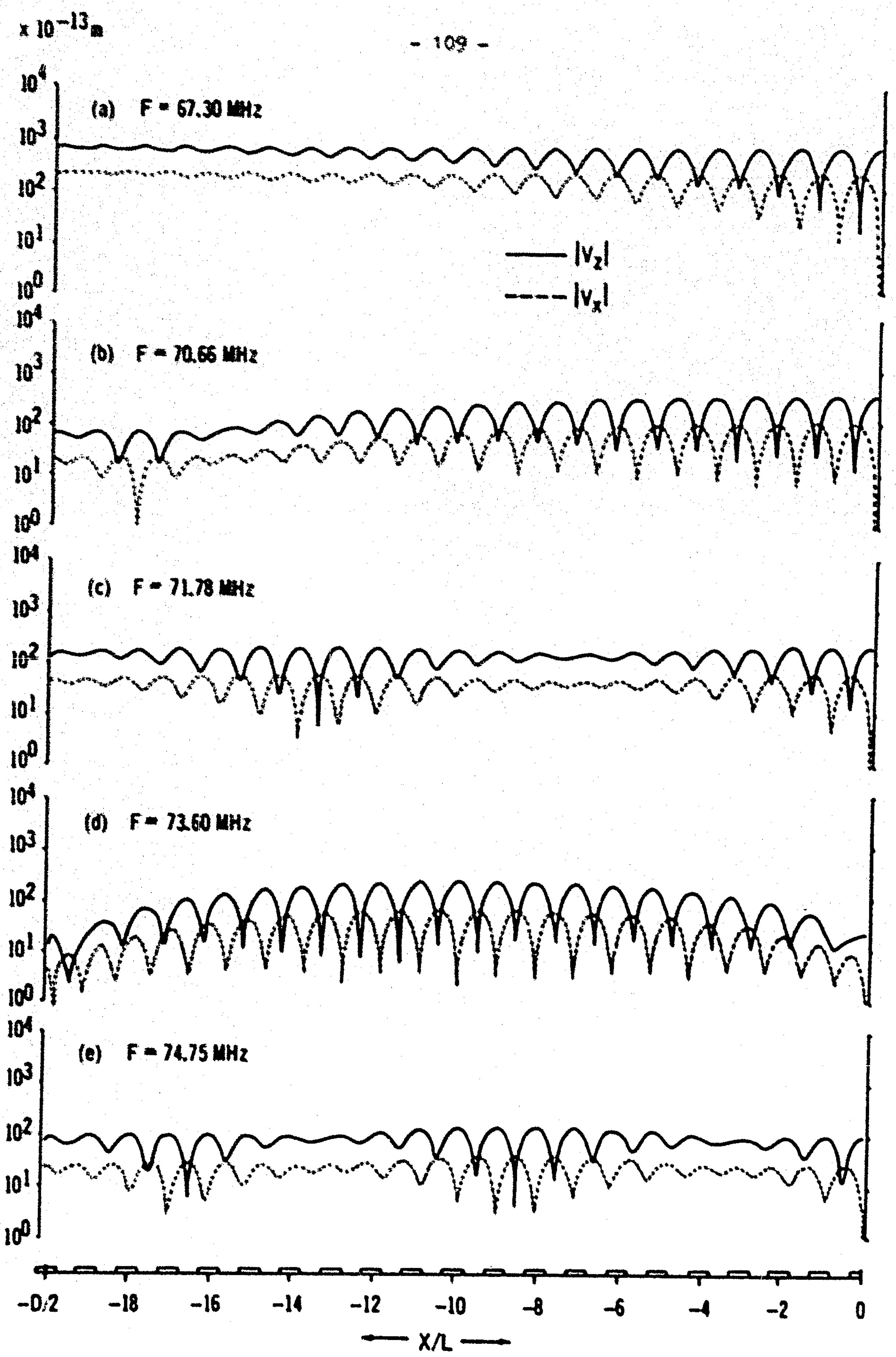

Figure 6.1 – Magnitude of particle displacements within the transducer

positions of the fingers of the ID transducer, in the range $-D/2 \leq x \leq 0$. The frequencies chosen for this figure are:

(a) 67.30 MHz - the "resonant" frequency of the device, f_r, $G = 0.715$ mmhos

(b) 70.66 MHz - slightly greater than the frequency of the first "null" above f_r, $G = 0.0076$ mmhos

(c) 71.78 MHz - approximate center frequency of the first "side lobe" above f_r, $G = 0.039$ mmhos

(d) 73.63 MHz - approximate frequency of the second "null" above f_r, $G = 0.00025$ mmhos

(e) 74.75 MHz - approximate center frequency of the second "side lobe" above f_r, $G = 0.015$ mmhos.

Where, "resonant", "null" and "side lobe" refer to the R_p characteristics of this device as shown in Fig. 5.8, section 5.5.2, and G refers to the calculated radiation conductance of the transducer, assuming $R_s = 0$.

At first glance, the "standing wave" patterns* shown in Fig. 6.1 may appear somewhat unusual and difficult to interpret; however, they can, in fact, be explained in a very simple manner. Let us begin by assuming that each finger pair of the ID transducer launches only surface waves, and that they are generated equally in both the positive and negative x-directions. Thus, one can view the surface wave which is radiated by the transducer at $x = D/2$ as a superposition of all of the waves generated in the positive x-direction, by all of the finger pairs. An equivalent viewpoint is to think of this wave as starting at $x = -D/2$ and travelling through the transducer, gathering contributions from each finger pair, until it is radiated at $x = D/2$. In a similar fashion, one can imagine that the wave which is radiated by the transducer at $x = -D/2$ starts at $x = D/2$. These two surface

---

* A time dependence $\exp(-i\omega t)$ is still implied, for every point shown.

waves, propagating in opposite directions through the transducer region, will interact with each other to form standing wave patterns, the characteristics of which will be determined by the relative amplitudes of the two waves at each point (x,z). A "model" of this nature was anticipated in section 2.2.7, equation (2.45), when we divided the total wave solutions within the transducer region into two "wave packets", $V_j^+(x,z)$ and $V_j^-(x,z)$, each composed solely of wave-like terms propagating in the positive or the negative x-direction, respectively. It was then convenient to define "amplitude factors", $AP_j^{(\pm)}$, by

$$AP_j^+(x,z) = V_j^+(x,z)/e^{ik_s x} \qquad (2.46a)$$

and

$$AP_j^-(x,z) = V_j^-(x,z)/e^{-ik_s x} , \qquad (2.46b)$$

where k_s is the propagation constant for the surface wave, as representing the relative amplitudes (complex) of the j^{th} component of the "wave packets" V_j^+ and V_j^-, respectively. Comparing the above to our simple "model" consisting of two surface waves propagating in opposite directions through the transducer, we see that they are analogous. The two surface waves are identical to the "wave packets", and the "amplitude factors" will describe the relative amplitudes of the two surface waves as they propagate through the transducer.

Figure 6.2 shows the magnitude of the amplitude factor for the z-component of the wave packet propagating in the positive x-direction, $|AP_3^+|$, at $z = 0$, for the same frequencies that were used in Fig. 6.1. The magnitude of the amplitude factor for the z-component of the wave packet propagating in the opposite direction, $|AP_3^-|$, will be the mirror image, about $x = 0$, of

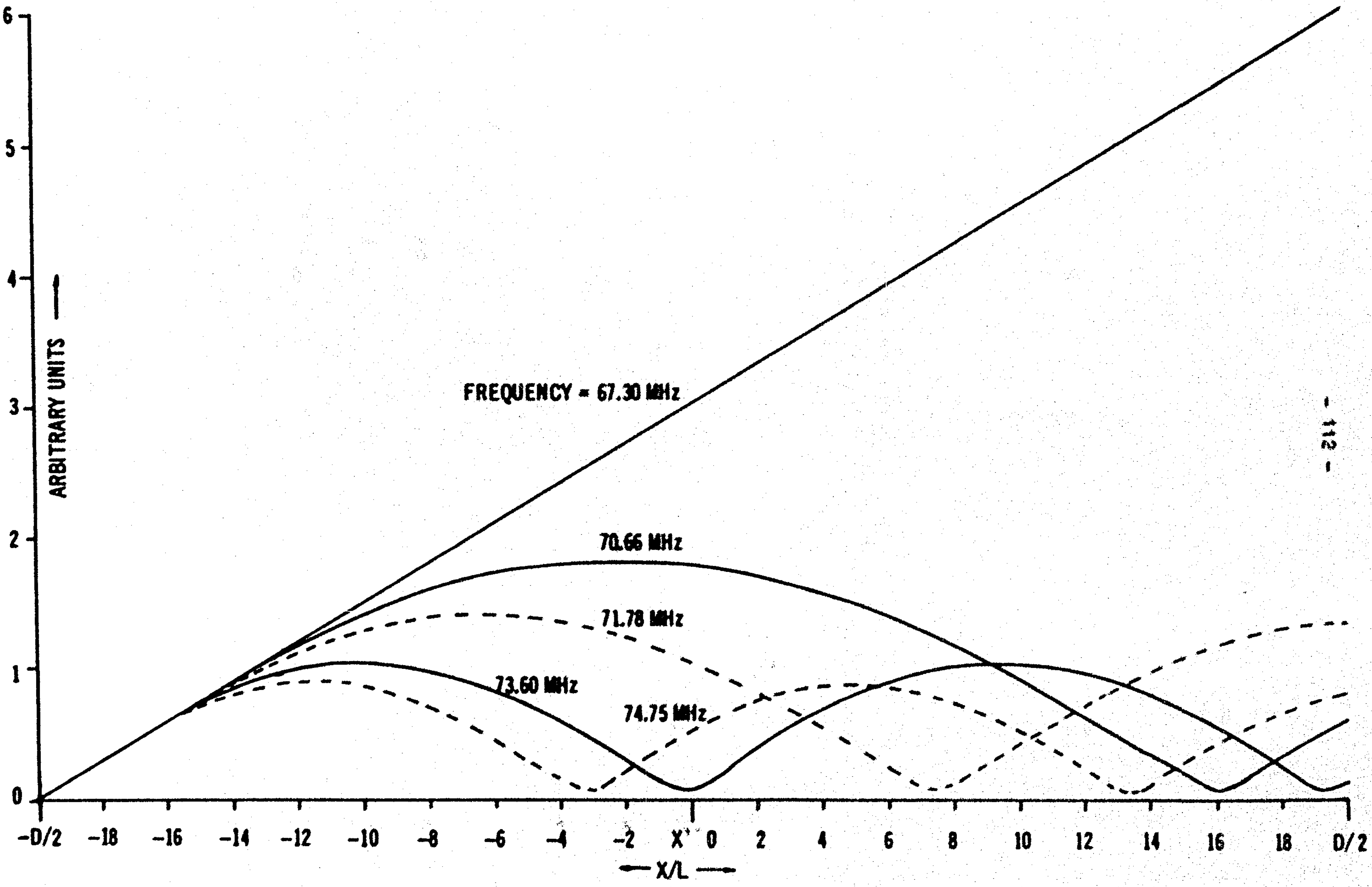

Figure 6.2 – $|AF_3^+|$ calculated from general theory

the curves shown in Fig. 6.2. The magnitude of the amplitude factors for the x-component of both wave packets will be essentially the same as those of the z-component, though the phase at each point may be different.

At the resonant frequency, 67.30 MHz, the surface wave which is propagating within the transducer is exactly in step with the applied signal; and hence it gets a "push", at exactly the right time, from each finger pair*. Thus, the wave linearily increases with distance from its start at $x = -D/2$ until it is radiated at $x = D/2$, as shown in Fig. 6.2. At the frequency which is approximately equal to that of the first "null", 70.66 MHz, (we have chosen the "null" $> f_r$, however, the "null" $< f_r$ will behave in a similar fashion) the surface wave begins to build up linearily from $x = -D/2$, as was the case at resonance. However, the wave is not quite in step with the applied signal and hence it slowly slips out of phase with respect to the applied signal, as it passes through the transducer. At about $x = 0$, the surface wave is 90° out of phase with the applied signal and cannot receive any additional energy. As the wave continues, it will give up energy until it has reached zero amplitude, at which point it is 180° out of phase. As seen in Fig. 6.2, the wave amplitude, $|AF_3^s|$, is approximately zero at a point about four fingers from the end of the transducer, for this frequency. Since the wave is still within the transducer region, the process will start again, as it did at $x = -D/2$, and continue until the wave is radiated by the transducer. As $|f - f_r|$ increases, the phase of the surface wave with respect to the applied signal changes more rapidly as the

---

* In reality, it is the particles which are being moved about a fixed point by the applied signal (particular integral solution); and if their motion is exactly in step with that of the wave, as it passes, the wave will increase in amplitude.

wave propagates through the transducer; and thus the magnitude of the amplitude factor changes more rapidly with distance from $x = -D/2$, as seen in Fig. 6.2.

Returning now to the explanation of the standing wave patterns in Fig. 6.1, let us consider Fig. 6.3 which shows the magnitude of the amplitude factors for the z-component of the wave packets (surface waves) which are propagating in both directions, over the range $-D/2 < x < 0$. The same frequencies that are used in Figs. 6.1 and 6.2 are also used in Fig. 6.3. One can qualitatively explain the patterns of Fig. 6.1, using the curves of Fig. 6.3, by remembering that for two waves of equal wavelength, but which are propagating in opposite directions, the maximum and minimum amplitudes of the resulting standing wave pattern are $|AF^+| + |AF^-|$ and $|AF^+| - |AF^-|$, respectively. Where $|AF^+|$ and $|AF^-|$ are the magnitudes of the two waves. Thus, if $|AF^+|$ and $|AF^-|$ are equal, the standing wave pattern will have the maximum peak-to-peak amplitude; whereas, if either $|AF^+|$ or $|AF^-|$ is zero, the standing wave pattern will be constant in amplitude. We have assumed that the transducer is symmetric about $x = 0$, with the result that $|AF^+| = |AF^-|$ at $x = 0$. Hence, the standing wave patterns will always have a large peak-to-peak amplitude in the vicinity of $x = 0$, as seen in Fig. 6.1. However, providing that the transducer is of equal finger spacing throughout, the standing wave pattern will always have a large peak-to-peak amplitude in the vicinity of the center of the transducer, irrespective of the location of the origin. It should also be noted that if the origin is centered between an adjacent pair of fingers, and the transducer is symmetric about this point, the standing wave patterns for $|V_x|$ will have a maximum at $x = 0$, while those for $|V_z|$ will have a minimum. In light

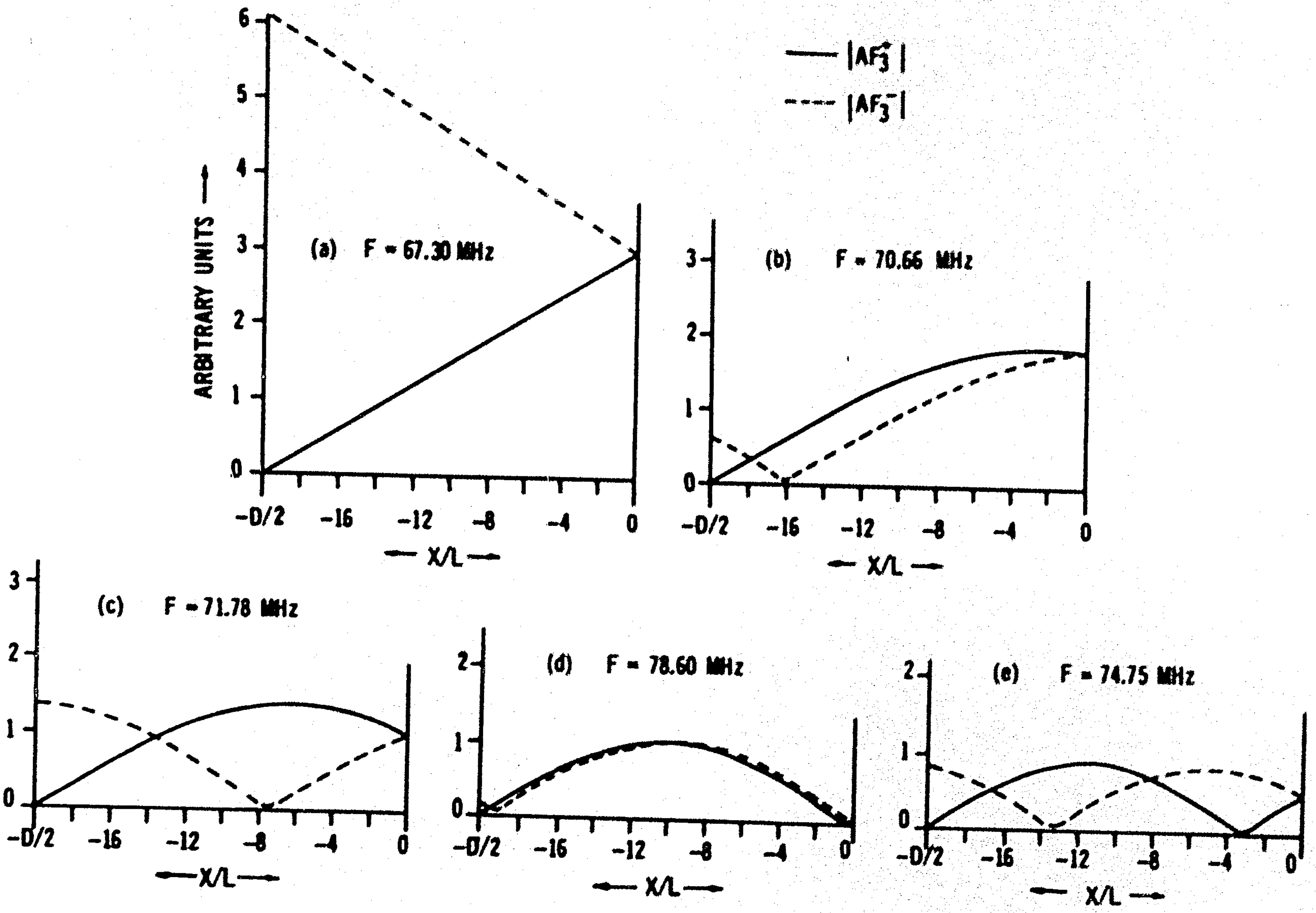

Figure 6.3 – $|AF_3^+|$ and $|AF_3^-|$ over range (−D/2, 0)

of Fig. 6.3, the explanations for the remaining portions of the standing wave patterns shown in Fig. 6.1 is very straightforward. For a frequency of 67.3 MHz, Fig. 6.3a indicates that the standing wave pattern will decrease linearily from $x = 0$, until it becomes constant at $x = -D/2$, as is shown in Fig. 6.1a. Figure 6.3b shows that the standing wave pattern should have a "maximum" in the vicinity of the 18th finger from the center and a "minimum" at about the 16th, after which the standing wave pattern will gradually increase until reaching a "maximum" at $x = 0$. This characteristic is apparent in Fig. 6.1b. The other standing wave patterns can be explained in a similar fashion, it would be repetitious to discuss each one of them.

In the above analysis of the wave behaviour shown in Fig. 6.1, we have lost sight of the particular integral solutions which represent the forced particle motion in response to the applied signal. These terms are present in the amplitude factors $AP_j^+(x,z)$ and $AP_j^-(x,z)$, as defined by equations (2.46), but are very small, and hence do not appear except when the "surface wave" terms vanish. It is for this reason that the amplitude factors shown in Fig. 6.2 never quite go to zero at points other than $x = -D/2$. (Remember that the edges of the transducer region, $|x| = D/2$, represent discontinuities in the driving potential function, as defined by equation (2.10), and in Appendix C.3 it was impossible to evaluate one portion of the homogeneous solutions at this point.) For a frequency of 73.63 MHz, Fig. 6.3d shows that at $x = 0$ and $x = -D/2$ there are virtually no surface waves present and it is the contributions from the forced particle displacements that cause the edges of Fig. 6.1d to appear distorted. In the remaining patterns shown in Fig. 6.1, the surface wave activity is sufficient to obscure the effects of the forced motion.

Thus far we have only considered the wave behaviour within the transducer, at $z = 0$, and for a single type of structure. It is, however, obvious that above and below $z = 0$ the same basic behaviour shown in Figs. 6.1 - 6.3 will apply, though the relative scale factors may change from one value of z to another. Likewise, the same basic characteristics will apply to other types of structures, be they layered or free surface, plated or unplated. The only variation will occur when the fingers of the transducer are all driven in phase and of the opposite polarity to a metallic plating, referred to as "unipolar" drive in section 2.1.1. In this case, the effective "wavelength" of the transducer is halved, and the "resonant" frequency, f_r, is doubled, providing the transducer dimensions are not altered. Thus, the "wavelength" of the standing wave patterns of Fig. 6.1 will be halved: however, for the same values of $(k - k_r)/k_r$ as used in Figs. 6.1 - 6.3[*], the amplitude factors and the positions of the "maxima" and "minima" of the standing wave patterns will be as shown, with the possible exception of a constant scale factor. The wave number k is used, instead of frequency, to account for the dispersion present in layered structures.

We have thus shown how the wave behaviour within an ID transducer can be adequately described by a "two surface-wave approach"; in which the surface waves start at opposite ends of the transducer and propagate through it to the other end, at which point they are radiated into the surrounding media. As they travel through the transducer, the change in amplitude of the surface waves is determined by the relative phasing between the waves

---

[*] 'k' $= \omega/v$, where v is the phase velocity of the surface wave, k_r is the value of k at "resonance".

and the applied signal. Chapter VII will demonstrate how this same behaviour can be predicted on the basis of a very simple mathematical model that can also be used to determine the transducer admittance. It was also indicated that the contributions to the total particle displacements from the forced particle motion are very small and their effect can only be observed when the surface wave contributions are negligible. The surface wave components can be made to vanish in certain regions of the transducer by operating at an appropriate frequency, as shown in Figs. 6.1 - 6.3, or by exciting the transducer at a frequency which is far removed from the "resonant" frequency.

6.3 Admittance Characteristics of an ID Transducer on a Highly Dispersive Structure

The structures which have been studied thus far were either non-dispersive (free surface), or had very little inherent dispersion ($ZnO - SiO_2$). The general theory which has been developed for the study of layer excitation has the effects of dispersion implicitly included, and it is interesting to illustrate the effect of a large amount of dispersion on the electrical characteristics of an ID transducer. Figure 6.4* shows the surface wave velocity as a function of H/λ for layered structures, using ZnO as the layer, with various substrates. It can be observed that the $ZnO - SiO_2$ system is not very dispersive, as previously mentioned. However, a structure utilizing ZnO on either Si or sapphire should show considerable dispersive effects. Figure 6.5 shows the R_p characteristic, as a function of frequency, for an ID transducer located at the interface of a $ZnO - Al_2O_3$ structure**. The transducer is assumed to have the following

---

* From Hickernel, et al[20].

** The effect of dispersion on the C_p characteristic, for this system, is negligible, and thus the C_p curve is not shown.

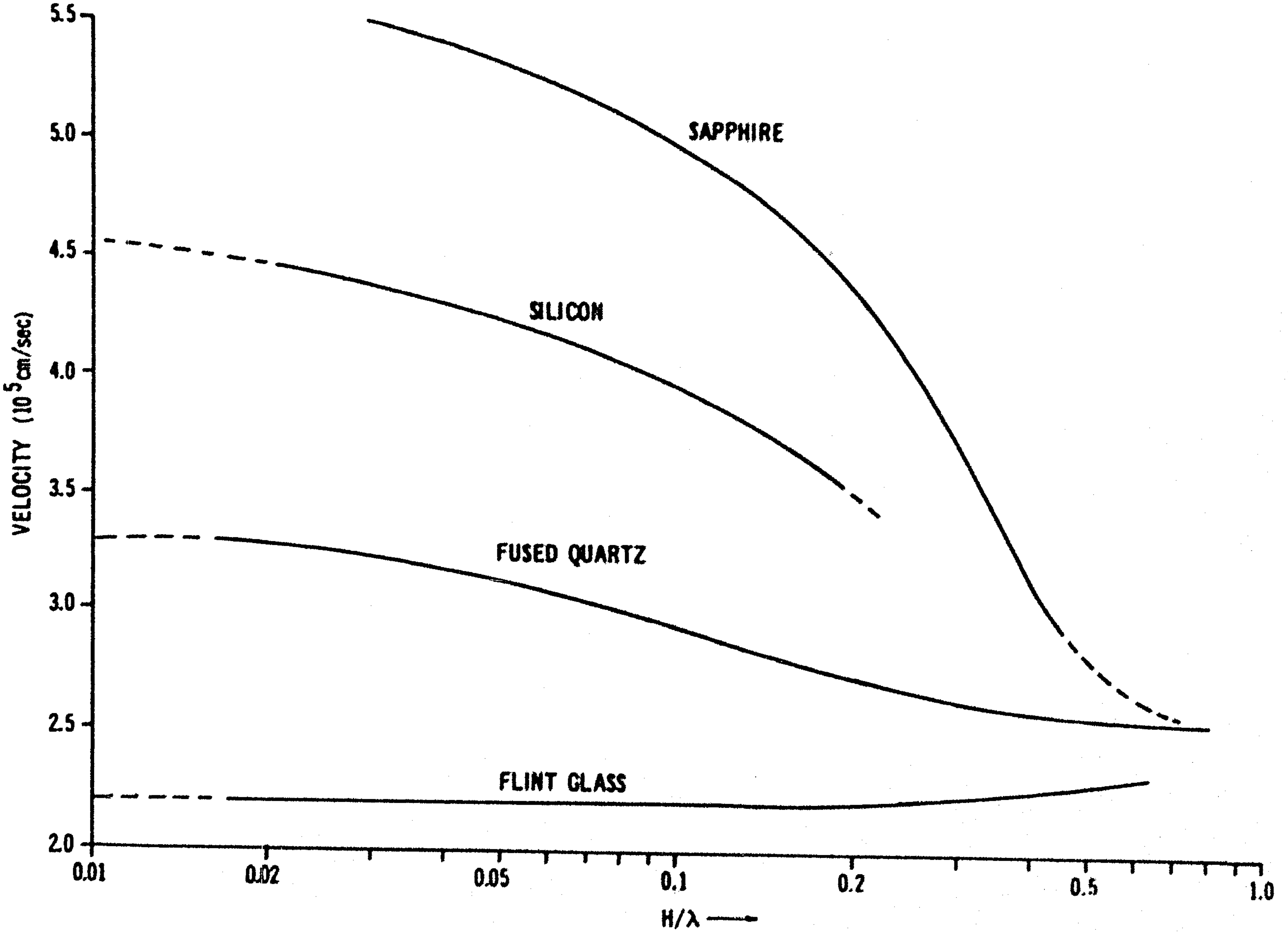

Figure 6.4 – Velocity of ZnO on selected substrates (from Hickernell et al.)

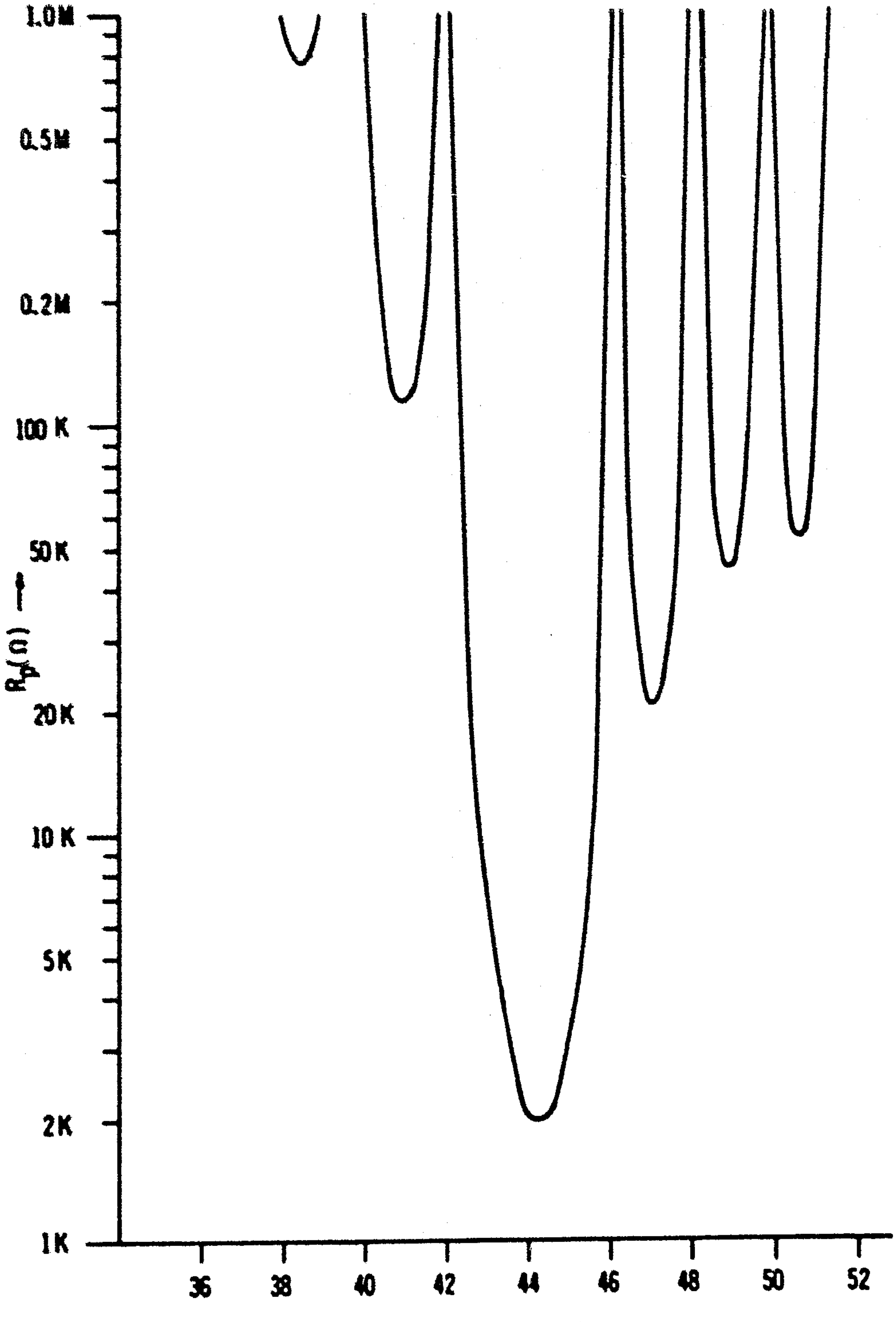

Figure 6.5 – R_p characteristic of an ID transducer with a 20 μm ZnO layer on Al_2O_3

dimensions:

$$L = 50.8\ \mu m\ (\lambda_r = 101.6\ \mu m)$$
$$d = 25.4\ \mu m$$
$$W_o = 4.5\ mm\ ,$$

and consists of 15 finger pairs. Since these calculations are not being compared with measured data, it is convenient to assume that $R_s = 0$. Both materials are assumed to be oriented such that their c-axes are normal to the interface. The material constants to be used for the ZnO were given by (5.4), and are:

$$\begin{array}{llll} c_{11} = 2.097 \times 10^{11}\ N/m^2 & & e_{15} = -0.59\ C/m^2 & \\ c_{33} = 2.109 & & e_{31} = -0.61 & \\ c_{44} = 0.425 & & e_{33} = 1.14 & (5.4) \\ c_{13} = 1.051 & & \rho = 5676\ kg/m^3 & \\ & \epsilon_1 = 8.33, \quad \epsilon_3 = 8.84\ . & & \end{array}$$

The appropriate material constants for the Al_2O_3 are[8]:

$$\begin{array}{lll} c_{11} = 4.902 \times 10^{11}\ N/m^2 & & \\ c_{33} = 4.902 & & \\ c_{44} = 1.454 & & (6.1) \\ c_{13} = 1.130 & \rho = 3986\ kg/m^3 & . \end{array}$$

An "isotropic dielectric constant" equal to 10 was used; and since Al_2O_3 is non-piezoelectric, all of the $e_{ij} = 0$. The ZnO layer was chosen to be 20 μm thick which gives a "resonant" value of $H/\lambda \simeq 0.2$. This places our calculation in the region of maximum dispersion for a structure of this nature. The presence of dispersion is apparent in the asymmetry of the R_p curve of Fig. 6.5, about the center frequency. One will observe the relative "bunching" of the "side lobes" for frequencies greater than f_r, as compared to the "side lobe" spacing for frequencies less than f_r. The R_p characteristics for the $ZnO - SiO_2$ system, shown in Figs. 5.7 - 5.9* of the previous chapter, will also be asymmetric but the effect is too small to be noticed. Additional calculations were performed for the $ZnO - Al_2O_3$ system, using layer thicknesses of 15 μm and 60 μm. The calculated values of R_p at "resonance", for these additional structures, are compared with that calculated for a 20 μm layer in Table 6.1, below.

TABLE 6.1

$H(\mu m)$	$R_p(k\Omega)$	G (mmhos)	C_T (pF)	kH	f_r (MHz)	K^2
15	80.0	0.0125	10.35	0.96	47.7	0.014×10^{-2}
20	2.0	0.5	10.8	1.25	44.1	0.875
60	0.545	2.74	11.2	3.71	28.6	7.15

Where $G = 1/R_p$, f_r is the "resonant" frequency, $kH = 2\pi H/\lambda$ at "resonance", and K is the "electromechanical coupling constant" determined from equation (5.7) in section 5.5.4,

$$G(\omega_r) = (4/\pi)K^2(\omega_r C_T N) \quad , \qquad (5.7)$$

remembering that N = 15 for this structure. The value of the total transducer capacitance, C_T, is determined from the "CAPAX" program.

The values of K^2 calculated from the above theoretical values compare qualitatively with the values of $\Delta v/v$ calculated by Solie for ZnO on YZ sapphire**; however, they indicate that a $ZnO - Al_2O_3$ structure with the c-axis

---

* Figs. 5.7-5.9 are found on pages 100, 101 and 103, respectively.
** See Fig. 3 of ref. 60, or Fig. III.20, pp. 78 of ref. 61.

of the sapphire normal to the interface will have higher coupling to surface waves, by perhaps a factor of 2, than that analyzed by Solie, which has the c-axis parallel to the interface.

6.4 Material Constants of ZnO

In Chapter V, sections 5.5.1 - 5.5.3, it was observed that the measured values of the transducer admittance characteristics for ZnO - SiO_2 structures could only be obtained theoretically if some form of "reduction" was applied to the piezoelectric constants of the ZnO layer. There have been, however, different values of these constants reported in the literature, and one may wonder if perhaps the experimentally determined values of R_p and C_p can be derived theoretically by using other published values of the piezoelectric constants for ZnO, without having to reduce them.

Whenever we have been required to perform calculations involving ZnO, we have used the material constants given by (5.4) and published by Jaffe and Berlincourt[34]. In 1968, Crisler et al.[16] measured the material constants and found them to be considerably different from those of Jaffe and Berlincourt. More recently, Smith[57] has measured these constants and his findings are more in line with those of Jaffe and Berlincourt. Experimental measurements of the change in surface wave velocity when the free surface of ZnO is shorted by a metallic film indicate that the values of Smith may be the correct ones, and not those of Jaffe and Berlincourt[53]. The values determined by Smith are:

$$\begin{aligned} c_{11} &= 2.096 \times 10^{11}\ N/m^2 & e_{15} &= -0.48\ C/m^2 \\ c_{33} &= 2.106 & e_{31} &= -0.573 \\ c_{55} &= 0.425 & e_{33} &= 1.321 \\ c_{13} &= 1.046 & \rho &= 5665\ kg/m^3 \end{aligned} \tag{6.2}$$

$$\varepsilon_1 = 7.57\ ,\ \varepsilon_3 = 9.03 \qquad ;$$

and can be compared to those of Jaffe and Berlincourt:

$$
\begin{array}{ll}
c_{11} = 2.097 \times 10^{11}\ \mathrm{N/m^2} & e_{15} = -0.59\ \mathrm{C/m^2} \\
c_{33} = 2.109 & e_{31} = -0.61 \\
c_{44} = 0.425 & e_{33} = 1.14 \\
c_{13} = 1.051 & \rho = 5676\ \mathrm{kg/m^3}
\end{array}
\qquad (5.4)
$$

$$
\epsilon_1 = 8.33\ ,\ \epsilon_3 = 8.84\ .
$$

It is obvious that there is negligible difference between the elastic constants and the density, and only a minor change in the "isotropic dielectric constant", $\sqrt{\epsilon_1 \epsilon_3}$. There appears to be, however, a considerable difference in the piezoelectric constants. To observe the effect of these differences, two sets of computations were performed, the results of which are shown in Figs. 6.6 and 6.7. In Fig. 6.6, the admittance characteristics of an ID transducer on the free surface of ZnO are calculated, using both sets of constants. The transducer dimensions were:

$$
\begin{array}{l}
L = 101.6\ \mu m\ (\lambda_r = 203.2\ \mu m) \\
d = 50.8\ \mu m \\
W_o = 3.5\ mm\ ,
\end{array}
$$

and consisted of 15 finger pairs. It was assumed that R_s, for this transducer, was equal to 10 ohms. A portion of the curve shown in Fig. 6.6, and calculated using the Jaffe and Berlincourt data, was shown in Fig. 5.3a* and used for comparison with the measured data for free surface ZnO in section 5.4. As one would expect, from the negligible differences in the two sets of elastic constants and densities, the "resonant" frequencies are identical. More interesting is the difference in the two values of R_p at "resonance". The value of R_p calculated from the Smith data is higher than that calculated from the data of Jaffe and Berlincourt by about 30%, indicating reduced

---

* Fig. 5.3a is found on page 88.

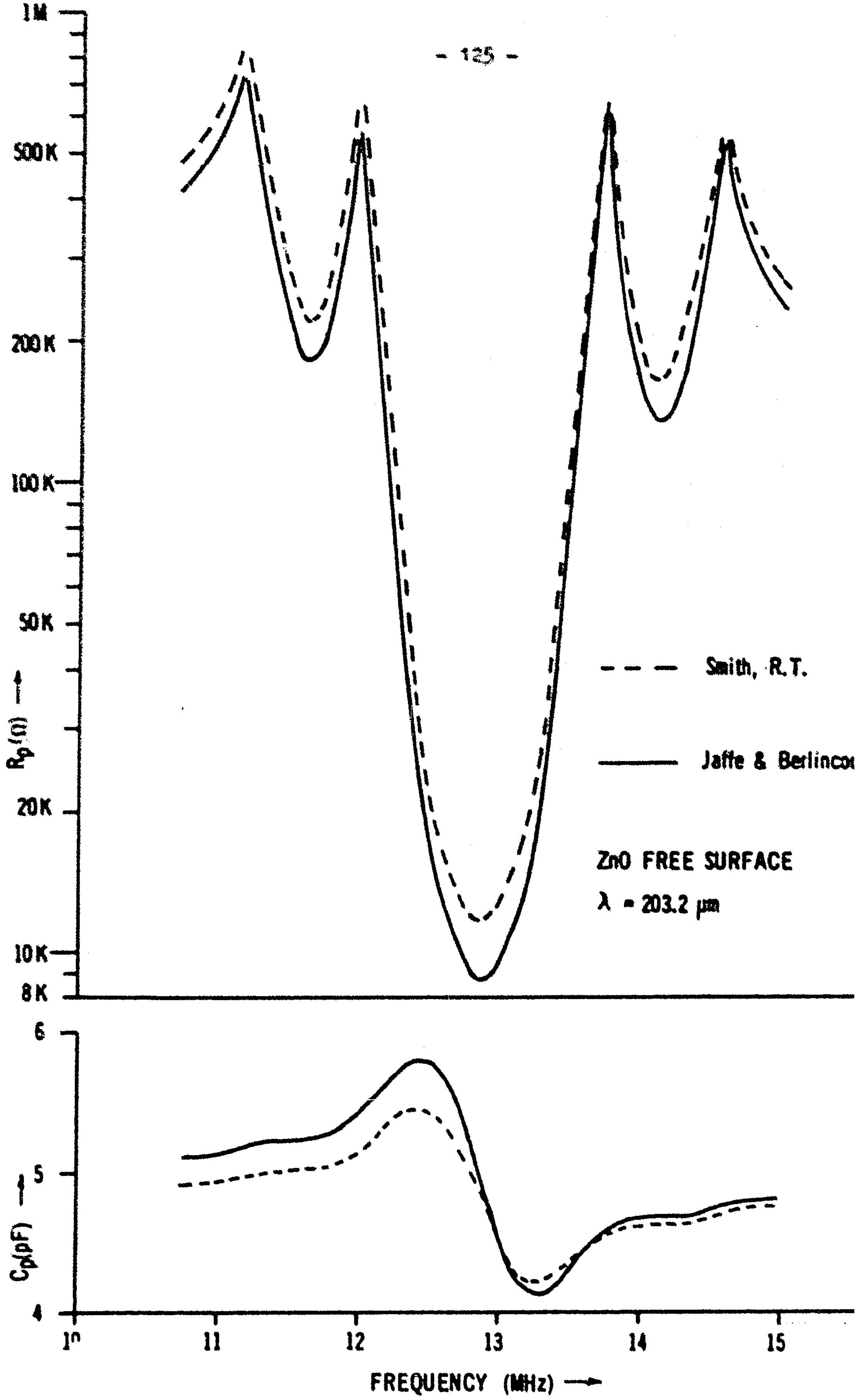

Figure 6.6 – Comparison of R_p and C_p calculated from data by Smith, R.T. and Jaffe & Berli

surface wave excitation. This would indicate that the piezoelectric constants e_{15} and e_{31} play a greater role in the generation of surface waves than e_{33}, for this configuration.

Figure 6.7 shows an equivalent set of curves calculated for a layered structure of ZnO and SiO_2 identical to the sample ZMU-50C, which was discussed in section 5.5.1. The transducer dimensions are :

$$L = 19.5\ \mu m\ (\lambda_r = 39\ \mu m)$$
$$d = 9.75\ \mu m$$
$$W_o = 1.5\ mm \quad ,$$

and consists of 20 finger pairs. It was assumed that the transducer had an R_s of 10 ohms. The curve calculated using the Jaffe and Berlincourt data is shown as the "single crystal" curve in Fig. 5.7.* Once again, ther is no difference in the "resonant" frequency; although the R_p at resonance, as determined by the Smith data, is greater than that calculated using the Jaffe and Berlincourt constants. In this structure, however, the differenc is only about 16%. Although the R_p calculated using the Smith constants is higher, it is not sufficient to explain the measured data for this sample, which is shown in Figs. 5.4* and 5.7* of section 5.5.1. Thus, one must still consider some form of "reduction" of the piezoelectric elements of ZnO to explain the measured results for the ZnO - SiO_2 structures examined in the previous chapter.

6.5 Summary

In this chapter we have shown how the characteristic wave behaviour within the transducer region can be explained on the basis of a "two surface wave" model. The theoretical analysis of Chapter II allowed us to

---

* Fig. 5.4 will be found on page 93, and Fig. 5.7 on page 100.

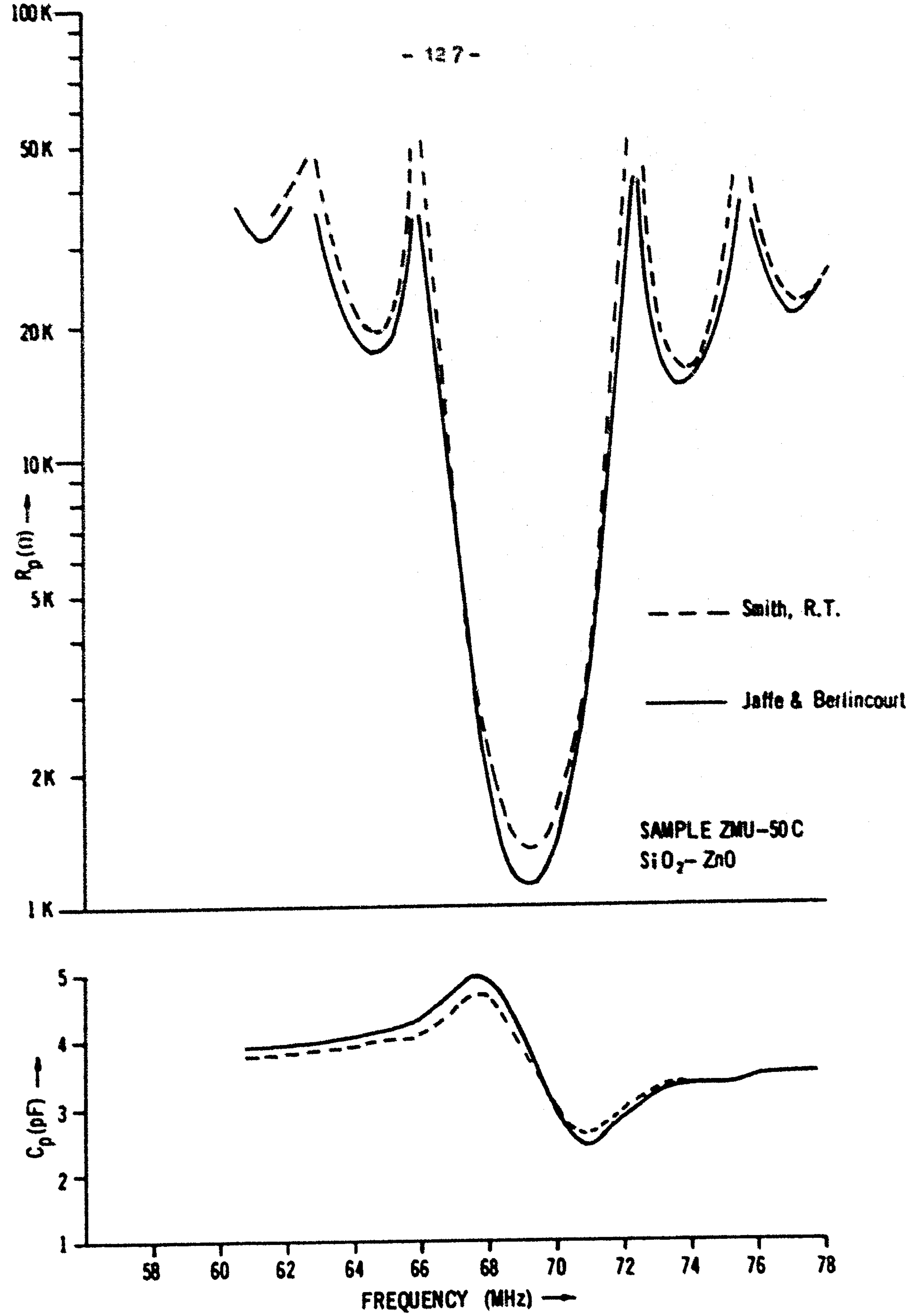

Figure 6.7 – Comparison of R_p and C_p calculated from data by Smith, R.T. and Jaffe & Berlincourt

separate the wave solutions within the ID transducer into two "wave packets", each representing a surface wave with propagation constant $|k_s|$, and propagating in opposite directions. These two waves start at opposite ends of the transducer and propagate through it to the other end, from which they are radiated into the surrounding media. As the waves propagate through the transducer, their amplitude changes by an amount determined by the relative phasing of the surface wave and the applied signal at every point. This fact is used as the basis for a simple mathematical model of an ID transducer which is presented in the following chapter.

We have also demonstrated the effect of dispersion on the R_p characteristic of an ID transducer and considered the result of using different reported values of material constants for ZnO in both free surface and layer excitation.

CHAPTER VII

A SIMPLE TRANSDUCER MODEL

7.1 Introduction

The preceding chapter used the results of the general theory to demonstrate how surface acoustic waves develop as they propagate under the transducer fingers and the resulting standing wave behaviour. This chapter discusses a very simple mathematical model of an ID transducer, as a generator of surface waves, which does not require specific reference to the wave equations of Chapter II. This model can predict the "amplitude factors" presented in Chapter VI, and which are responsible for the observed standing wave behaviour, to within a multiplicative constant. It can also be used to accurately predict the admittance results of Chapter V and Chapter VI, except for a constant scale factor which must be determined from either experimentation or the general theory. As will be seen, this model contains the essence of the "Stanford" model[58] which is in common use.

Since we are interested in the derivation of a plausible model, and not a rigorous description, the approach to be taken will, at times, be approximate and without excessive concern for physical or mathematical rigor. For simplicity, the arguments will be based on the assumption that the transducer is located on the free surface of a material, however, some of the data used for comparison will be taken from layered structures.

7.2 A Simple Mathematical Model of an ID Transducer

We shall begin by considering an ID transducer as a one dimensional structure oriented along the direction of wave propagation, without concern for possible variations in other directions. Assume that an ID transducer can then be described by a generating function $g(x)$ which acts upon propagating surface waves such that the change in amplitude of the wave, over the interval 'dx', is given by $g(x)dx$. (A time dependence $e^{-i\omega t}$ will be assumed.) Thus, if the wave has a propagation constant $k > 0$*, the change in amplitude, as observed at the point $x' > x$, resulting from the generating function acting at x is

$$dA^{+} = g(x)e^{ik(x'-x)}dx \qquad . \qquad (7.1)$$

Where the '+' sign used as a superscript implies the wave propagating in the positive direction. Hence, the total change in amplitude over the interval $x_o \leq x \leq x'$, as observed at x', is given by

$$A^{+} = \int_{x_o}^{x'} g(x)e^{ik(x'-x)}dx \qquad , \qquad (7.2)$$

which will be recognized as the convolution of the generating function with a propagating wave. Thus, the amplitude of the wave propagating in the positive direction at x', $V_o^{+}(x')$, can be written

$$V_o^{+}(x') = V_o^{+}(x_o)e^{ik(x'-x_o)} + \int_{x_o}^{x'} g(x)e^{ik(x'-x)}dx \qquad . \qquad (7.3)$$

Physically speaking, the generating function $g(x)$ will be related to either the applied electric potential or field, and for the purposes of simplification we will make the following assumptions:

(1) finger spacing = L = constant

(2) finger overlap (aperture) = W_o = constant

---

* For $k < 0$, the analysis proceeds in a similar fashion.

(3) origin, $x = 0$, is located at the center of a finger, and the transducer extends from $-D/2$ to $D/2$.

Then one can write

$$g(x) = a_o \cos(\pi x/L), \quad |x| < D/2$$
$$g(x) = 0 \qquad\qquad , \quad |x| > D/2 \quad ,$$

as a reasonable first approximation to an appropriate generating function. Assuming that the wave $V_o^+(x')$ starts at $x = -D/2$, (i.e., $V_o^+(-D/2) = 0$) substitution of $g(x)$ into (7.3) gives

$$V_o^+(x') = -\frac{ia_o}{2}\left[\frac{e^{iK_1 D/2} - e^{-iK_1 x'}}{K_1} + \frac{e^{iK_2 D/2} - e^{-iK_2 x'}}{K_2}\right] e^{ikx'} \quad , \qquad (7.4)$$

where $K_1 = (k - \pi/L)$ and $K_2 = (k + \pi/L)$. The term within the brackets then represents the "amplitude factor" for the wave e^{ikx}.

Proceeding from (7.1) in the same manner, but for the surface wave propagating in the negative direction $(k < 0)$, one obtains

$$V_o^-(x) = -\frac{ia_o}{2}\left[\frac{e^{iK_1 D/2} - e^{iK_1 x}}{K_1} + \frac{e^{iK_2 D/2} - e^{iK_2 x}}{K_2}\right] e^{-ikx} \quad . \qquad (7.5)$$

It is obvious that the "amplitude factor" of (7.5) is the mirror image, about $x = 0$, of that in (7.4). Inspection of (7.4) shows that the magnitude of the "amplitude factor" for the wave $e^{ikx'}$ at $x' = D/2$ (i.e., the magnitude of the wave radiated from the ID transducer) is proportional to

$$a_o\left[\frac{\sin(k - \pi/L)D/2}{(k - \pi/L)} + \frac{\sin(k + \pi/L)D/2}{(k + \pi/L)}\right] \quad . \qquad (7.6)$$

The term within the brackets is recognized as the expression $F_n(k)$, for $n = 1$, used in Chapter II.

Figures 7.1a and 7.1b compare the magnitude of the "amplitude factor" of the wave $V_o^*(x')$, defined by (7.4), with that derived by the more general theory, respectively. Figure 7.1b was previously introduced as Fig. 6.2, and the same finger spacing and number of finger pairs were used in the determination of the curves presented in Fig. 7.1a. As can be seen, the behaviour of the simple model and the more general approach are very similar with regard to the amplitude factor. The differences are a multiplicative constant, which is the same for all of the curves shown in the Figs. 7.1a and 7.1b, and the absence of the forced particle displacements in the simple model. The latter is evidenced by the fact that the amplitude factor, as defined by (7.4), has 'zeroes' within the transducer region, whereas the amplitude factor calculated from the general theory never completely vanishes*. Thus, it would appear evident that the one dimensional model defined by (7.2), with the generating function $g(x)$, provides an adequate description of the generation and propagation of acoustic surface waves along the x-axis within the transducer. It is obvious that the amplitude factors of (7.4) and (7.5), combined with the appropriate propagating wave, will create standing wave patterns that are identical to those shown in Fig. 6.1 of the preceding chapter, and are derived from the general theory.

Thus far we have concentrated on the surface wave behaviour along

---

* The amplitude factors calculated from the general theory, and shown in Fig. 7.1b, vanish at $x = -D/2$ only as the result of our inability to completely evaluate the solutions at that point.

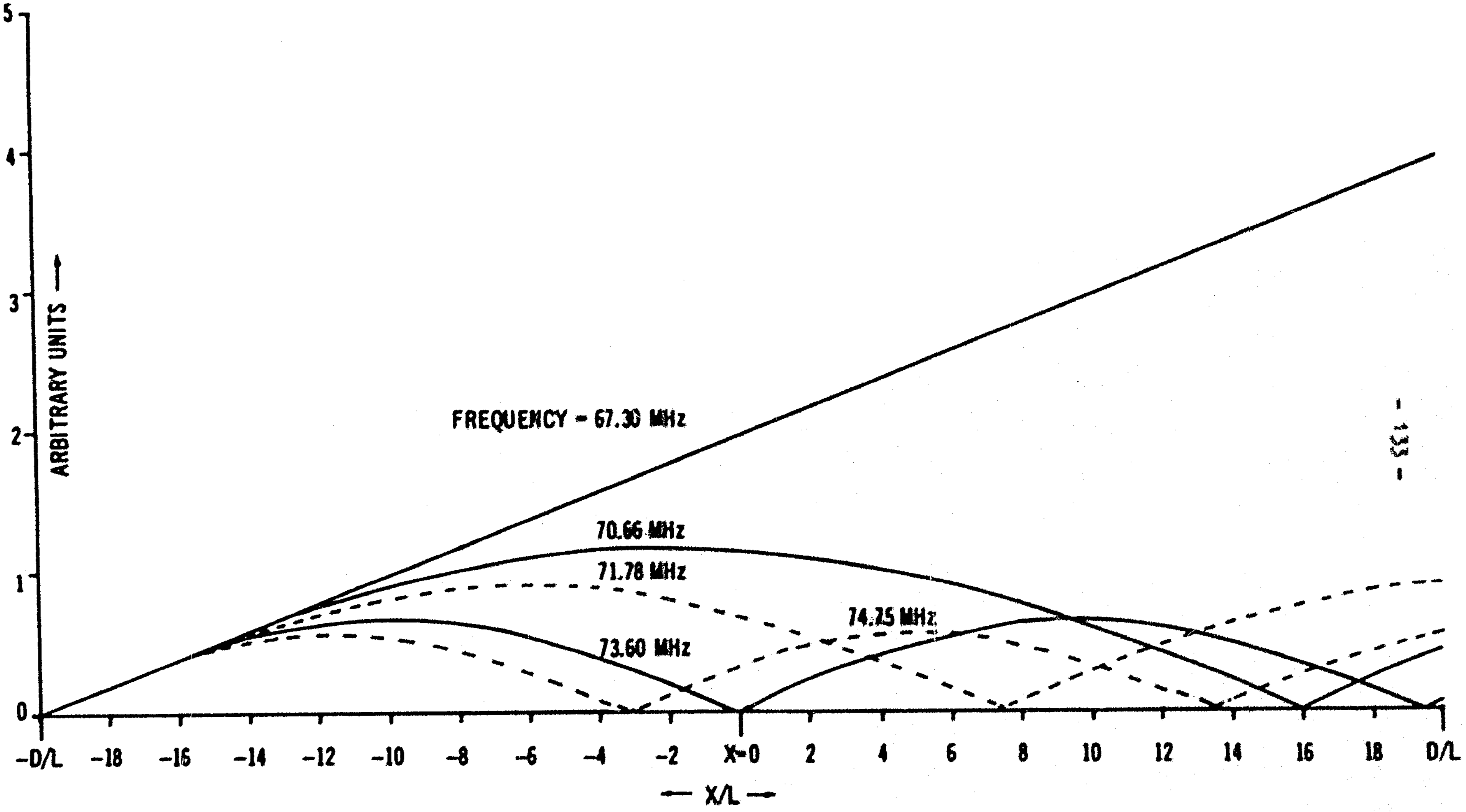

Figure 7.1(a) – Magnitude of "Amplitude Factor" determined by 'Simple Model' from –D/2 to D/2 for a 20-finger pair transducer.

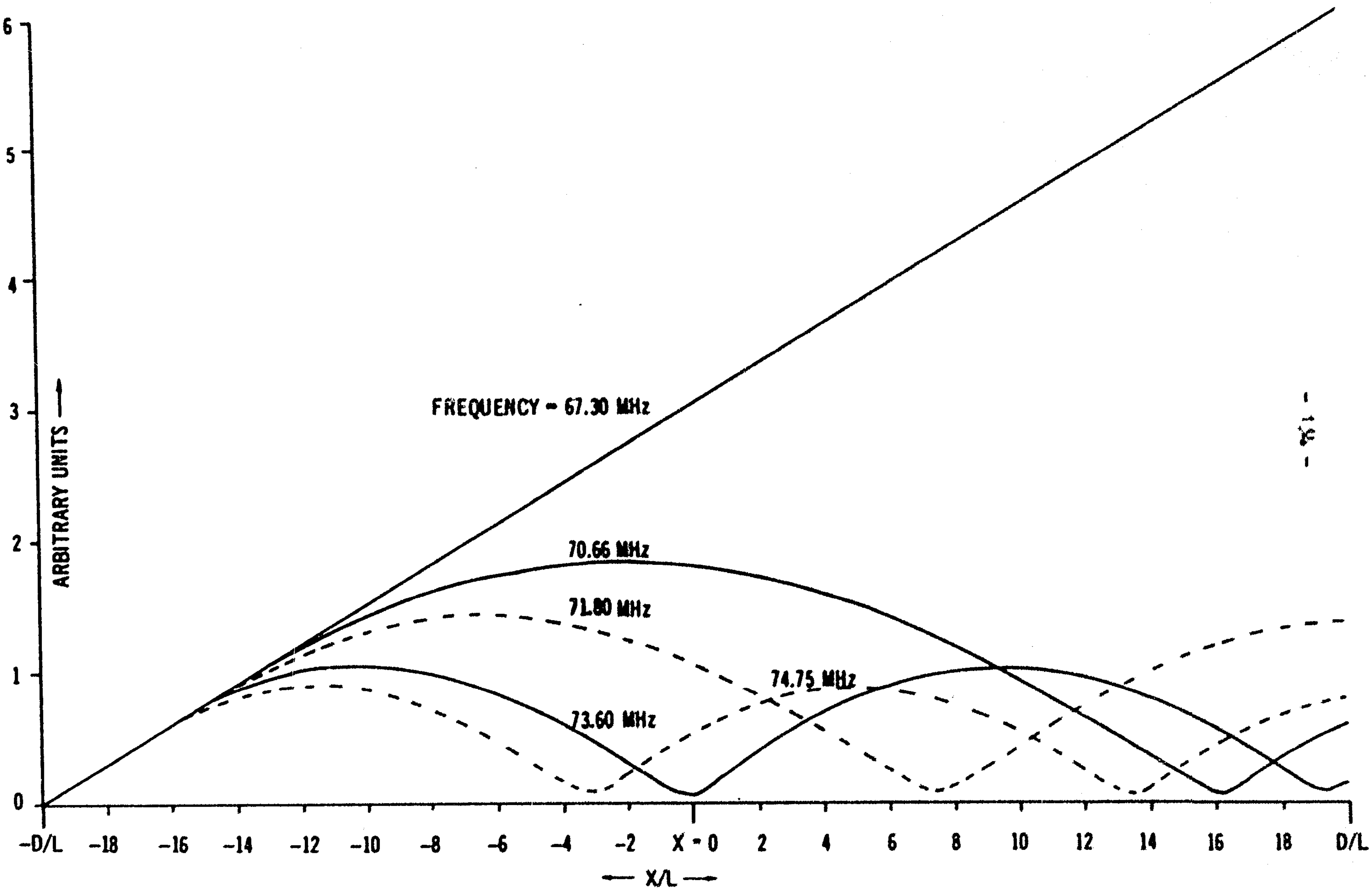

Figure 7.1(b) – $|AF_3^+|$ Determined from general theory

the direction of propagation; however, it is well known that the surface wave characteristics are also a function depth in the material. Hence, one can consider the result (7.4) as a description of the amplitude of the surface wave propagating in the positive direction at a particular $z = z_o$. For convenience, it will henceforth be assumed that $z_o = 0$. To complete the description of surface wave behaviour with our simple model, it is necessary to consider the z-dependence. It has been shown by many authors,[1,23,36,50] in addition to the theory of Chapter II, that surface waves decay with depth into the material in a manner described by the sums of exponentials, and that the decay constants are proportional to the wave number k. Thus, it will be convenient to write, as an approximation of the surface wave $V^{+}(x,z)$ within the ID transducer ,

$$V^{+}(x,z) = V_o^{+}(x) \sum_{N'}^{N} e^{-\beta_n k|z|} \quad , \qquad (7.7)$$

where the β_n are constants and $V_o^{+}(x)$ is given by (7.4). The range of the index 'n' is determined by the number of terms necessary to fully describe a surface wave in the region under consideration.

7.2.1 Admittance Calculations

The preceding section used a convolution approach to determine the x-dependence of an acoustic surface wave within the transducer, and the z-dependence was added in a somewhat arbitrary fashion. We will now demonstrate that the expression (7.7) is an adequate description of acoustic surface waves from the standpoint of the transducer admittance. Using (7.6) and (7.7), the surface wave leaving the transducer in the positive x-direction can be written

$$V^*(x,z) = a_o\left[\frac{\sin K_1 D/2}{K_1} + \frac{\sin K_2 D/2}{K_2}\right]\sum_{n}^{N} e^{-\beta_n k|z|}\, e^{ik(x-D/2)} \quad , \qquad (7.8)$$

where $K_1 = (k - \pi/L)$ and $K_2 = (k + \pi/L)$. In Chapter III, section 3.2, it was shown that the power in the radiated wave is given by

$$P = -\tfrac{1}{2}\,\text{Real}\left[\int_A (T^*_{ij}\frac{\partial U_j}{\partial t}) n_i\, dA\right] \quad , \qquad (3.6)$$

where A is the area through which the surface wave propagates. Because of the symmetry restrictions previously introduced, equation (3.6) can be written

$$P = -2\,W_o \int_{-\infty}^{H} \left(T^*_j \frac{\partial U_j}{\partial t}\right) dz \quad ,$$

from equation (4.5). The term W_o is the overlap, or aperture, of the transducer and H is the thickness of the layer. The term T^*_j will introduce mixed derivatives with respect to x and z with the appropriate elastic constants. However, in all cases, the wave number k is a common factor. Thus, substituting the expression (7.8) into the above, one can write

$$P \propto \omega k\, a_o^2\left[\frac{\sin K_1 D/2}{K_1} + \frac{\sin K_2 D/2}{K_2}\right]\int_{-\infty}^{H}\sum_{n}^{N}\sum_{m}^{N} e^{-(\beta_n + \beta^*_m)k|z|}\, dz \qquad (7.9)$$

as an approximate expression for the radiated power, where the symbol "$\propto$" implies proportionality. The terms β^*_m appear as coefficients upon the evaluation of T^*_j and have been absorbed in the proportionality, along with the appropriate elastic constants. The total radiated power is determined by integrating over the z-axis and can be approximated

$$P \propto \omega\, a_o^2\left[\frac{\sin K_1 D/2}{K_1} + \frac{\sin K_2 D/2}{K_2}\right]^2 \quad , \qquad (7.10a)$$

when the constants $(\beta_n \cdot \beta_m^*)$ have been absorbed in the proportionality. Since $\omega = kv$, where v is the wave velocity, the equation (7.10a) can be expressed

$$P \propto k\, a_o^2 \left[\frac{\sin K_1 D/2}{K_1} + \frac{\sin K_2 D/2}{K_2} \right]^2 \quad , \qquad (7.10b)$$

assuming that the change in velocity with k is small. The total input power is proportional to the transducer admittance and thus the transducer conductance, $G(k)$, can be expressed as*

$$G(k) \propto k\, a_o^2\, (D/2)^2 \left[\frac{\sin K_1 D/2}{(K_1 D/2)} + \frac{\sin K_2 D/2}{(K_2 D/2)} \right]^2 . \qquad (7.11a)$$

The relation (7.11a) is similar to that used by Smith et al.[58], who predict that

$$G(k) \propto \left(\frac{\sin y}{y} \right)^2 \quad , \qquad (7.11b)$$

where $y = M(k - k_r)/k_r$. The term k_r represents the value of k at resonance and M is the number of finger pairs. The original relationship used by Smith et al.[58] for the transducer admittance was derived as a function of frequency; however, if the system under study is dispersive, the wave number k is a more appropriate variable. The imaginary part of the transducer admittance, $B(k)$, can be determined from the Hilbert transform of the conductance[48]. Thus, if the conductance is given by $G(k)$,

$$B(k) = -1/\pi \int_{-\infty}^{\infty} \frac{G(\eta)}{(k-\eta)}\, d\eta \quad . \qquad (7.12)$$

Substituting the expression (7.11a) for $G(k)$, and integrating, gives

---

* The equation (7.11a) is essentially identical to equation (42) of Joshi and White, ref. 36.

$$B(k) = k\, a_o^2 (D/2)^2 \left\{ \left[\frac{\sin 2K_1' - 2\delta K_1}{2K_1'^2} \right] + \left[\frac{\sin 2K_2' + 2\delta K_2'}{2K_2'^2} \right] - \frac{\sin kD}{K_1' K_2'} \right\} \quad ; \qquad (7.13a)$$

where $K_1' = K_1 D/2$, $K_2' = K_2 D/2$ and $\delta = \pi/Lk$. Again, this result is similar to that of Smith et al.[58], given by

$$B(k) = \left(\frac{\sin 2y - 2y}{2y^2} \right) \quad . \qquad (7.13b)$$

The last term which appears in (7.13a) results from the cross-product in the expression

$$\left[\frac{\sin K_1 D/2}{K_1} + \frac{\sin K_2 D/2}{K_2} \right]^2 \quad ,$$

and has negligible contribution to the equation (7.13a). In the limit, as $|k| \to \pi/L$, this term has the value L/π.

Figures 7.2a and 7.2b compare the transducer conductance and susceptance, respectively, as determined by the Stanford model and given by equations (7.11b) and (7.13b), with that calculated by the 'simple model' discussed in this chapter and given by (7.11a) and (7.13a). These results are also compared with theoretical calculations on a layered structure*, using the general theory of Chapters II and III. The transducer used for all of the calculations had 20 finger pairs and, in the calculations from the general theory, it was assumed that the transducer had no series resistance. The curves calculated from the two 'models' have been normalised to the peak value of the conductance determined from general theory. The susceptance of the static capacitance of the transducer has been subtracted

---

* The structure which was simulated for this comparison was the sample ZMU-50C, provided by M. Holland, using single crystal constants for the ZnO. The change in velocity from the lowest to the highest value of k shown is on the order of 1%.

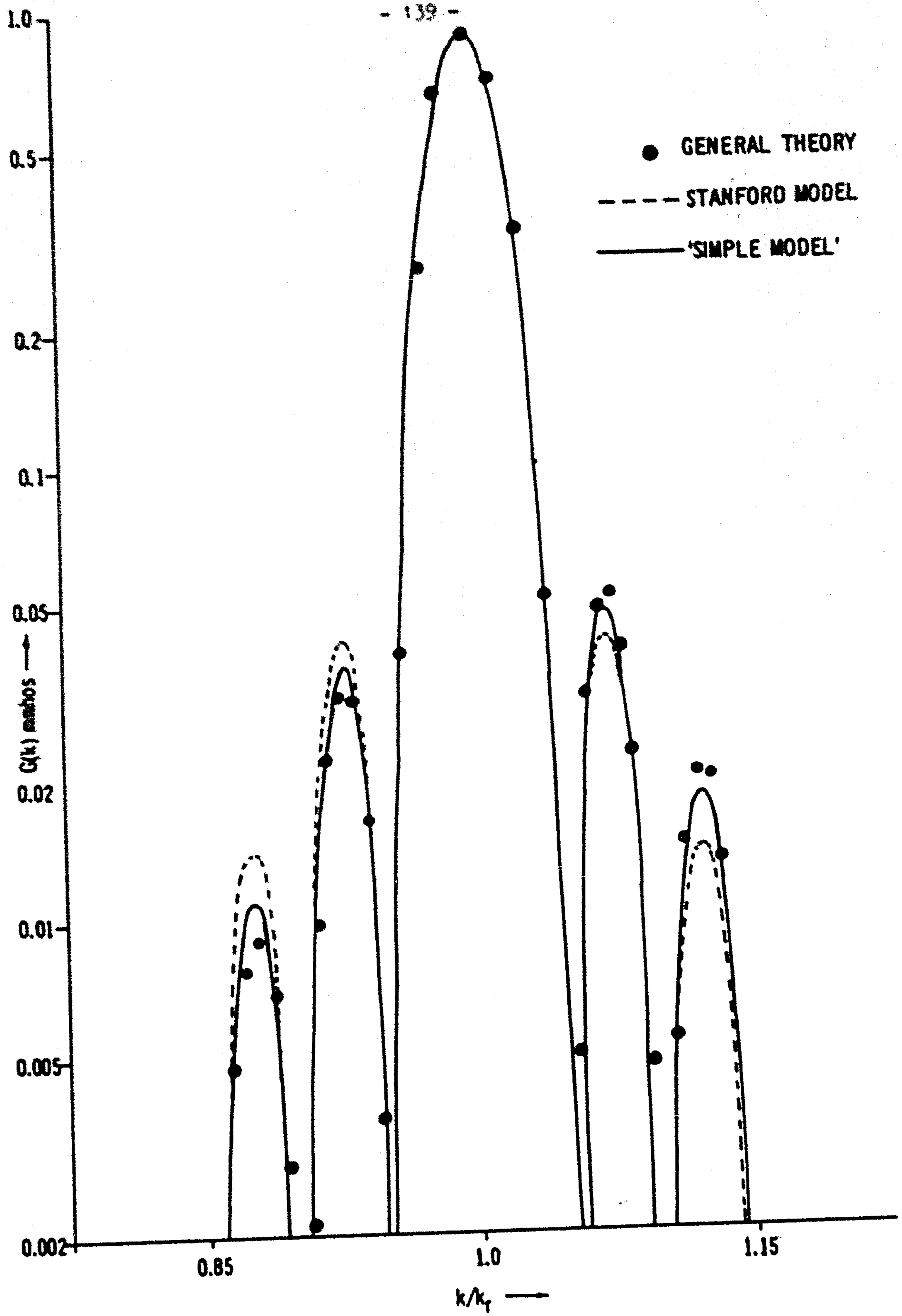

Figure 7.2(a) – Comparison of G(k) calculated by Stanford Model and 'Simple Model' with general theory

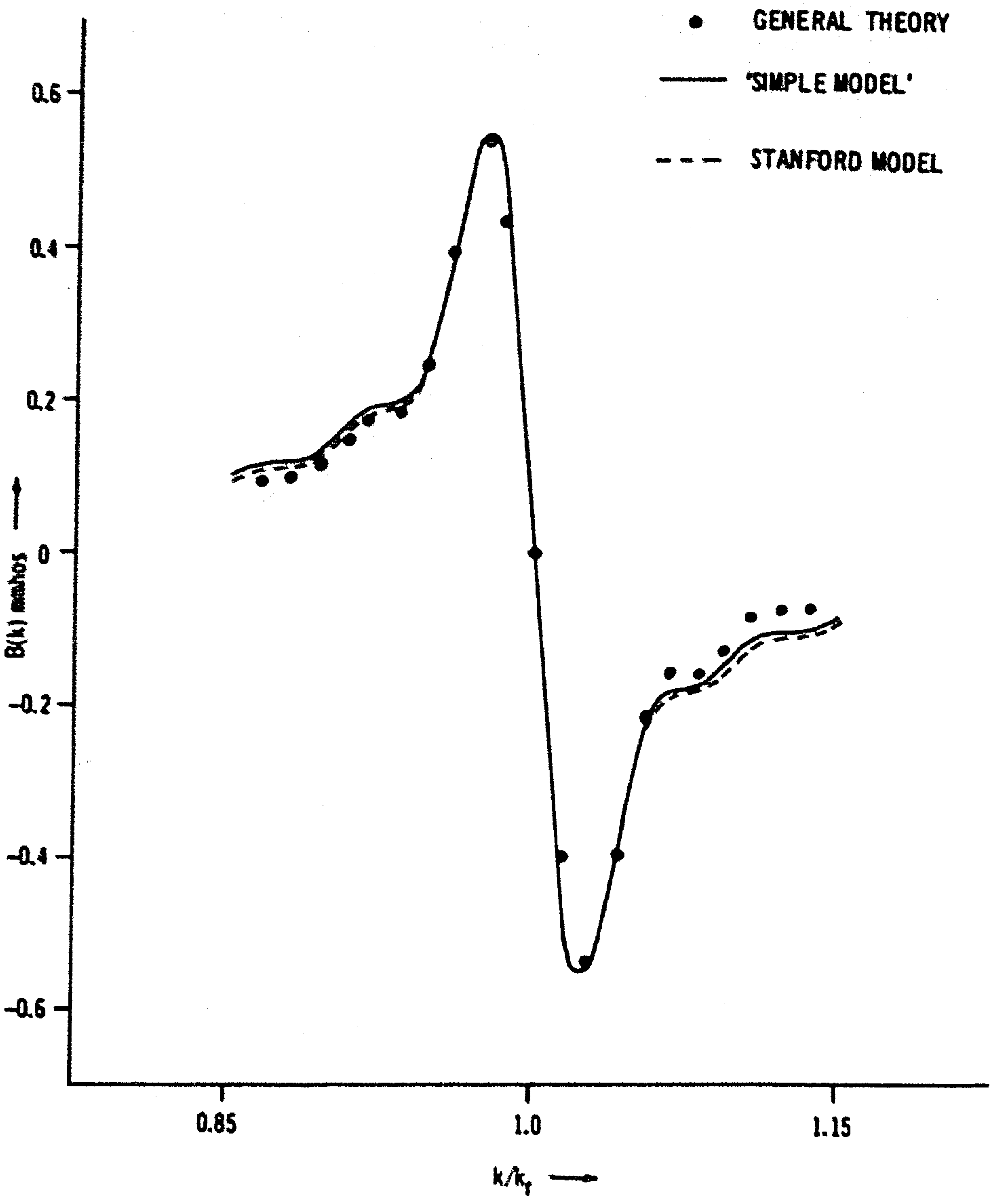

Figure 7.2(b) – Comparison of B(k) calculated by Stanford Model and 'Simple Model' with general theory

from the results determined by the general theory, and shown in Fig. 7.2b. As can be seen, in Fig. 7.2a, both the 'simple model' and that of Smith et al.[58] are in good agreement with each other, and the results of the general theory, in the region of the central lobe. The only apparent variation is in the region of the side lobes, where our 'simple model' is a slightly better fit to the theoretical results than the Stanford model. As seen in Fig. 7.2b, there is very little variation between either of the 'models' and the theoretical results in the central region, it is only at the extremities where any variation occurs. The comparisons between the general theoretical results and measurements, shown in Chapter V, tend to support the general theory; thus, the differences between the two 'models' and the theoretical results which appear in Figs. 7.2a and 7.2b may result from failures in the 'models', and not the general theory.

7.2.2 Further Discussion of the 'Simple Model'

One can see that the simple mathematical model for an ID transducer which has been proposed in this chapter will behave in essentially the same fashion as the Stanford model, when describing the transducer admittance, but in addition it can readily describe the behaviour of the surface waves within the transducer. Further consideration shows that the relative correspondance between the two models is to be expected. The approach used by Smith et al.[58] is to represent each finger pair of the ID transducer by a discrete "equivalent circuit", and the cascaded results gives the transducer admittance characteristics. The "equivalent circuit" approach was originally derived for bulk wave devices, and relates the outputs at the acoustic "terminals" (force and velocity) to the inputs at the electrical terminals (voltage and current)[6]. The elements within the equivalent circuit are expressed as frequency dependent electrical impedances. While this approach facilitates the rapid calculation of the device admittance (impedance), it is not a very satisfactory approach for presenting surface wave behaviour. The simple mathematical model which has been discussed in this chapter is, however, capable of describing both the surface wave behaviour and the transducer admittance characteristics. The convolution of the "generating function", $g(x)$, with a travelling wave, expressed by equation (7.2), is the equivalent of cascading the discrete sections in the approach of Smith et al.[58]. The equivalence between the two approaches results in both methods producing similar predictions of transducer characteristics. The main difference is that the model discussed in this chapter is derived on the basis of a continuous function, whereas the functional representation used by Smith et al.[58] is discrete.

One may argue that the "equivalent circuit" approach can relate the transducer admittance directly to the "electro-mechanical coupling factor", a measurable or calculable parameter of the material. However, inspection shows that a single measurement on the device in question is still required to define the "filling factor" for the ID transducer so that the relationship can be completed. Our "simple model" also requires a single measurement, or calculation, to provide the absolute scale factor for the transducer admittance. The measurement, or calculation, usually performed will determine the transducer conductance at "resonance". Neither model is capable of providing a measure of the static capacitance of the device.

7.3 Extension to Other Transducer Types

One can visualize how this 'simple model' could be used to describe the behaviour of a transducer in which the finger overlap (aperture) and spacing vary along the length of the transducer. Returning to equation (7.1), one has

$$dA^{+}(x') = g(x)e^{ik(x'-x)}dx \quad , \qquad (7.1)$$

for the wave propagating in the positive direction. If the finger overlap varies, $g(x)$ can be written

$$g(x) = a_o W(x)\cos \pi x/L, \quad |x| < D/2$$
$$g(x) = 0 \qquad , \quad |x| > D/2 \quad ,$$

where $W(x)$ is the "overlap" or weighting function. Substituting into (7.3) one has

$$V_o^{+}(D/2) = \frac{a_o e^{ikD/2}}{2}\left\{ \int_{-D/2}^{D/2} W(x)e^{-iK_1 x}dx + \int_{-D/2}^{D/2} W(x)e^{-iK_2 x}dx \right\} \; ; \quad (7.14)$$

where $K_1 = (k-\pi/L)$ and $K_2 = (k+\pi/L)$, as before. The integrals which appear in (7.14) are, of course, the Fourier transforms of the function $W(x)$ with respect to the variables K_1 and K_2 , thus illustrating the well known fact that the frequency response of an ID transducer is proportional to the Fourier transform of its "overlap function"[28,35,65].

If the spacing between the fingers, L, also varies, equation (7.2) can be written

$$A^{+} = a_o \int_{x_o}^{x'} W(x)f(L(x))e^{ik(x'-x)}dx \quad , \qquad (7.15)$$

where $f(L(x))$ represents the x-dependence of the "generating function". The ease with which (7.15) can be solved will, of course, depend on the functional representations for $W(x)$ and $f(L(x))$. In very involved cases, it may be preferable to segment the transducer into regions in which either $W(x)$ or $L(x)$ is approximately constant, and then sum the resulting integrals. The method of including second order effects, such as internal reflections and mass loading of the fingers is not so obvious, however, and it may be in this aspect that the "equivalent circuit" approach of Smith et al.[58] is superior.

7.4 The 'End Correction' for an ID Transducer

In Chapter II, section 2.1.4, and in section 7.1 of this chapter, the 'potential' function of the ID transducer was defined so as to terminate abruptly at $x = \pm D/2$. It was observed, in section 2.1.4, that the potential function could be extended into the region outside the transducer in a continuous fashion, but that such an extension would not appreciably alter the results for a transducer of "reasonable length". In this section the 'simple model' will be used to examine this statement.

First it is necessary to decide on an extension of the potential function at the ends of the transducer. It is obvious that the potential function must decay asymptotically to zero outside the transducer, and it is unlikely that there will be any measurable potential at a distance greater than L from $\pm D/2$. It is also necessary that the amplitude and first derivative of the extension match the potential inside the transducer at $x = \pm D/2$. A simple function which fulfills these requirements, and is compatible with $g(x) = \cos(\pi x/L)$, is

$$g_1(x) = a_o \cos M\pi \cos^2(\pi x/L), \quad D/2 \leq |x| \leq D/2 + L \quad .$$

The term M represents the number of finger pairs ($D/2 = ML$), and the coefficient $\cos(M\pi)$ is necessary for the continuity of both amplitude and derivative with $\cos(\pi x/L)$ at $x = \pm D/2$. The transducer can then be divided into three regions:

$$g(x) = g_1(x) = a_o \cos M\pi \cos^2(\pi x/L), \quad -(D/2+L) \le x \le -D/2$$

$$g(x) = g_o(x) = a_o \cos(\pi x/L) \quad , \quad -D/2 \le x \le D/2$$

$$g(x) = g_1(x) = a_o \cos M\pi \cos^2(\pi x/L), \quad D/2 \le x \le D/2+L\ .$$

From equation (7.3), the wave leaving the transducer at $x = D/2+L$, $V_o^+(D/2+L)$, assuming $V_o^+(-D/2-L) = 0$, can be written

$$V_o^+(D/2+L) = V_o^+(D/2)e^{ikL} + \int_{D/2}^{D/2+L} g_1(x)e^{ik[(D/2+L)-x]}dx \quad , \qquad (7.16)$$

where

$$V_o^+(D/2) = V_o^+(-D/2)e^{ikD} + \int_{-D/2}^{D/2} g_o(x)e^{ik(D-x)}dx$$

and

$$V_o^+(-D/2) = \int_{-D/2-L}^{-D/2} g_1(x)e^{ik(-D/2-x)}dx \quad .$$

Evaluation of (7.16) yields

$$V_o^+(D/2+L) = a_o e^{ik(D/2+L)}\left\{\left[\frac{\sin K_1 D/2}{K_1} + \frac{\sin K_2 D/2}{K_2}\right] + \Delta\right\}, \qquad (7.17)$$

where the "end correction", Δ, is given by

$$\Delta = \cos M\pi\left\{\frac{\sin k\,(D/2+L) - \sin k\,D/2}{k} + \frac{1}{2}\left[\frac{\sin K_3(D/2+L) - \sin K_3 D/2}{K_3} + \frac{\sin K_4(D/2+L) - \sin K_4 D/2}{K_4}\right]\right\} .$$

The terms K_1, K_2, K_3, and K_4 are defined by:

$$K_1 = (k - \pi/L)$$

$$K_2 = (k + \pi/L)$$

$$K_3 = (k - 2\pi/L)$$

$$K_4 = (k + 2\pi/L) \quad .$$

Using the results of section 7.2.1, the radiation conductance for the transducer with the "end correction", $G(k)$, can be written

$$G(k) = k\left|V_o^*(D/2 + L)\right| \quad .$$

Substituting the result (7.17) into the above gives

$$G(k) = ka_o^2\left\{\left[\frac{\sin K_1 D/2}{K_1} + \frac{\sin K_2 D/2}{K_2}\right] + \Delta\right\}^2 \quad . \qquad (7.18a)$$

A reasonable measure of the effect of the "end correction" on the transducer behaviour would be to compare the radiation conductance calculated with the "end correction", using equation (7.18a), and the radiation conductance without the "end correction", $G'(k)$, which is given by

$$G'(k) = ka_o^2\left[\frac{\sin K_1 D/2}{K_1} + \frac{\sin K_2 D/2}{K_2}\right]^2 \quad . \qquad (7.18b)$$

Equation (7.18b) is obtained from (7.11a). Such a comparison is shown in the Figs. 7.3a - 7.3d, for values of $M = 1, 3, 5, 10$, respectively. The vertical scale is the same for all of the figures, and is in arbitrary units. The horizontal axis is in units of k/k_r, and all of the curves are centered about $k/k_r = 1$, however, the range of the horizontal axis varies. The term k_r equals π/L. As can be seen in Fig. 7.3a, the "end correction" will have a considerable effect on the transducer conductance for $M = 1$. This is to be

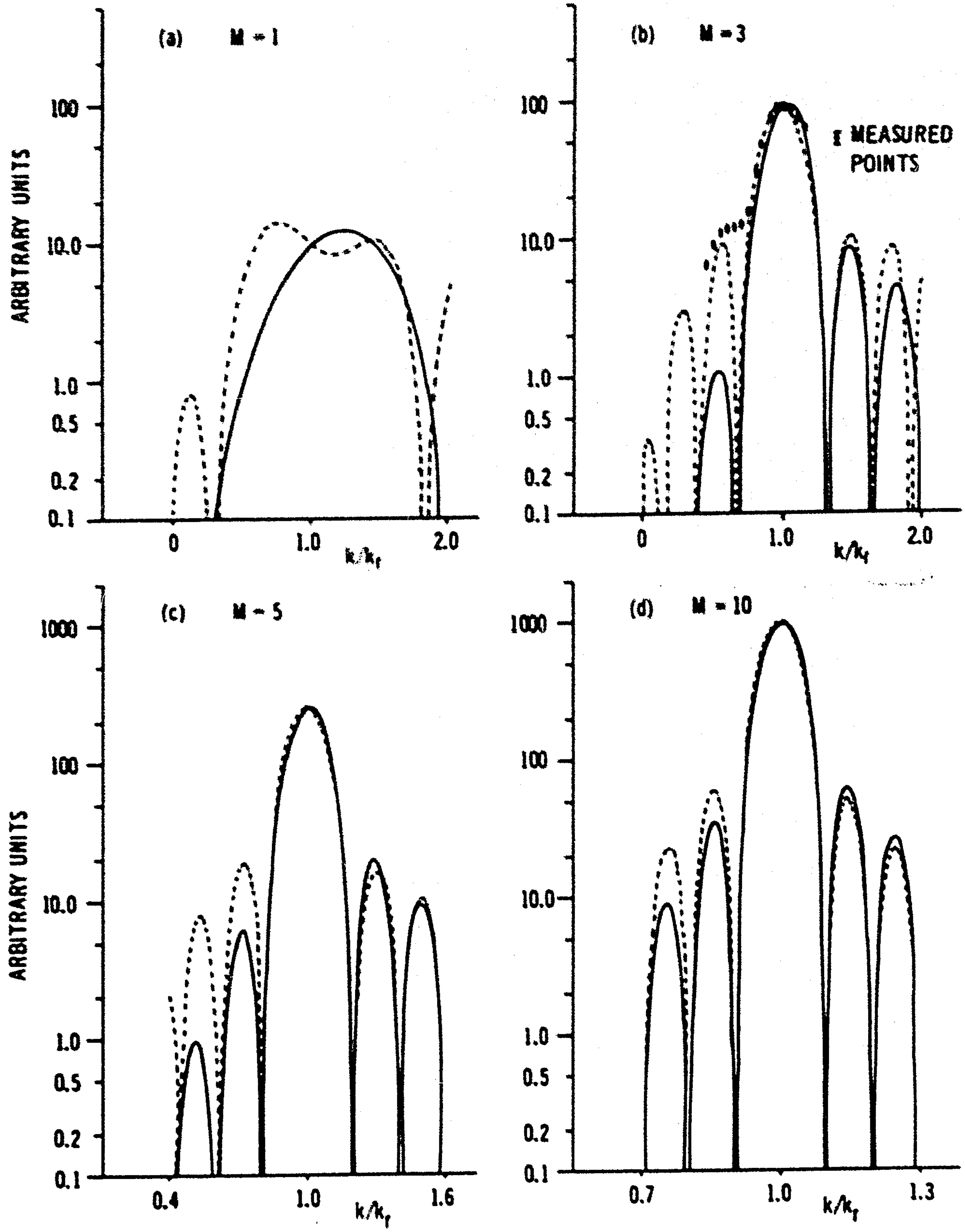

Figure 7.3 – Showing effect of 'End Correction'

– – – – With Correction ——— Without Correction expected since, in this case, the region occupied by the "end correction" is as large as the region between the fingers. Figure 7.3b shows that, for $M = 3$, the transducer conductance in the central lobe will be largely unaffected by the "end correction". Only in the side lobes will its effect be apparent. Figure 7.3b also contains experimental measurements of the conductance of a 3 finger pair ID transducer on $LiNbO_3$. The peak conductance of the transducer was normalized to the peak value of the curve calculated without the "end correction". The measurements were performed as described earlier in Chapter V, using the same $LiNbO_3$ sample that was used in section 5.3. As can be seen, the measurements are more in keeping with the transducer behaviour with the "end correction" than without it. The remaining two figures, 7.3c and 7.3d, show that the effect of the "end correction" in the central lobe rapidly diminishes as M increases, and for $M = 10$ it has essentially disappeared. A small, but noticable effect does, however, remain in the side lobes for $M = 10$. Hence, it would appear that, for a transducer whose length is greater than a few finger pairs, the effect of the "end correction" is small, and will appear only in the side lobe response.

It is interesting to observe that, with the exception of $M = 1$, the dominant effect of the "end correction" is to "level out" the side lobe response of the transducer, and this fact warrants further discussion. Let us return to equation (7.17),

$$V_o^+(D/2+L) = a_o e^{ik(D/2+L)} \left\{ \left[\frac{\sin K_1 D/2}{K_1} + \frac{\sin K_2 D/2}{K_2} \right] + \Delta \right\}, \quad (7.17)$$

where Δ is given by

$$\Delta = \cos M\pi \left\{ \frac{\sin k(D/2+L) - \sin k\, D/2}{k} + \frac{1}{2}\left[\frac{\sin K_3 (D/2+L) - \sin K_3 D/2}{K_3} + \frac{\sin K_4 (D/2+L) - \sin K_4 D/2}{K_4} \right] \right\} .$$

In the absence of the "end correction", Δ, (7.17) contains two "sin(x)/x" type terms involving K_1 and K_2, respectively, and can be written

$$V_o^+(D/2+L) = a_o e^{ik(D/2+L)} \left[\frac{\sin K_1 D/2}{K_1} + \frac{\sin K_1 D/2}{K_1} \right] . \quad (7.19)$$

Equation (7.19) is symmetric about the origin, $k = 0$, with maximum values of D/2 occurring at $k = \pi/L$ and $k = -\pi/L$. For transducers which are only a few finger pairs in length, it is evident that considerable "overlapping" of the two "sin(x)/x" terms in (7.19) can occur, which results in asymmetry about the points $k = \pi/L$ and $k = -\pi/L$. This is evident in Fig. 7.3b, for $M = 3$, and to some extent, in Fig. 7.3c, for $M = 5$. The side lobes of the conductance curve calculated without the "end correction" (solid curve) have greater asymmetry than can be accounted for by the multiplying factor 'k' which appears in equation (7.18b).

The inclusion of the "end correction", Δ, in (7.17) adds three additional terms which are also "sin(x)/x" in nature, but have variable periodicity. The first of these terms is centered about $k = 0$, and has a maximum value of L. The other two terms, involving K_3 and K_4, are centered about $k = 2\pi/L$ and $k = -2\pi/L$, respectively, also with maximum values of L. The term which is centered about $k = 0$ is the mirror image of the term centered at $k = 2\pi/L$ about the point $k = \pi/L$, as well as the mirror image of the term involving K_4 about the point $k = -\pi/L$. However, because the terms involving K_3 and K_4 are accompanied by a multiplying factor of $(\frac{1}{2})$

in the expression for Δ, these terms have less effect on the $G(k)$ characteristics for $\pi/L \leq |k| \leq 2\pi/L$ than does the term centered at $k = 0$ in the range $|k| \leq \pi/L$. All three of the additional terms are identically zero at $|k| = \pi/L$. Inspection shows that the effect on the $G(k)$ characteristics is always additive in the range $|k| < \pi/L$; whereas, in the range $\pi/L \leq |k| \leq 2\pi/L$ it may be additive or subtractive, depending on the number of finger pairs in the transducer. Thus, the inclusion of the "end correction", Δ, effects a "levelling out" of the side lobe response in the $G(k)$ characteristics, as shown in Figs. 7.3(b) - 7.3(d).

7.5 An Alternative Approach to the Calculation of Transducer Admittance Characteristics

In section 7.2.2, it was observed that both the simple "mathematical model" and the approach of Smith et al.[58] require a "scale factor" for the calculations of absolute admittance values. In the Stanford model it is usual to rely upon experimentation; however, this need not be the case for either model. It is possible to obtain the required factor from the general theory presented earlier by performing a calculation of the transducer conductance at the "resonant" frequency. This value can then be used as a scaling factor for equation (7.11a) (or the Stanford model) which can rapidly calculate the complete conductance characteristic with considerable accuracy, as previously shown. Once the conductance $G(k)$ has been determined, the susceptance $B(k)$ can be found numerically, using the procedure outlined by Malamwar and Epstein[48]. These calculations can be performed in the variable k directly; however, if the admittance as a function of frequency is desired, one must have knowledge of the dispersion relation for the structure.

7.6 Summary

In this chapter we have introduced a simple mathematical model of an ID transducer based on the concept of the transducer acting as a continuous generating function. It was shown that this model predicts behaviour which is essentially identical to that of the model proposed by Smith et al.[58]; but, in addition, it can be used to show more directly how the surface waves are affected by the transducer as they propagate along its length. This 'model' was also used to examine the "end correction" of an ID transducer; and it was shown that, for a transducer whose length is greater than a few finger pairs, this correction has negligible effect. An alternative approach to the calculation of admittance characteristics was also presented.

CHAPTER VIII

CONCLUSIONS

An analytical and computational procedure for studying the acoustic surface wave excitation of layered structures, by means of an ID transducer, has been developed. A "low coupling" approach has been used throughout and the analysis can be applied to an ID transducer located on the free surface or at the interface, and with or without a metallic plating. Comparison between the calculated and measured admittance characteristics of ID transducers for both free surface and layered structures have been used to establish the validity of the theory. These comparisons have also shown that the low coupling approach can be applied to certain orientations of high coupling materials with reasonable accuracy. The theoretical results have also been shown to agree with recent theoretical work on the "coupling constants" of layered structures[61].

The wave behaviour within the transducer region has been demonstrated and explained on the basis of two surface waves propagating in opposite directions. A simple mathematical model which can be used to describe the wave behaviour within the ID transducer, as well as calculate the admittance characteristics of the transducer, has also been developed. The results calculated from this model have been compared to the modelling techniques of Smith et al.[58] and it has been shown that the two approaches are very similar. This simple model has also been used to examine the effect of the distorted electric field at the ends of the ID transducer and a procedure whereby both the general theory and the simple model can be used to rapidly and accurately predict the admittance characteristics of an ID transducer has been presented.

APPENDIX A

In the application of the Fourier transform, defined by equations (2.13) and (2.14), one must remember that, for all "x", the displacements U_1 and U_3, as well as the stresses $T_{11} = T_1$ and $T_{31} = T_{13} = T_5$, are continuous. To see how this effects the application of the Fourier transform, let us return, for a moment, to Newton's Law, equation (2.3):

$$\rho \frac{\partial^2 U_i}{\partial t^2} = \frac{\partial T_{ij}}{\partial x_j} \quad . \qquad (2.3)$$

By writing out the components of this equation in full, and assuming a time dependence $e^{-i\omega t}$, one has:

$$\partial T_{11}/\partial x + \partial T_{12}/\partial y + \partial T_{13}/\partial z + \rho\omega^2 U_1 = 0 \qquad (A.1a)$$

$$\partial T_{21}/\partial x + \partial T_{22}/\partial y + \partial T_{23}/\partial z + \rho\omega^2 U_2 = 0 \qquad (A.1b)$$

$$\partial T_{31}/\partial x + \partial T_{32}/\partial y + \partial T_{33}/\partial z + \rho\omega^2 U_3 = 0 \quad . \qquad (A.1c)$$

The T_{ij} are defined by equation (2.1):

$$T_{ij} = c_{ijkl} S_{kl} + e_{mij}\, \partial\phi/\partial x_m \quad . \qquad (2.1)$$

In section 2.2.1, the following symmetry restrictions were imposed on the c_{ijkl} and the e_{mij}:

$$c_{16} = c_{14} = c_{56} = c_{36} = c_{34} = c_{45} = 0$$

and

$$e_{16} = e_{14} = e_{36} = e_{34} = 0 \; ,$$

in matrix notation. As was shown in section 2.2.1, these restrictions eliminate both T_{12} and T_{23} and uncouple the U_2 displacement which, in the absence of a driving term, will not be excited. With these restrictions, the equations (A.1) reduce to

$$\frac{\partial T_1}{\partial x} + \frac{\partial T_5}{\partial z} + \rho\omega^2 U_1 = 0 \qquad (A.2a)$$

and

$$\frac{\partial T_5}{\partial x} + \frac{\partial T_3}{\partial z} + \rho\omega^2 U_3 = 0 \quad . \qquad (A.2b)$$

In section 2.1.3 it was shown that, in the low coupling approximation, the potential function in equation (2.1) becomes that of the transducer only. With the above symmetry restrictions, and assuming the low coupling approximation, the T_i of equations (A.2) are given by:

$$T_1 = c_{11}\frac{\partial U_1}{\partial x} + c_{15}\frac{\partial U_1}{\partial z} + c_{15}\frac{\partial U_3}{\partial x} + c_{13}\frac{\partial U_3}{\partial z} + e_{11}\frac{\partial \phi}{\partial x} + e_{31}\frac{\partial \phi}{\partial z}$$

$$T_3 = c_{13}\frac{\partial U_1}{\partial x} + c_{35}\frac{\partial U_1}{\partial z} + c_{35}\frac{\partial U_3}{\partial x} + c_{33}\frac{\partial U_3}{\partial z} + e_{13}\frac{\partial \phi}{\partial x} + e_{33}\frac{\partial \phi}{\partial z}$$

$$T_5 = c_{15}\frac{\partial U_1}{\partial x} + c_{55}\frac{\partial U_1}{\partial z} + c_{55}\frac{\partial U_3}{\partial x} + c_{35}\frac{\partial U_3}{\partial z} + e_{15}\frac{\partial \phi}{\partial x} + e_{35}\frac{\partial \phi}{\partial z} \ ,$$

and the equations (A.2) are identical with (2.12). Applying the Fourier transform defined by (2.13) to equations (A.2) gives

$$\int_{-\infty}^{\infty}\frac{\partial T_1}{\partial x}e^{ik}\,dx + \frac{\partial}{\partial z}\int_{-\infty}^{\infty}T_5 e^{-ikx}dx + \rho\omega^2\int_{-\infty}^{\infty}U_1 e^{-ikx}dx = 0$$

and

$$\int_{-\infty}^{\infty}\frac{\partial T_5}{\partial x}e^{-ikx}dx + \frac{\partial}{\partial z}\int_{-\infty}^{\infty}T_3 e^{-ikx}dx + \rho\omega^2\int_{-\infty}^{\infty}U_3 e^{-ikx}dx = 0 \quad .$$

Since T_1 and T_5 are continuous, this reduces to[59]

$$ik\overline{T}_1 + \frac{\partial}{\partial z}\overline{T}_5 + \rho\omega^2\overline{U}_1 = 0$$

and

$$ik\overline{T}_5 + \frac{\partial}{\partial z}\overline{T}_3 + \rho\omega^2\overline{U}_3 = 0 \ ,$$

where the "‾" represents the transformed function.

Now consider the value of $\overline{T}_1$:

$$\overline{T}_1 = c_{11}\int_{-\infty}^{\infty}\frac{\partial U_1}{\partial x}\,e^{ikx}dx + c_{15}\frac{\partial}{\partial z}\int_{-\infty}^{\infty}U_1 e^{-ikx}dx + c_{15}\int_{-\infty}^{\infty}\frac{\partial U_3}{\partial x}\,e^{-ikx}dx$$

$$+ c_{13}\frac{\partial}{\partial z}\int_{-\infty}^{\infty}U_3 e^{-ikx}dx + e_{11}\int_{-\infty}^{\infty}\frac{\partial\phi}{\partial x}\,e^{-ikx} + e_{31}\frac{\partial}{\partial z}\int_{-\infty}^{\infty}\phi e^{-ikx}dx \;.$$

Since U_1 and U_3 are continuous, this can be written[59]

$$\overline{T}_1 = c_{11}ik\overline{U}_1 + c_{15}\frac{\partial}{\partial z}\overline{U}_1 + c_{15}ik\overline{U}_3 + c_{13}\frac{\partial}{\partial z}\overline{U}_3$$
$$+ e_{31}\frac{\partial}{\partial z}\overline{\phi} + e_{11}\int_{-\infty}^{\infty}\frac{\partial\phi}{\partial x}\,e^{-ikx}dx \;;$$

and because the function $\phi(x,z)$, as defined by (2.10),

$$\phi(x,z) = \begin{cases}\Sigma A_n f_n(z)\cos(n\pi x/L), & |x| < D/2\\ 0, & |x| > D/2\end{cases} \qquad (2.10)$$

is not a continuous function of "x", the final term must be evaluated by parts as follows:

$$\int_{-\infty}^{\infty}\frac{\partial\phi}{\partial x}\,e^{-ikx}dx = \phi e^{-ikx}\Big|_{-\infty}^{\infty} + ik\int_{-\infty}^{\infty}\phi e^{-ikx}dx$$
$$= \phi e^{-ikx}\Big|_{-D/2}^{D/2} + ik\overline{\phi} \;.$$

Because ϕ is an even function of "x", this can be written

$$-2i\phi\,(D/2)\sin\,(kD/2) + ik\,\overline{\phi}\;,$$

where $\phi(D/2) = \phi(D/2,z)$. Thus $\overline{T}_1$ is given by:

$$\overline{T}_1 = c_{11}ik\overline{U}_1 + c_{15}\frac{\partial}{\partial z}\overline{U}_1 + c_{15}ik\overline{U}_3 + c_{13}\frac{\partial}{\partial z}\overline{U}_3 + e_{31}\frac{\partial}{\partial z}\overline{\phi}$$
$$+ e_{11}ik\overline{\phi} - 2ie_{11}\phi(D/2)\sin(kD/2) \;.$$

The terms $\overline{T}_1$ and $\overline{T}_3$ can be evaluated in a similar fashion, and the transformed equations (A.2) can be written

$$\begin{bmatrix} Y_{11} & Y_{12} \\ Y_{12} & Y_{22} \end{bmatrix} \times \begin{bmatrix} \overline{U}_1 \\ \overline{U}_3 \end{bmatrix} = \begin{bmatrix} \overline{\theta}_1 \\ \overline{\theta}_3 \end{bmatrix} \quad ; \qquad (A.3)$$

where:

$$Y_{11} = c_{55}\frac{\partial^2}{\partial z^2} + 2c_{15}ik\frac{\partial}{\partial z} - c_{11}k^2 + \rho\omega^2$$

$$Y_{22} = c_{33}\frac{\partial^2}{\partial z^2} + 2c_{35}ik\frac{\partial}{\partial z} - c_{55}k^2 + \rho\omega^2$$

$$Y_{12} = c_{35}\frac{\partial^2}{\partial z^2} + [c_{55} + c_{13}]ik\frac{\partial}{\partial z} - c_{15}k^2$$

$$\overline{\theta}_1 = -\left[e_{35}\frac{\partial^2}{\partial z^2} + (e_{15} + e_{31})ik\frac{\partial}{\partial z} - e_{11}k^2\right]\overline{\phi} + 2ie_{15}\frac{\partial}{\partial z}\phi(D/2)\sin(kD/2) - 2ke_{11}\phi(D/2)\sin(kD/2)$$

$$\overline{\theta}_3 = -\left[e_{33}\frac{\partial^2}{\partial z^2} + (e_{13} + e_{35})ik\frac{\partial}{\partial z} - e_{15}k^2\right]\overline{\phi} + 2ie_{13}\frac{\partial}{\partial z}\phi(D/2)\sin(kD/2) - 2ke_{15}\phi(D/2)\sin(kD/2) \quad .$$

Now consider the functions $\overline{\phi}$ and $\phi(D/2)$. By using (2.10), the term $\overline{\phi}$ is defined by

$$\overline{\phi} = \int_{-\infty}^{\infty}\phi(x,z)e^{-ikx}dx = \sum A_n f_n(z)\int_{-D/2}^{D/2}\cos(n\pi\, x/L)e^{-ikx}dx$$
$$= \sum A_n F_n(k) f_n(z) \quad ,$$

where

$$F_n(k) = \frac{\sin[(k-n\pi/L)D/2]}{(k-n\pi/L)} + \frac{\sin[(k+n\pi/L)D/2]}{(k+n\pi/L)} \quad . \qquad (A.4)$$

The term $\phi(D/2)$ is given by

$$\phi(D/2) = \sum A_n f_n(z)\cos(n\pi\, D/2L) \quad .$$

Since $D/2 = m_o L$, where m_o is an integer, this is equal to

$$\phi(D/2) = \sum A_n N_n f_n(z) \quad , \qquad (A.5)$$

where

$$N_n = \begin{cases} -1, & n-m_o \text{ is odd} \\ +1, & n-m_o \text{ is even} \end{cases} \quad .$$

APPENDIX B

As shown in section 2.1.3, when using the "low coupling" approximation the only electric potential function appearing in the wave equations is that of the transducer imbedded in a dielectric non-piezoelectric medium. In this case Laplace's equation is given by (2.7),

$$\left(\varepsilon_1 \frac{\partial^2}{\partial x^2} + 2\varepsilon_5 \frac{\partial^2}{\partial x \partial z} + \varepsilon_3 \frac{\partial^2}{\partial z^2}\right)\phi = 0 \quad , \qquad (2.7)$$

using matrix notation for the ε_i. It has been assumed that the transducer fingers are very long and compared to their width and thus terms involving $\partial/\partial y$ do not appear in (2.7).

If the material dielectric tensor has only diagonal terms, equation (2.7) can be written

$$\left[\left(\frac{\varepsilon_1}{\varepsilon_3}\right)\frac{\partial^2}{\partial x^2} + \frac{\partial^2}{\partial z^2}\right]\phi = 0 \quad . \qquad (B.1)$$

Assuming, for the moment, that the material is dielectrically isotropic, $\varepsilon_1 = \varepsilon_3$ and (B.1) reduces to

$$\left(\frac{\partial^2}{\partial x^2} + \frac{\partial^2}{\partial z^2}\right)\phi = 0 \quad . \qquad (B.2)$$

Equation (B.2) is the differential equation to which numerical solutions are obtained by the program "CAPAX", over the region shown in Fig. 2.4,* as described in section 2.1.4. The numerical solutions to (B.2), within the transducer, are "discrete" and given by

$$\phi = \varphi(x,z_i) = \sum_n A_n \delta_n(z_i)\cos(n\pi\, x/L) \quad , \qquad (2.9a)$$

as shown in section 2.1.4. It is desirable that a continuous potential function

---

* Fig. 2.4 will be found on page 17 .

$$\Psi(x,z) = \sum_n A_n f_n(z) \cos(n\pi x/L) \qquad (B.3)$$

be found to satisfy (B.2). On substitution of the solution (B.3) into (B.2) one obtains the following differential equation for $f_n(z)$:

$$\partial^2 f_n(z)/\partial z^2 = \left(\frac{n\pi}{L}\right)^2 f_n(z) \quad . \qquad (B.4)$$

The general solution to (B.4) is

$$f_n(z) = a_n e^{-\eta_n z} + b_n e^{\eta_n z} \quad ,$$

where $\eta_n = \pm n\pi/L$. Thus, the solution $\Psi(x,z)$ can be written

$$\Psi(x,z) = \sum_n A_n (e^{-\eta_n z} + r_n e^{\eta_n z}) \cos(n\pi x/L) \quad , \qquad (B.5)$$

depending on the location of the transducer and the region of interest. This will be discussed in greater detail in the following section, for the moment assume that the transducer is located at the layer substrate interface. For this situation, $\eta_n = +n\pi/L$ in the layer and $\eta_n = -n\pi/L$ in the substrate. In the substrate, $r_n = 0$ for all cases, while in the layer $r_n = 0$ in the absence of a metallic plating. In the plated layer case, the tangential electric field (E_x) must be zero, for all x, at $z = H$, which requires that

$$e^{-n\pi H/L} + r_n e^{n\pi H/L} = 0$$

or

$$r_n = -e^{-2\pi nH/L} \quad .$$

In the case where the transducer is located on the layer surface and the interface is plated, $E_x = 0$ at $z = 0$, and thus $r_n = -1$, from (B.5).

The procedure for establishing (B.5), using "CAPAX" would be as follows:

(1) Perform the "CAPAX" computation to calculate the potential at every point on the grid described in section 2.1.4.

(2) Choose any level z_i in the region of interest (either layer or substrate) and expand the potential at that level in a Fourier series as indicated in section 2.1.4. (In most situations it is best to choose z_i within the layer.) Thus, using (B.5), the potential at this level can be written

$$\psi(x,z_i) = \sum_n B_n(z_i)\cos(n\pi\, x/L) \quad ,$$

where

$$B_n = A_n\left[e^{-\eta_n z_i} + r_n e^{\eta_n z_i}\right] \quad .$$

(3) From the chosen region and the boundary conditions one can then determine η_n and r_n.

(4) Having determined r_n and η_n, and knowing both z_i and $B_n(z_i)$, the constant A_n is determined from

$$A_n = B_n(z_i)\Big/\left[e^{-\eta_n z_i} + r_n e^{\eta_n z_i}\right] \quad .$$

(5) Replacing z_i by the continuous variable z, the potential function in the chosen region can then be written

$$\psi(x,z) = \sum A_n\left[e^{-\eta_n z} + r_n e^{\eta_n z}\right]\cos(n\pi\, x/L) \quad .$$

The role played by the program "CAPAX" is very important for it provides the potential at every point on the computation grid, by solving equation (B.2) while taking into account the necessary boundary conditions. These conditions include:

(1) different isotropic dielectric constants in the three separate regions (substrate, layer, vacuum)

(2) existance of metallic plating (if desired)

(3) tangential electric field equal to zero on transducer fingers (and plating if present)

(4) normal component of D continuous in gaps between fingers and at interfaces where no plating is present.

These conditions are reflected in the coefficients B_n of the Fourier expansion of the potential function at the level z_i. However, once the Fourier expansion within a particular region is established at a level z_i (step No. 2 above), the derivation of $\varphi(x,z)$ for that particular region follows as outlined above (steps No. 3 - No. 5).

<u>B.2</u>

In this section, the means of preparing the "CAPAX" program to handle different transducer configurations and the determination of the functions $f_n(z)$ in the regions of interest will be discussed. There are three basic cases to be considered:

(1) transducer at interface, plated or unplated layer

(2) transducer on free surface of layer, possible plating at interface

(3) transducer at $z = 0$, no layer.

The argument list of "CAPAX" contains the following variables:

(1) an integer "IPLATE" which is set to zero if the layer is plated, and not zero, if unplated

(2) ε_1, the isotropic dielectric constant of the layer

(3) ε_2, the isotropic dielectric constant of the substrate

(4) a variable "DL" = d/L (L is finger spacing, d is finger width)

(5) a variable "TD" = finger thickness/d (in our case, TD has been assumed essentially equal to zero in section 2.1.2)

(6) a variable "HL" = H/L (H is layer thickness).

The dielectric constant of the material above the layer vacuum is assumed to be unity, and for "HL" > 1 an infinite layer is assumed. A "Block Data" subroutine provides the appropriate shift operators for "unipolar" or "bipolar" drive. The program returns the capacitance/meter/finger-half-pair and the potential at every point on the grid as mentioned in section 2.1.4. By suitable alteration of the six input variables, it is possible to make "CAPAX" analyze any of the three transducer configurations mentioned above.

Consider the configuration with the transducer at the interface and a plated, or unplated, layer. This is the configuration for which "CAPAX" was initially intended, and no alteration of the input variables is required. In the case of the plated layer, "HL" should not exceed unity or the effect of the plating will be ignored.

When the potential array is filled, it is convenient to choose the level $z_1 = 0$ for the Fourier expansion. This results from having previously chosen the finger thickness to be zero. Thus, the layer potential at $z = 0$ can be given by

$$\hat{\Psi}(x,0) = \sum_n \hat{B}_n(0)\cos(n\pi x/L) \quad . \qquad (B.6)$$

("^" refers to the layer solutions.) As shown in the previous section, the function $f_n(z)$ for the layer can then be written

$$\hat{f}_n(z) = \hat{A}_n\left[e^{-n\pi z/L} + \hat{r}_n e^{n\pi z/L}\right] \quad (\hat{r}_n = 0 \text{ if unplated}),$$

where $\hat{A}_n = \hat{B}_n(0)/(1+\hat{r}_n)$.

One can also write the potential function in the substrate, at $z_1 = 0$, as

$$\varphi(x,0) = \sum_m B_m(0)\cos(m\pi x/L) \ . \qquad \text{(B.7)}$$

The functions $f_m(z)$ in the substrate are

$$f_m(z) = A_m e^{m\pi z/L}$$

since $r_m = 0$ in this region. Since the potential in the layer and that in the substrate must be equal at $z = 0$ (zero finger thickness),

$$\sum_n \hat{A}_n[1+\hat{r}_n]\cos(n\pi x/L) = \sum_m A_m \cos(m\pi x/L) \quad .$$

For this to be true for all x in the range $0 \leq x \leq L$, the "cell" over which the Fourier expansion is generated, the Fourier coefficients must be identical and hence

$$A_n = \hat{A}_n(1+\hat{r}_n) \quad .$$

Thus, for this configuration, with zero finger thickness, the Fourier expansion at $z_1 = 0$ completely determines the potential function in both regions.

Now consider the second configuration of interest, that with the transducer located on top of the layer. To analyze this situation with "CAPAX", certain modifications in the input variables are required. First, divide all of the isotropic dielectric constants by that of the substrate, ϵ_S, forming a new set of isotropic dielectric constants:

$$\varepsilon'_S = 1$$
$$\varepsilon'_L = \varepsilon_L/\varepsilon_S$$
$$\varepsilon'_o = 1/\varepsilon_S \quad .$$

After performing this operation, the dielectric constants to "CAPAX" are entered as

$$\varepsilon_1 = \varepsilon'_L$$

and

$$\varepsilon_2 = \varepsilon'_o \quad .$$

From a computational standpoint, this operation interchanges the substrate and the region above the layer, and scales the dielectric constants so that "CAPAX" can assume a unity dielectric constant above the layer. This procedure does not alter the harmonic content of the potential function; however, it is necessary to multiply the calculated value of capacitance/meter/finger-half-pair by the value of the isotropic substrate dielectric constant to obtain the correct value of capacitance. If a metallic plate is present at the layer-substrate interface, "IPLATE" = 0, otherwise "IPLATE" = 1. For the Fourier expansion of the potential function, choose the level at which the transducer is located, $z_i = H$. The "CAPAX" program fills the computation grid as if the transducer were located at $z_i = 0$, and thus the potential $\hat{\varphi}(x,H)$ corresponds to $\sum_n \hat{B}_n(0)\cos n\pi x/L$ for this case. Again, it is desirable to write the potential function in the form

$$\hat{\varphi}(x,z) = \sum_n \hat{A}_n \left[e^{-\hat{\eta}_n z} + \hat{r}_n e^{\hat{\eta}_n z} \right] \cos\left(n\pi x/L\right) \quad . \qquad \text{(B.8)}$$

If the interface is unplated, $\hat{r}_n = 0$; but if it is plated

$$\hat{\varphi}(x,0) = 0 \quad ,$$

and $\hat{r}_n = -1$. Setting $\hat{\eta}_n = -n\pi x/L$, (B.8) can then be written

$$\hat{\varphi}(x,z) = \sum_n \hat{A}_n \left[e^{n\pi z/L} + \hat{F}_n e^{-n\pi z/L} \right] \cos(n\pi x/L) ,$$

where

$$\hat{A}_n = \hat{B}_n(0) \Big/ \left[e^{n\pi H/L} + \hat{F}_n e^{-n\pi H/L} \right] \quad .$$

The potential function in the substrate can be written

$$\varphi(x,z) = \sum_m A_m e^{m\pi z/L} \cos(m\pi x/L),$$

as has been done previously. In the case of a plated interface, all $A_m = 0$; however, if the interface is not plated

$$\sum_m A_m \cos(m\pi x/L) = \sum_n \hat{A}_n \cos(n\pi x/L) \quad . \; (0 < x < L)$$

Again, the above expressions must be equal on a term by term basis and $A_n = \hat{A}_n$. Thus, the program "CAPAX" can be used to analyse this configuration by suitable alteration of the input variables. The harmonic analysis at the level of the transducer yields all the information needed to construct the potential function throughout both regions.

The third configuration, that with no layer and the transducer located at $z = 0$, is a trivial case of the second configuration. To analyze this case, the input variables to "CAPAX" would be altered to read:

$\varepsilon_1 = \varepsilon_S$

$\varepsilon_2 = 1$

"HL" > 1 .

The harmonic analysis is performed at $z_1 = 0$ such that

$$\varphi(x,0) = \sum_n B_n(0) \cos(n\pi x/L) .$$

The continuous functional form of the substrate potential is then given by

$$\psi(x,z) = \sum_n A_n e^{n\pi z/L} \cos(n\pi x/L) \ ,$$

where

$$A_n = B_n(0) \ .$$

<u>B.3</u>

The results of the preceding sections have been derived on the assumption of an isotropic dielectric constant in all of the regions. This assumption was required to accomodate the "CAPAX" program; however, having obtained the "isotropic" results, it is possible to correct for this assumption. Let us return to equation (B.1),

$$\left[\left(\frac{\varepsilon_1}{\varepsilon_3}\right)\frac{\partial^2}{\partial x^2} + \frac{\partial^2}{\partial z^2}\right]\phi = 0 \ , \qquad \text{(B.1)}$$

and assume a solution

$$\phi = \psi'(x,z) = \sum A'_n f'_n(z) \cos(n\pi x/L) \ .$$

Substituting into (B.1) results in the equation

$$\frac{\partial^2 f'_n}{\partial z^2} = \left(\frac{\varepsilon_1}{\varepsilon_3}\right)\left(\frac{n\pi}{L}\right)^2 f'_n \ . \qquad \text{(B.9)}$$

The solution to (B.9) is

$$f'_n(z) = a'_n e^{M_n z} + b'_n e^{-M_n z} \ ,$$

where

$$M_n = \pm\left(\frac{\varepsilon_1}{\varepsilon_3}\right)^{\frac{1}{2}}\left(\frac{n\pi}{L}\right) \ .$$

Thus one has

$$\psi'(x,z) = \sum A'_n \left[e^{-M_n z} + r'_n e^{M_n z}\right] \cos(n\pi x/L) \qquad \text{(B.10)}$$

for each region. In the substrate, (B.10) would be written

$$\phi'(x,z) = \sum A'_n \, e \left(\frac{\varepsilon_1}{\varepsilon_3}\right)^{\frac{1}{2}} n\pi \, z/L \cos\,(n\pi \, x/L),$$

and is identical to the results of Joshi and White[36].

The somewhat modified potential function of (B.10) will replace that of (B.5) and can be calculated in the same fashion as outlined in section (B.1), with only a few minor alterations in the procedure. The altered procedure would be as follows: (* are changed)

(1) Perform "CAPAX" calculations assuming an isotropic dielectric constant.

(*2) Choose the <u>level of the transducer</u>, $z_i = 0$ or $z_i = H$, and expand the potential function in a Fourier series at that level. Thus, the potential function at this level is

$$\phi(x,z_i) = \sum_n B_n(z_i) \cos(n\pi \, x/L)$$

(*3) Determine M_n, $\hat{M}_n$ and $\hat{r}'_n$ ($r'_n = 0$, always). In the absence of a metallic plating, $\hat{r}'_n = 0$; otherwise,

$$\hat{r}'_n = -1 \quad \text{or} \quad \hat{r}'_n = -e^{-2\hat{M}_n H}, \text{ as before.}$$

(*4) The constant $\hat{A}'_n$ is then given by

$$\hat{A}'_n = \hat{B}_n(z_i) \Big/ \left[e^{-\hat{M}_n z_i} + \hat{r}'_n e^{\hat{M}_n z_i} \right], \text{ as before.}$$

The coefficient A'_n is then defined by

$$A'_n = \hat{A}'_n [1 + \hat{r}'_n] \quad .$$

(*5) Replacing z_i by z, the potential functions for layer and substrate are

$$\psi(x,z) = \sum_n \hat{A}_n \left[e^{-\hat{M}_n z} + \hat{r}'_n \, e^{\hat{M}_n z} \right] \cos(n\pi \, x/L)$$

and

$$\psi(x,z) = \sum_n A_n \left[e^{-M_n z} \right] \cos(n\pi \, x/L) \quad ,$$

respectively.

By choosing the level of the transducer for the Fourier expansion, we have insured that the potential difference between adjacent electrodes, as given by (B.10), is unchanged from (B.5). This alteration does not provide a perfect correction, for this step will have affected the boundary condition involving the continuity of the normal component of D. However, since for most materials ε_1 is approximately equal to ε_3, it is a reasonable first step to correct for the "isotropic" dielectric constant assumption.

APPENDIX C

This appendix is devoted to the evaluation of various integrals which are required in section 2.2.6. The first integral, in section C.1, is included for instructive purposes, while the integral of section C.2 is a well known Fourier transform.

C.1

Consider the integral

$$\int_{-\infty}^{\infty} \frac{e^{iky}}{k}\, dk \quad , \qquad \text{(C.1a)}$$

where the range of integration is the real axis. The "pole" at $k = 0$ is located on the path of integration, and for $y > 0$ it can be removed by using the contour C_o, given by[31]:

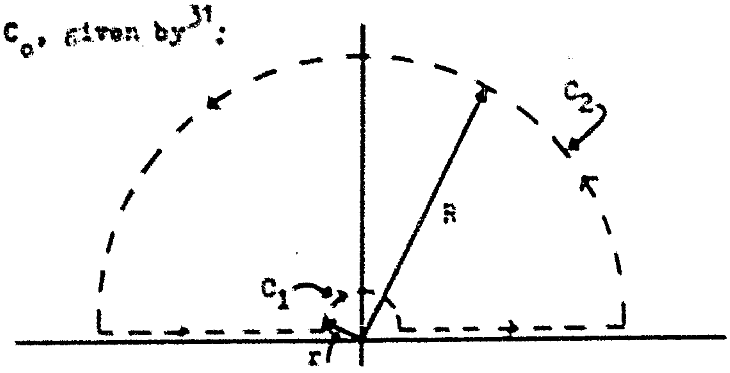

Thus,

$$\oint_{C_o} = \int_{-R}^{-r} + \int_{C_1} + \int_{r}^{R} + \int_{C_2}$$

and, since there are no poles within C_o,

$$\oint_{C_o} \frac{e^{iky}}{k}\, dk = 0 \quad .$$

Along the semicircle C_2, k is given by $k = R\,e^{i\theta}$, $0 \leq \theta \leq \pi$. Thus, the integral along this portion of C_o can be written

$$i\int_0^{\pi} e^{-yR\sin\theta} e^{iyR\cos\theta} d\theta \quad .$$

The absolute value of this integral is dominated by[31]

$$\int_0^{\pi} e^{-yR\sin\theta} d\theta = 2\int_0^{\pi/2} e^{-yR\sin\theta} d\theta < 2\int_0^{\pi/2} e^{-2\theta yR/\pi} d\theta = \frac{\pi}{yR}\left(1-e^{-yR}\right) \quad .$$

Thus, for $y > 0$, this integral tends to zero as $R \to \infty$. The integral over C_o can then be written

$$\oint_{C_o} = \int_{-\infty}^{-r} + \int_{r}^{\infty} + \int_{C_1} = 0 \quad .$$

Over the contour C_1, $k = r\,e^{i\theta}$, $\pi \leq \theta \leq 0$, and one can write

$$\int_{C_1} \frac{e^{iky}}{k}\, dk = \int_{C_1} \frac{dk}{k} + \int_{C_1} \frac{(e^{iky}-1)}{k}\, dk = \int_{\pi}^{0} i d\theta + i\int_{\pi}^{0} \left[e^{iyr(e^{i\theta})} - 1\right] d\theta \quad .$$

In the limit, as $r \to 0$, the last integral above will vanish[31], and one is left with

$$\oint_{C_o} \frac{e^{iky}}{k}\, dk = \int_{-\infty}^{0} \frac{e^{iky}}{k}\, dk + \int_{0}^{\infty} \frac{e^{iky}}{k}\, dk + \int_{\pi}^{0} i d\theta = 0 \quad .$$

Thus, the integral (C.1a) has the value $i\pi$, for $y > 0$. In a similar fashion, (C.1a) for $y < 0$ has the value $-i\pi$. If $y = 0$, the integral (C.1a) reduces to

$$\int_{-\infty}^{\infty} \frac{dk}{k} = 0 \quad ,$$

since the integrand is an odd function of k.

To summarize:

$$\int_{-\infty}^{\infty} \frac{e^{iky}}{k}\, dk = \begin{cases} i\pi, & y > 0 \\ 0, & y = 0 \\ -i\pi, & y < 0 \end{cases} \quad . \qquad \text{(C.1b)}$$

C.2

Consider the integral

$$\int_{-\infty}^{\infty} \frac{\sin(k\,D/2)}{k}\, e^{ikx} dk \;, \quad D > 0 \quad . \tag{C.2a}$$

This can be written

$$(1/2i)\left\{ \int_{-\infty}^{\infty} \frac{e^{ik(x+D/2)}}{k}\, dk - \int_{-\infty}^{\infty} \frac{e^{ik(x-D/2)}}{k}\, dk \right\} \quad .$$

Using the results (C.1b), it can be seen that

$$\int_{-\infty}^{\infty} \frac{\sin(k\,D/2)}{k}\, e^{ikx} dk = \begin{cases} \pi \;, & 0 \leq |x| < D/2 \\ \pi/2, & |x| = D/2 \\ 0 \;, & |x| > D/2 \end{cases} \;, \tag{C.2b}$$

which is a well known result[4].

C.3

Now consider the integral

$$\int_{-\infty}^{\infty} \frac{\sin[(k+A)D/2]}{(k+A)}\, f(k,z) e^{ikx} dk \qquad D > 0 \quad , \tag{C.3a}$$

where A is real and $f(k,z)$ has no poles in the k-plane, but there is the possibility of branch points occurring in $f(k,z)$. (In the evaluation of (2.32) there are no branch points, while in (2.35) there are.) The variable z can be considered a parameter. In the advent of branch points, assume that their locations are known and given by K_1, K_2, ..., K_n, where n must be finite. (The means of locating the branch points in the evaluation of (2.35) is considered in Appendix D.2.) Substituting $k' = k + A$, (C.3a) can be written

$$\frac{e^{-iAx}}{2i}\left\{ \int_{-\infty}^{\infty} 6(k')\, \frac{e^{ik'(x+D/2)}}{k'}\, dk' - \int_{-\infty}^{\infty} 6(k')\, \frac{e^{ik'(x-D/2)}}{k'}\, dk' \right\} \;,$$

where $g(k') = f(k' - A, z)$. Hence (C.3a) can be determined by evaluating integrals of the form

$$\int_{-\infty}^{\infty} \frac{g(k')}{k'} e^{ik'y}\, dk' \quad .$$

Consider first the case for $y > 0$. One wishes to use a contour identical to that used in C.1, enclosing the upper-half of the k'-plane; however, one must take into account those branch points which are located in the upper-half of k'-space and draw the contour so as to pass around these points, when they exist, and not cross the branch cuts*. Such a contour is :

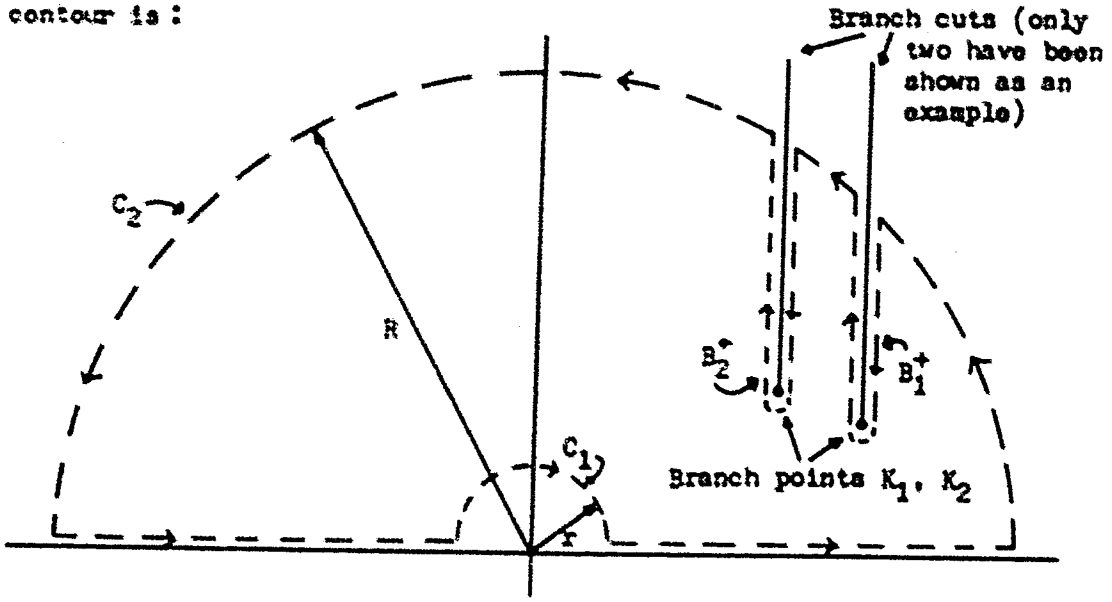

This contour remains on the same sheet of the Riemann surface for k'^{31}; and since there are no poles contained within the contour,

$$\int_{-R}^{-r} + \int_{C_1} + \int_{r}^{R} + \sum_q \int_{B_q^+} + \int_{C_2} = 0 \quad .$$

---

* Since A is real, those branch points located in the upper-half of k-space are also located in the upper half of k'-space.

The summation over the index q represents those contours, B_q^+, which exclude the branch points in the upper-half plane, as shown. Along that portion of the contour denoted by C_2, k' is given by $R\,e^{i\theta}$. One can then show, in a fashion similar to that used in C.1, that the integral

$$\int \frac{g(k')}{k'}\, e^{ik'y} dk$$

vanishes along any portion of C_2 as $R \to \infty$, providing $g(k')$ is bounded (for all z) along the contour C_2 as $R \to \infty$. That $g(k')$ remains bounded implies that the branch cuts have been properly chosen[14]. (The means of properly choosing the branch cuts is shown in Appendix D.3).

As in the evaluation of (C.1a), the integral over the contour C_1 can be written

$$i \int_{\pi}^{0} g(r,\theta) d\theta + \int_{C_1} \frac{g(k')}{k'} \left[e^{ik'y} - 1 \right] dk' \quad .$$

Since $g(k')$ remains finite in the limit as $r \to 0$, (no poles in the k-plane) the second integral above will vanish. The function $g(k')$ is complex and can be written $g(k') = g'(k') + i\, g''(k')$, which when substituted into the first integral above gives

$$i \int_{\pi}^{0} g'(r,\theta) d\theta - \int_{\pi}^{0} g''(r,\theta)\, d\theta \quad .$$

Both of these integrals can be evaluated by use of the "mean value theorem" as follows:

$$i \int_{\pi}^{0} g(r,\theta) d\theta < [-i\pi\, g'(r,\theta_0') + \pi g''(r,\theta_0'')], \quad 0 < \theta_0' < \pi, \quad 0 < \theta_0'' < \pi \quad .$$

(Since $g(k')$ is complex, the real and imaginary parts must be separated, since the maximum values of the two parts will not necessarily occur at the same point on C_1.) Thus,

$$\lim_{r\to 0} \int_{C_1} \frac{g(k')}{k} e^{ik'y} dk \le -i\pi \lim_{r\to 0} \left[g'(r,\theta_o') + ig''(r,\theta_o'') \right] \quad .$$

In the limit, as $r\to 0$, the equality sign is used because θ has no meaning when $r = 0$; hence,

$$\int_{-\infty}^{\infty} \frac{g(k')}{k'} e^{ik'y} dk' = i\pi\, g(0) - \sum_q b_q^+(y), \quad y > 0 \quad .$$

The terms $b_q^+(y)$ represent the contributions from the branch points in the upper half plane.

In a similar fashion,

$$\int_{-\infty}^{\infty} \frac{g(k')}{k'} e^{ik'y} dk', \quad \text{for } y < 0 \ ,$$

can be evaluated, and the result is

$$-i\pi\, g(0) - \sum_p b_p^-(y) \quad ;$$

where $b_p^-(y)$ represents the contribution of the p^{th} branch point located in the lower-half of the k-plane. (Remember that the branch points in the lower-half plane are circled in the opposite sense to those in the upper-half plane.)

Thus, for $0 < |x| < D/2$, the integral (C.3a) has the value:

$$\pi f(-\lambda,z) e^{-i\lambda x} + \frac{1}{2i} \left\{ e^{-i\lambda D/2} \sum_p \int_{B_p^-} f(k,z) \frac{e^{ik(x-D/2)}}{(k+\lambda)} dk \right.$$

$$\left. - e^{i\lambda D/2} \sum_q \int_{B_q^+} f(k,z) \frac{e^{ik(x+D/2)}}{(k+\lambda)} dk \right\} \quad ;$$

where B_q^+ and B_p^- represent contours, of the type shown on the contour C_o, around the branch points located in the upper-half and lower-half of k-space, respectively.

For $x > D/2$, the integral (C.3a) has the value

$$-\sum_q \int_{B_q^+} \frac{\sin[(k+A)D/2]}{(k+A)} f(k,z) e^{ikx}\, dk \quad .$$

For $x = D/2$, the integral (C.3a) can be written

$$\frac{e^{-iAx}}{2i} \int_{-\infty}^{\infty} \frac{g(k')}{k'} \left(e^{ik'D} - 1\right) dk' \quad ;$$

and unless more is known about the nature of $g(k')$, i.e., "odd" or "even", this integral cannot be evaluated.

In section 2.2.6.3 it was observed that the actual contributions from the branch points are too involved to evaluate exactly, and hence will not be considered in the evaluation of the integrals (2.35) and (2.32). The solutions of (C.3a), as used in the evaluation of (2.32) and (2.35), can be then summarized as

$$\int_{-\infty}^{\infty} \frac{\sin[(k+A)D/2]}{(k+A)} f(k,z) e^{ikx} dk = \begin{cases} \pi f(-A,z) e^{-iAx}, & 0 < |x| < D/2 \\ 0, & |x| > D/2 \end{cases} ,$$

in the absence of branch point contributions.

C.4

A variation of the integral (C.3a) is the integral

$$\int_{-\infty}^{\infty} \sin(k\, D/2) g(k,z) e^{ikx} dk \qquad D > 0 \quad ,$$

where $g(k,z)$ has the same properties as $f(k,z)$ in C.3. The integral (C.4a) can be written

$$\frac{1}{2i}\left\{\int_{-\infty}^{\infty} g(k,z)e^{ik(x+D/2)}dk - \int_{-\infty}^{\infty} g(k,z)e^{ik(x-D/2)}dk\right\} \quad .$$

These integrals are of the form

$$\int_{-\infty}^{\infty} g(k,z)e^{iky}dk \quad .$$

For $y > 0$, the contour for the above integral is:

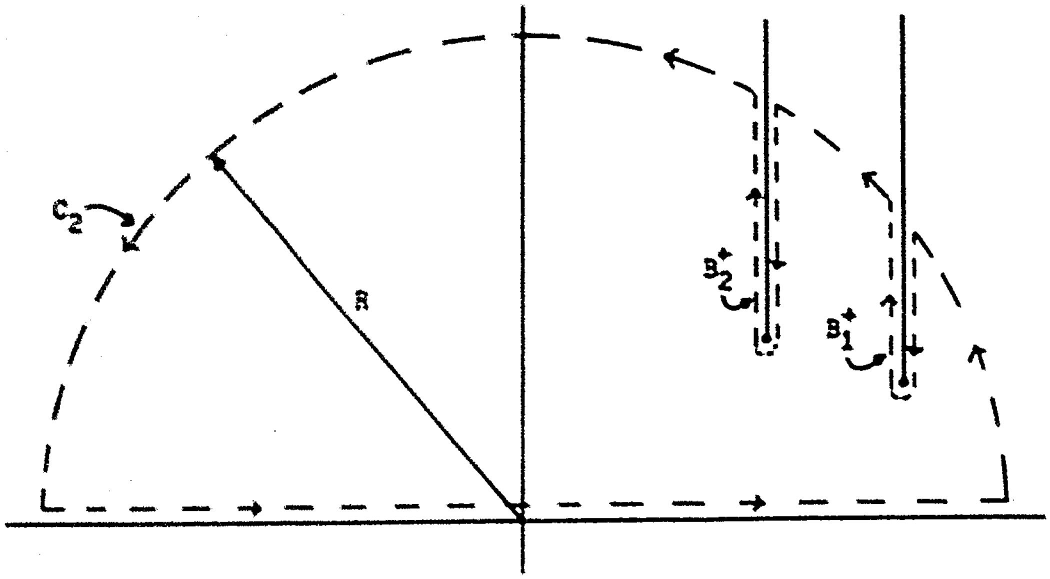

where the B_q^+ are the contours around the branch points in the upper-half plane, as in the previous section. (Again, only two such branch cut contours are shown as an example.) Since no poles are enclosed by this contour

$$\int_{-R}^{R} + \int_{C_2} + \sum_q \int_{B_q^+} = 0 \quad . \qquad (C.4b)$$

Unless more is known about the function $g(k,z)$, one cannot guarantee that the integral over C_2 will vanish as $R \to \infty$.

Considering first the particular integral solutions, given by (2.32) in section 2.2.6.2, the term $g(k,z)$ represents either $\exp(-M_n z)c_{jn}$ or $\exp(M_n z)d_{jn}$, and contains no branch points. As observed in section 2.2.6.1, the functions $c_{jn}(k)$ and $d_{jn}(k)$ behave as $1/k$ if $|k| \to \infty$, for k complex as well as real. Thus, for large values of k, one can write

$$g(k,z) \approx \frac{r(k,z)}{k} \quad .$$

Since the integral

$$\int_{C_2} \frac{r(k,z)}{k} e^{iky} dk \;, \quad y > 0 \;,$$

vanishes as $R \to \infty$, as shown in C.3, and there are no branch points for the particular integral solutions, the integral

$$\int_{-\infty}^{\infty} g(k,z) e^{iky} dk$$

must vanish according to (C.4b). The same is true for $y < 0$, and thus the integral (C.4a) will vanish, for all x, when applied to the particular integral solutions of (2.32).

Considering the homogeneous solutions in section 2.2.6.3, one can see that $g(k,z)$ is identical to ${}^{j}\eta_{2mn}$ in equation (2.39). Tracing the origins of this term through the equations (2.36b) and (2.29), one finds that the behaviour of this term is controlled by the terms c_{jn} and d_{jn}, which are associated with the particular integral solutions, as $|k| \to \infty$. This results from the fact that $\exp(ikl_m z)$ remains finite as $|k| \to \infty$, as shown in section 2.2.6.1, providing the branch cuts have been properly chosen. Thus, the integral

$$\int_{C_2} g(k,z)e^{iky}dk, \quad y>0$$

will vanish as $R\to\infty$, as with the particular integral solutions. From (C.4b) one then has

$$\int_{-\infty}^{\infty} g(k,z)e^{iky}dk = -\sum_q \int_{B_q^+} g(k,z)e^{iky}dk, \quad y>0,$$

for the homogeneous solutions. In a similar fashion, for $y<0$, one has

$$\int_{-\infty}^{\infty} g(k,z)e^{iky}dk = -\sum_p \int_{B_p^-} g(k,z)e^{iky}dk \quad .$$

Hence, for the homogeneous solutions, and $0\leq|x|<D/2$, (C.4a) has the value

$$\frac{1}{2i}\left\{ \sum_p \int_{B_p^-} g(k,z)e^{ik(x-D/2)}dk - \sum_q \int_{B_q^+} g(k,z)e^{ik(x+D/2)}dk \right\} \quad .$$

And for $x>D/2$, the value is given by

$$-\sum_q \int_{B_q^+} g(k,z)\sin(kD/2)e^{ikx}\,dk \quad ,$$

where B_q^+ and B_p^- are as previously defined in C.3.

When one ignores the branch point contributions, as is the case when evaluating the homogeneous solutions in section 2.2.6.3; or in the absence of branch points, as is the case for the particular integral solutions in 2.2.6.2, the integral (C.4a) has the value zero for all x.

C.5

Consider now the integral

$$\int_{-\infty}^{\infty} \frac{\sin(kD/2)}{(k+b)}\,e^{ikx}dk, \quad D>0 \quad , \qquad \text{(C.5a)}$$

where $b = B + i\varepsilon$, $\varepsilon << B$. This integral can be written

$$\frac{1}{2i}\left\{\int_{-\infty}^{\infty}\frac{e^{ik(x+D/2)}}{(k+b)}\,dk - \int_{-\infty}^{\infty}\frac{e^{ik(x-D/2)}}{(k+b)}\,dk\right\} .$$

Thus it is necessary to evaluate integrals of the form

$$\int_{-\infty}^{\infty}\frac{e^{iky}}{(k+b)}\,dk .$$

The above integral has a pole at $k = -b$, which does not lie on the real axis. Thus, for $y > 0$, the contour of integration is given by[31]:

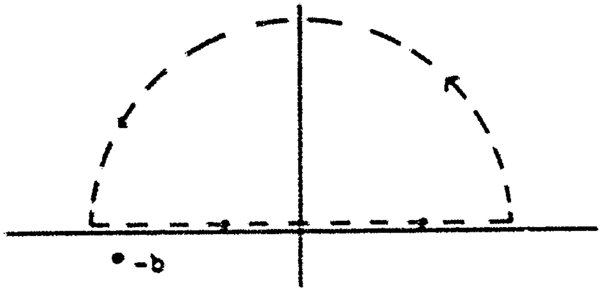

Since no poles occur within this contour,

$$\int_{-\infty}^{\infty}\frac{e^{iky}}{(k+b)}\,dk = 0, \qquad \text{for } y > 0.$$

For $y < 0$, the contour is given by[31]:

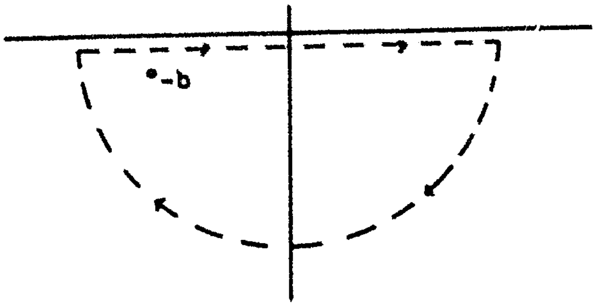

The pole at $k = -b$ occurs within this contour, and hence

$$\int_{-\infty}^{\infty} \frac{e^{iky}}{(k+b)}\,dk = -2\pi i\, e^{-iky}, \qquad \text{for } y < 0.$$

($-2\pi i$ since the contour is being travelled in a clockwise direction.)

In the case for $y = 0$, the integral

$$\int_{-\infty}^{\infty} \frac{e^{iky}}{(k+b)}\,dk$$

becomes

$$\int_{-\infty}^{\infty} \frac{dk}{(k+b)} = \int_{-\infty}^{\infty} \frac{k'dk'}{(k'^2+\epsilon^2)} - i\epsilon \int_{-\infty}^{\infty} \frac{dk'}{(k'^2+\epsilon^2)} \quad ,$$

where

$$k' = k + B \ .$$

The first of these integrals is zero, since the integrand is an odd function. The second integral can be written

$$-2i \int_{0}^{\infty} \frac{dx}{x^2+1} = -2i\left[\tan^{-1}x\right]_0^{\infty} = -i\pi \quad , \qquad x = k'/\epsilon \quad .$$

Thus,

$$\int_{-\infty}^{\infty} \frac{e^{iky}}{(k+b)} = -i\pi, \qquad \text{for } y = 0 \quad .$$

Therefore, the integral (C.5a) can be written:

$$\int_{-\infty}^{\infty} \frac{\sin(kD/2)e^{ikx}}{(k+b)}\,dk = \begin{cases} 0, & x > D/2 \\ \pi/2, & x = D/2 \\ \pi e^{-ib(x-D/2)}, & 0 < |x| < D/2 \\ \pi e^{ibD} - \pi/2, & x = -D/2 \\ 2\pi i \sin(bD/2)e^{-ibx}, & x < D/2 \end{cases} \ . \qquad \text{(C.5b)}$$

In a similar fashion :

$$\int_{-\infty}^{\infty} \frac{\sin(kD/2)e^{ikx}}{(k-b)}\, dk = \begin{cases} 2\pi i \sin(bD/2)e^{ibx}, & x > D/2 \\ \pi e^{ibD} - \pi/2, & x = D/2 \\ \pi e^{ib(x+D/2)}, & 0 \leq |x| < D/2 \\ \pi/2, & x = -D/2 \\ 0, & x < -D/2 \end{cases} \qquad (C.5c)$$

C.6

Consider the integral

$$\int_{-\infty}^{\infty} \frac{\sin[(k+A)D/2]e^{ikx}}{(k+A)(k+b)}\, dk \quad , \quad D > 0 \quad , \qquad (C.6a)$$

where A is real and $b = B + i\epsilon$, $\epsilon << B$. Using a partial fraction expansion, (C.6a) can be written

$$\left[\frac{1}{(b-A)}\right]\left\{ \int_{-\infty}^{\infty} \frac{\sin[(k+A)D/2]e^{ikx}}{(k+A)}\, dk - \int_{-\infty}^{\infty} \frac{\sin[(k+A)D/2]e^{ikx}}{(k+b)}\, dk \right\} \quad .$$

Substituting $k' = k + A$, and using (C.2b), the first integral has the value:

$$e^{-iAx} \times \begin{cases} \pi & , 0 \leq |x| < D/2 \\ \pi/2, & |x| = D/2 \\ 0 & , |x| > D/2 \end{cases} \quad .$$

The second integral can be written

$$\frac{1}{2i}\left\{ e^{iA\,D/2} \int_{-\infty}^{\infty} \frac{e^{ik(x+D/2)}}{(k+b)}\, dk - e^{-iA\,D/2} \int_{-\infty}^{\infty} \frac{e^{ik(x-D/2)}}{(k+b)}\, dk \right\} \quad .$$

Both of these integrals are of the form

$$\int_{-\infty}^{\infty} \frac{e^{iky}}{(k+b)}\, dk \quad ,$$

which is evaluated in section C.5.

Therefore:

$$\int_{-\infty}^{\infty} \frac{\sin[(k+A)D/2]e^{ikx}}{(k+A)(k+b)}\,dk = \begin{cases} \dfrac{\pi e^{-iAx}}{(b-A)} - \dfrac{\pi e^{-ibx} e^{i(b-A)D/2}}{(b-A)}, & -D/2 < x < D/2 \\ 0, \quad x > D/2 & \\ -2\pi i\,\dfrac{\sin[(A-b)D/2]e^{-ibx}}{(A-b)}, & x < -D/2 \end{cases} ;$$

(C.6b)

and in a similar fashion:

$$\int_{-\infty}^{\infty} \frac{\sin[(k+A)D/2]e^{ikx}}{(k+A)(k-b)}\,dk = \begin{cases} -\dfrac{\pi e^{-iAx}}{(A+b)} + \dfrac{\pi e^{ibx} e^{i(A+b)D/2}}{(A+b)}, & -D/2 < x < D/2 \\ \dfrac{2\pi i}{(A+b)} \sin[(A+b)D/2]e^{ibx}, & x > D/2 \\ 0, \quad x < -D/2 & \end{cases} .$$

(C.6c)

APPENDIX D

In section 2.2.6.3 our attention was drawn to the existance of branch points in the integrands of the equations (2.35)

$$V_j^M(x,z) = (\tfrac{1}{2}\pi)\sum_M\sum_m\int_{-\infty}^{\infty}\left[P_m(k)\,\frac{A_{mn1}}{A} + \sin(kD/2)\,\frac{A_{mn2}}{A}\right]a_{jm}e^{ikl_m z}e^{ikx}dk\;. \tag{2.35}$$

This appendix presents a general discussion of these branch points; however, a complete mathematical treatment of branch points will be avoided. There are many texts available which cover the topic in considerable detail, of which that by Fuchs and Shabat[26] is a good example. Our discussion will concern the origins as well as the mathematical and physical implications of the branch points in (2.35). Also the means of locating them and the problems they present in the evaluation of (2.35) will be considered. A means of evaluating the "branch point contributions" to the integrals (2.35) will be presented; however, due to the complexity of the expressions, no attempt will be made to obtain these contributions.

D.1 The Origins and Mathematical Implications of the Branch Points in (2.35)

The secular equation (2.17),

$$\begin{aligned}&[c_{55}c_{33} - c_{35}^2]l^4 + 2[c_{15}c_{33} - c_{35}c_{13}]l^3\\ &+ [c_{11}c_{33} + c_{35}^2 + 2c_{15}c_{35} - (c_{55} + c_{13})^2 - (c_{33} + c_{55})(\tfrac{\rho\omega^2}{k^2})]l^2\\ &+ 2[c_{11}c_{35} - c_{15}c_{13} - (c_{35} + c_{15})(\tfrac{\rho\omega^2}{k^2})]l\\ &+ [c_{11}c_{55} - c_{15}^2 - (c_{55} + c_{11})(\tfrac{\rho\omega^2}{k^2}) + (\tfrac{\rho\omega^2}{k^2})^2] = 0 \quad ,\end{aligned} \tag{2.17}$$

represents the relationship between the wave number, k, and the roots, l_m, which determine the "eigenfunctions", $\exp(ikl_m z)$, of the homogeneous solutions. Equation (2.17) is quartic in l, and for any value of k, at a fixed frequency ω, there exist four roots $l_1,\ldots,l_4$. This is true for both layer and substrate materials and for all values of k, even those which are complex, though our interest is largely confined to real values. Thus, equation (2.17) can be considered a "mapping" from k-space to l-space, to be abbreviated $(k \rightarrow l)$. Multivalued functions of this nature lead to representation problems since the solutions are not unique, and hence it is difficult to establish a "one-to-one" correspondence between the variables. For complex variables, this representation problem has been solved with the concept of the "Riemann surface"[26,31]. In the situation described by (2.17), the Riemann surface for k-space consists of four "sheets", each sheet containing an entire complex plane. Each of the roots l_m is associated with k upon a particular sheet; however, the value of k on each sheet must be the same. The points in k-space which give equal values to the "branches", i.e., roots of the multivalued function, are known as "branch points".* The lines of intersection between the different sheets of the Riemann surface, by which means one can pass from one sheet to another, are known as "branch cuts". The branch points are unique and, in general, the branch cuts are not unique, though this may depend on the particular situation.

As an example, consider the simple function $w = y^{\frac{1}{2}}$, where both variables are complex. The Riemann surface for the variable y has two sheets, with branch points at $y = 0$ and $y = \infty$. A branch cut will exist between these two limits and a possible pictorialization of this Riemann surface is shown in Fig. D.1.

---

* In the strictest sense, we should really consider the separate branches of (kl) as a function of k, as will be seen in D.3. However, any point k_b which is a branch point for $(k \rightarrow l)$ must obviously be a branch point for $(k \rightarrow kl)$.

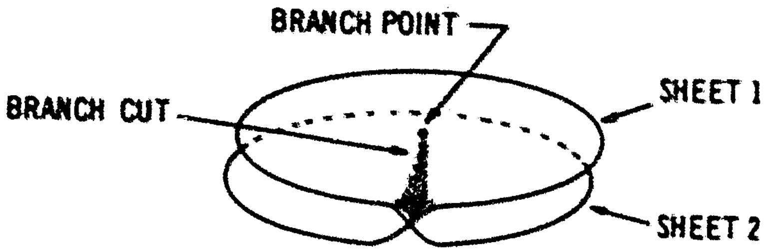

Figure D.1

To illustrate the problem to be encountered in performing the integration of (2.35), consider the simple integral

$$\int_C F(l)dk \quad ; \qquad (D.1)$$

where C is a closed contour in complex k-space, and l is defined by $l = k^{\frac{1}{2}}$. There are two roots, l_1 and l_2 (for the positive and negative sign, respectively), for every value of k, and branch points occur at $k = 0$ and $k = \infty$. Hence, the Riemann surface for k-space, in this problem, consists of two sheets which could be shown as in Fig. D.1. Assume that $F(l) = F(l_1)$, and thus the variable k is taken from the first sheet for the evaluation of (D.1). Furthermore, assume that F(l) is analytic over the whole of k-space. Due to the presence of branch points, the contour C must be constructed so as to remain on the first sheet only, and hence it cannot intersect the branch cut. Such a contour is shown in Fig. D.2, where the branch cut has been arbitrarily chosen to lie on the positive real axis. Thus $C = C_1 + B_1$:

C_1 = the circular portion of the contour

B_1 = that portion of the contour which goes around the branch point.

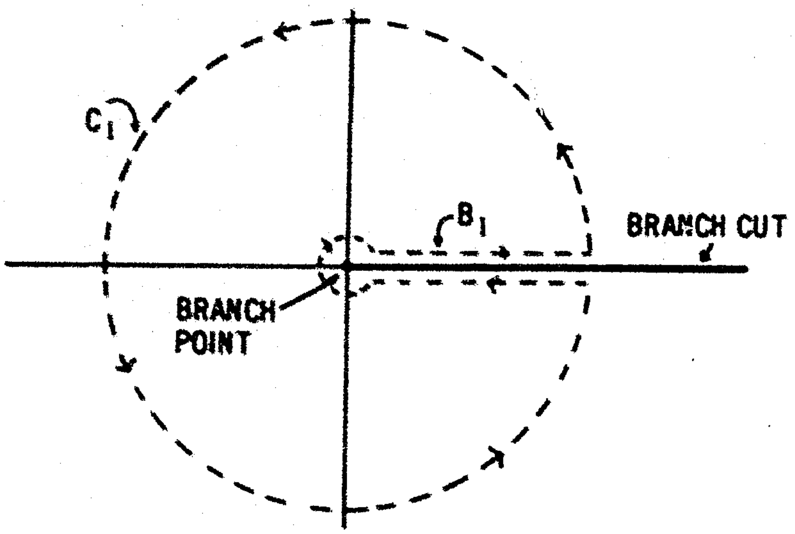

Figure D.2

Since $F(l)$ is analytic over all of k-space, and thus within and on the contour C,

$$\int_{C} F(l_1)dk = \int_{C_1} F(l_1)dk + \int_{B_1} F(l_1)dk = 0 \quad .$$

However, due to the presence of the branch cut, the integral over B_1 is not equal to zero[40]. Hence, the integral over C_1 is not equal to zero, and the integral (D.1) has a "branch point contribution" arising from the integration over B_1.

A useful variation of (D.1) is the integral

$$\int_{C} [F(l_1) + F(l_2)]dk \quad , \tag{D.2}$$

where l_1 and l_2 are the roots of $l = k^{\frac{1}{2}}$, as before. This integral separates into two separate integrals

$$\int_{C} F(l_1)dk \quad \text{and} \quad \int_{C} F(l_2)dk \quad .$$

The value of k, and hence the contour C, for the first integral is on the first sheet of the Riemann surface for k-space, and on the second sheet for the latter integral. The contour C must be the same in both sheets in this instance. Using the results of (D.1), one can write

$$\int_C F(l_1)dk + \int_C F(l_2)dk = \int_{C_1} F(l_1)dk + \int_{B_1} F(l_1)dk + \int_{C_2} F(l_2)dk + \int_{B_2} F(l_2)dk \ ;$$

where C_2 and B_2 are the equivalents of C_1 and B_1, but on the second sheet. However, since the contours C_1 and C_2 describe a contour that circles the branch point twice, it can be shown that[40]

$$\int_{C_1} F(l_1)dk + \int_{C_2} F(l_2)dk = 0 \quad .$$

(This is the equivalent of integrating F(l) twice around the branch point.) Hence,

$$\int_{B_1} F(l_1)dk + \int_{B_2} F(l_2)dk = 0,$$

and the integral (D.2) does not have any "branch point contribution".

Thus, if the integrand involves all of the roots l, in the fashion shown by (D.2), the value of the integral will be unaffected by the intersection of a branch cut with the contour of integration. If, however, the integrand does not involve all of the roots in a like fashion, the intersection of branch cuts by the contour of integration must be avoided, and the resulting integral has a "branch point contribution".

The integral (2.35) can involve all four of the layer roots, but only two of the possible four substrate roots due to the necessity of having solutions which do not increase as z goes to $-\infty$. The functional dependence upon each root is identical. Thus, the contour of integration used in the evaluation of (2.35) (see Appendix C.3 and C.4) must be constructed to avoid the branch points and branch cuts for the substrate solutions. If the contour crosses a branch cut originating from the layer roots, these roots will be permuted as[31]

$$l_3 \rightarrow l_4 \rightarrow l_3 \rightarrow l_4 \rightarrow l_3$$

and the value of the integrand will remain unchanged. Thus, the only branch point contributions to the integral (2.35) arise in the substrate solutions, due to the necessity of avoiding the intersection of the contour of integration with the substrate branch cuts.

D.2 Location of the Branch Points

As mentioned in section D.1, the branch cuts terminate at the branch points; and, to be able to construct the contour of integration for the integrals (2.35) in a logical fashion, one must know the location of the branch points. The location of the branch points for $(k \rightarrow l)$, as defined by (2.17) is not obvious; however, it can be shown that the branch points of a multivalued function can be found by considering the inverse mapping, if single valued[40]. To simplify the algebra, let $v^2 = \omega^2/k^2$ in equation (2.17), which can then be represented $(v^2 \rightarrow l)$, and consider the inverse mapping $(l \rightarrow v^2)$, given by[*]

$$v^2 = \left\{ P_1(l) \pm [P_2(l)]^{\frac{1}{2}} \right\} / 2\rho \quad ; \qquad (D.3)$$

(the symbol $\frac{1}{2}$ implies the positive square root)

---

[*] As mentioned in the preceeding section, one should look for branch points in $(k \rightarrow kl)$; however the inverse $(kl \rightarrow k)$, obtained by multiplying (2.17) by k^4 is more involved than $(l \rightarrow v^2)$. Hence, since the branch points in $(k \rightarrow kl)$ coincide with those in $(k \rightarrow l)$, we shall be content to study $(l \rightarrow v^2)$ to obtain the branch points in $(k \rightarrow l)$ or $(v^2 \rightarrow l)$.

where:

$$P_1(l) = (c_{33} + c_{55})l^2 + 2(c_{15} + c_{35})l + (c_{11} + c_{55})$$

$$\begin{aligned} P_2(l) = {} & [(c_{33} - c_{55})^2 + 4c_{35}^2]l^4 + [4(c_{33} + c_{55})(c_{35} + c_{15}) + 8c_{35}(c_{13} - c_{15})]l^3 \\ & + [4(c_{35}^2 + c_{15}^2) + 2(c_{11} - c_{55})(c_{55} - c_{33}) + 4(c_{55} + c_{13})^2 - 8c_{15}c_{35}]l^2 \\ & + [4(c_{35} + c_{15})(c_{11} + c_{55}) - 8(c_{35}c_{11} - c_{15}c_{13})]l \\ & + [(c_{11} - c_{55})^2 + 4c_{15}^2] \quad . \end{aligned}$$

It is interesting to observe that (D.3) represents two separate single valued mappings from l-space to v^2-space, depending on the choice of sign, and each must be considered separately. Branch points in $(v^2 \to l)$ are located at values of $l = l_o$ such that[40]

$$[d(v^2)/d(l)]_{l_o} = 0 \quad .$$

Taking the derivative of (D.3) generates two equations

$$2P_2^{\frac{1}{2}} P_1' \pm P_2' = 0 \,, \tag{D.4}$$

where the prime denotes d( )/d(l). Equation (D.4) yields three roots, l_o, for each sign; and upon substituting them into (D.3), the values of $v^2 = v_b^2$, which are the branch points for $(v^2 \to l)$, are determined. The values of $k = k_b$, which are the branch points in k-space, are then given by

$$k_b = \pm \omega / v_b \quad .$$

Although equation (D.4) yields three values of l_o for each sign, computation shows that each set of three roots (one set for each sign) corresponds to only one value of v^2. Hence, there exist only two values of v^2, and four values of $k = k_b$, at which branch points occur. The reasoning behind this situation will be considered further in section D.4 regarding the physical implications.

It is useful to note that, if $c_{15} = c_{35} = 0$, the values of v at which the branch points occur are equal to the bulk wave transverse and longitudinal velocities*. Also, when considering a real system in which loss occurs, the values of k_b will be complex.

D.3 Location of the Branch Cuts

The location of the branch cuts is arbitrary with respect to the integrals (2.30), for these are integrals along the real axis only. It is when one has to evaluate the integrals (2.39) in the manner outlined in Appendix C that the location of the branch cuts becomes important. As indicated in Appendix C.3 and C.4, the branch cut must be chosen such that the integrals vanish along that portion of the contour which encloses the upper or lower half of the complex k-plane ($|k| \to \infty$). This problem is analogous to that encountered in the study of electro-magnetic surface wave generation and propagation[14], and similar techniques can be employed. The branch cut must be chosen so as to separate those solutions with $\text{Imag}(kl) < 0$, and that decay in the substrate, from those with $\text{Imag}(kl) > 0$, which do not decay**. The contour (branch cut) which provides this separation is given by the solution of[14]

$$\text{Imag}(kl) = 0 \quad . \qquad (D.5)$$

Since there are four values of k which are branch points, as mentioned earlier, there will be two sets of branch cuts determined by (D.5). Once the path of the branch cut is determined, the contour of integration around the branch points, as used in Appendix C.3 and C.4, is chosen so as to

---

* The allowed values of velocity for bulk waves whose planes of constant phase are normal to the x-axis.

** It is for this reason that one must consider the branch points for $(k \to kl)$, in the strictest sense, as previously mentioned.

exclude the branch point from the desired region of k-space without crossing the branch cut. This contour must be chosen to follow the branch cut for it is only along this path that one can enter from $|k| = \infty$, and return, while keeping the integral on the same sheet of the Riemann surface.

Consider now the shape of the branch cuts for the simplest of substrate materials, one which is isotropic. In this instance

$$c_{11} = c_{33}$$

$$c_{15} = c_{35} = 0$$

$$c_{13} = c_{11} - 2c_{55} \quad ,$$

and equation (2.17) can be written

$$c_{11}c_{55}l^4 + \left[2c_{11}c_{55} - (c_{11} + c_{55})\frac{\rho\omega^2}{k^2}\right]l^2 + \left[c_{11}c_{55} - (c_{11} + c_{55})\frac{\rho\omega^2}{k^2} + \left(\frac{\rho\omega^2}{k^2}\right)^2\right] = 0 .$$

This has the solutions:

$$l^2 = \left(\frac{\rho\omega^2}{c_{11}k^2} - 1\right) \quad \text{and} \quad l^2 = \left(\frac{\rho\omega^2}{c_{55}k^2} - 1\right) \quad .$$

Thus, as $|k| \to \infty$ (k real), $l = \pm i$, as mentioned in section 2.2.6.1. One then has

$$(kl)^2 = (A^2 - k^2) \quad ,$$

where $A^2 = \dfrac{\rho\omega^2}{c_{11}}$ or $\dfrac{\rho\omega^2}{c_{55}}$. This equation, combined with (D.5) gives

$$\mathrm{Imag}(kl) = \mathrm{Imag}[(A^2 - k^2)^{\frac{1}{2}}] = 0,$$

which determines the shape of the branch cut. Assume, for the moment, that

$$A = a' + ia''$$

$$k = k' + ik'' \quad ,$$

then the above equation can be written

$$\text{Imag}\left\{\left[(a'^2 - a''^2) - (k'^2 - k''^2) + 2i(a'a'' - k'k'')\right]^{\frac{1}{2}}\right\} = 0 \quad .$$

This equation can be satisfied by

$$a'a'' = k'k''$$

providing

$$\left[(a'^2 - a''^2) - (k'^2 - k''^2)\right] > 0 \quad .$$

The first of these relationships describes a set of hyperbolas passing through the branch point $k = A$. The second relationship defines the range of k over which the hyperbolas are valid representations of the branch cuts. As can be seen, the hyperbolic branch cuts are valid for $|k'| < |a'|$ and thus the branch cuts appear as shown in Fig. D.3. In the absence of loss, the branch cuts degenerate to paths lying on the real and imaginary axes.

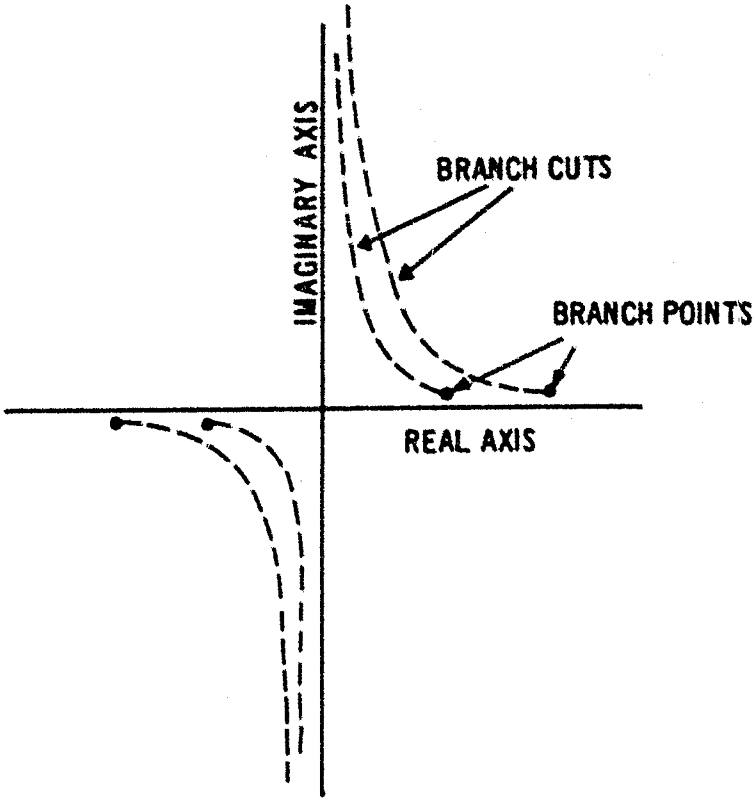

Figure D.3

To complete this section, it is useful to consider, qualitatively, the following two situations:[*]

(1) "Slow" layer material on a "fast" substrate

(2) "Fast" layer material on a "slow" substrate,

where "fast" and "slow" refer to the relative surface wave velocities of the two materials. First let us examine the situation (1). In the absence of a layer, the surface wave velocity is slightly less than the transverse bulk wave velocity[50]. Thus in k-space, the free surface $k = k_{s1}$ is slightly greater than the values of k corresponding to the branch points, k_{b1} and k_{b2}. (Where k_{b1} and k_{b2} are equal, or almost equal, to the values of k for transverse and longitudinal bulk waves in the substrate, respectively.) This is shown in Fig. D.4a. Upon the addition of a "slower" layer material, the surface wave velocity is depressed and the value of k_s increases, as shown by the arrows in Fig. D.4a[1,50].

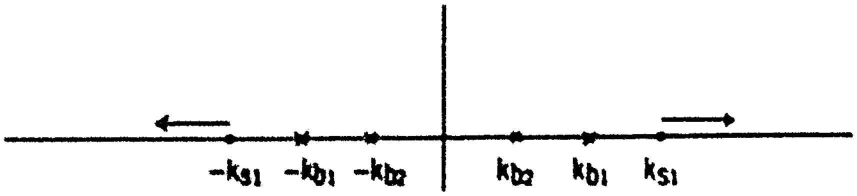

Figure D.4a

Even if numerous modes are present, as is possible in this situation[1,50], all $k_s \geq k_{s1}$. Thus, for a "slow" layer on a "fast" substrate, the surface wave k does not come very close to the branch points k_{b1} and k_{b2}, the closest value being k_{s1}, the value for free surface propagation.[*]

---

[*] Assuming a fixed frequency in the vicinity of the "resonant" frequency.

Consider now the inverse situation. Again, in the absence of a layer material, the relationships between k_{s1}, k_{b1} and k_{b2} are shown by Fig. D.4b.*

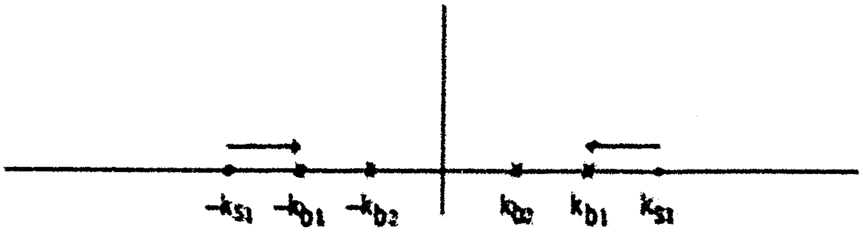

Figure D.4b

However, upon the addition of a "faster" layer material the surface wave velocity increases[1], and k_s moves in the direction of the arrows in Fig. D.4b. Thus, the surface wave k approaches the values of k at the branch points as the layer thickness is increased.*

In the absence of loss, k_s, k_{b1} and k_{b2} will be real and thus it is possible for k_s to equal k_{b1} or k_{b2}. This presents a problem since the branch points must be excluded from the contour that includes k_s; however, this problem is resolved by the inclusion of loss.

D.4 Physical Implications of the Branch Points

The branch points were defined in section D.1 as those values of k at which the roots (or pairs of roots) of equation (2.17) are equal. If one were to plot the locus of a single pair of roots of (2.17) as a function of k (real and with decreasing magnitude), it would appear as shown in Fig. D.5 .

---

* See footnote on page 193

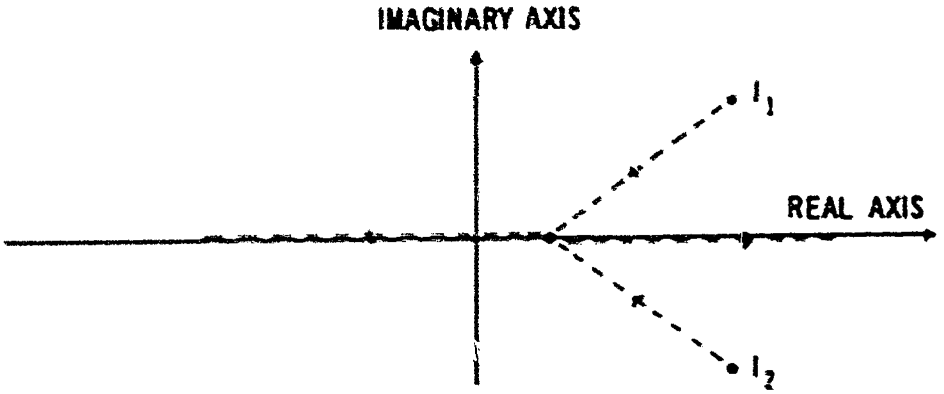

Figure D.5

For large values of $|k|$, the roots are complex and appear in conjugate pairs. As $|k|$ decreases, the roots approach each other until they meet on the real axis, at which point they are equal. As $|k|$ tends toward zero, the roots diverge along the real axis; however, (kl) approaches a finite value as $|k| \to 0$, as shown in section 2.2.6.1. Since the branch points occur at those values of k at which the roots of (2.17) become equal, and hence real as seen in Fig. D.5, they represent the maximum values of k, or minimum values of phase velocity v, at which bulk waves (i.e., waves which do not decay with depth) can occur[36]. There are only three distinct roots at these values of k (two of the four are equal), and hence the fact that equation (D.4) had only three roots for each sign, all corresponding to the same velocity, is to be expected.

As mentioned earlier, if $c_{15} = c_{35} = 0$, the branch point velocities correspond with the bulk wave transverse and longitudinal velocities in our coordinate system. If, however, c_{15} and/or c_{35} are not equal to zero, one finds that the values of v_b are less than the appropriate values of velocity for transverse and longitudinal bulk waves. This can be observed by reconsidering Fig. D.5 and remembering that $l = 0$ is the required condition for bulk transverse and longitudinal waves as defined above. This leads to a new and more fundamental definition of the branch points; however, it will be stated without proof, for mathematical proof is difficult, although, it can be seen from physical intuition. "The branch points represent the minimum values of velocity for which a bulk wave mode can propagate in the substrate with its Poynting vector parallel to the surface (x-axis)."

In the theory of electromagnetic surface waves, the "branch point contribution" represents the continuous spectrum of waves which carry energy away from the surface[14]. By analogy, the same is true for our situation, and the "branch point contribution" (i.e., the sum of the integrals around each of the branch points) represents a continuous spectrum of propagating modes which carry energy into the substrate. No such modes can be launched into the layer for there is no place for the energy to go (it has been assumed that $z = H$ is a stress free surface), providing further physical proof for the absence of branch points in (2.35) for the layer solutions.

Thus, one can think of the ID transducer as launching, in addition to the surface waves, a whole spectrum of bulk modes which carry energy into the substrate and whose Poynting vectors are included at every angle from 0° to 90° with respect to the interface.

D.5 Branch Point Contributions (Bulk Wave Modes)

It has previously been shown that only the substrate solutions contain branch points. These solutions are given by equation (2.39) as :

$$W_j^H(x,z) = \left(\frac{1}{2\pi}\right) \sum_{m=1}^{2} \sum_{n} \int_{-\infty}^{\infty} \left\{ F_n(k) \left[\frac{{}^{j}A_{mn11}}{(k-k_s)} + \frac{{}^{j}A_{mn12}}{(k+k_s)} + \eta_{1mn}^{j} \right] \right.$$

$$\left. + \sin(kD/2) \left[\frac{{}^{j}A_{mn21}}{(k-k_s)} + \frac{{}^{j}A_{mn22}}{(k+k_s)} + \eta_{2mn}^{j} \right] \right\} e^{ikx} dk \quad . \qquad (2.39)$$

As mentioned in section 2.2.6.3, the branch point contributions, representing bulk wave modes, arise from the terms

$$\left(\frac{1}{2\pi}\right)\sum_{m=1}^{2}\sum_{n}\int_{-\infty}^{\infty}F_n(k)\eta^{j}_{1mn}e^{ikx}dk$$

and

$$\left(\frac{1}{2\pi}\right)\sum_{m=1}^{2}\sum_{n}\int_{-\infty}^{\infty}\sin(k\,D/2)\,\eta^{j}_{2mn}e^{ikx}dk \quad .$$

Let us consider only those contributions in the region x> D/2. As shown in Appendix C.3 and C.4, for x> D/2 the two integrals above can be written

$$-\left(\frac{1}{2\pi}\right)\sum_{m=1}^{2}\sum_{n}\int_{B_m^*}F_n(k)\eta^{j}_{1mn}e^{ikx}dk$$

and

$$-\left(\frac{1}{2\pi}\right)\sum_{m=1}^{2}\sum_{n}\int_{B_m^*}\sin k\,D/2\;\eta^{j}_{2mn}e^{ikx}dk \quad ,$$

respectively (ignoring the possible contributions from other singularities in the "multi-mode" case). By substituting for η^{j}_{1mn} and η^{j}_{2mn}, one can combine the above integrals and write the exact branch point contribution, for x> D/2, as*

$$W_j^{BP}(x,z) = -\left(\frac{1}{2\pi}\right)\sum_{m=1}^{2}\int_{B_m^*}\frac{\Lambda_m}{\Lambda}\alpha_{jm}e^{ikl_m z}e^{ikx}dk \quad . \qquad (D.6)$$

It will be useful to combine the expotential terms in (D.6), so that one can write

---

* This result can also be obtained by the direct integration of equation (2.39), using Cauchy's theorem and including the branch cuts to insure that the integral remains single-valued.

$$w_j^{IB}(x,z) = -\left(\frac{1}{2\pi}\right)\sum_{m=1}^{2}\int_{B_m^+}\frac{A_m}{A}\alpha_{jm}e^{ixf_m(k,\theta)}dk \quad , \qquad (D.7)$$

where $f_m(k,\theta) = (k + kl_m \tan\theta)$, $\tan\theta = z/x$.

Before continuing, let us reconsider the shape of the branch cuts. In section D.3 it was shown that for an isotropic, lossless material, the branch cuts lay on the real and imaginary axes of k-space. Figure D.5 shows that for k on the real axis, each pair of "conjugate" roots to equation (2.17) becomes real for $|k| < k_{bm}$, the value of the branch point for that particular root pair. Thus, for $|k| < k_{bm}$, the term kl_m is purely real, the condition required for the branch cut. Therefore, the branch cuts for any lossless material which is appropriate to equation (2.17) will have a portion that lies on the real k axis, in the region $|k| < k_{bm}$. The value of k for the remaining portion of the branch cut will be complex, and though it is purely imaginary in the isotropic case, it is not obvious that this is true for a more general situation. For convenience, we will restrict ourselves to that portion of the branch cut which lies on the real axis, for in the "far field" the contributions for a complex k will have decayed to zero. (Remember that $k = k_x$.) Thus, (D.7) can be approximated by

$$w_j^{IB}(x,z) \simeq -\left(\frac{1}{2\pi}\right)\sum_{m=1}^{2}\int_{b_m^+}\frac{A_m}{A}\alpha_{jm}e^{ixf_m(k,\theta)}dk \quad , \qquad (D.8)$$

where the abbreviated contour b_m^+ is shown in Fig. D.6. Over the contour b_m^+, the function $f_m(k,\theta)$ is purely real (in the absence of loss), and thus the equation (D.8) represents an integral that can be evaluated by the

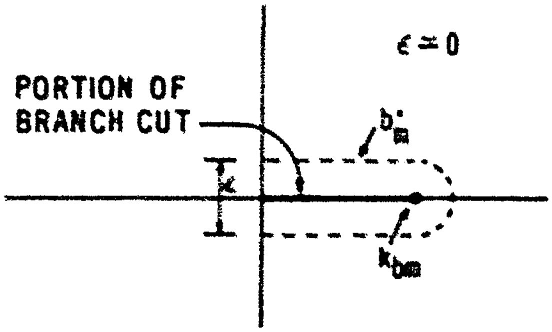

Figure D.6

method of "stationary phase"[11,67].

At this juncture we will terminate our discussion of branch points and bulk waves. The method of "stationary phase", applied to (D.8) will give an approximate, asymptotic solution to equation (D.7); however, it is obvious that the dominant contribution to the integral will occur in the vicinity of $k = k_{bm}$. Once the solution to (D.8) is found, the additional radiation conductance resulting from the generation of bulk wave modes can be found by returning to the Poynting vector used in Chapter III, and performing the calculations of the radiated energy using the solutions to equation (D.8).

APPENDIX E

The boundary condition equations (2.27) are written for the case of a "rigid" bond between layer and substrate. In the situation where the two materials are free to slide one upon the other, representing a "smooth" bond, the boundary conditions must be altered slightly. One cannot have continuity of tangential stress and displacements for the smooth bond, but rather the tangential stresses must vanish[1]. Thus the equation (2.27a) must be replaced by

$$T_5(x,0) = 0 \quad , \tag{E.1a}$$

and the equation (2.27d) by

$$\hat{T}_5(x,0) = 0 \quad . \tag{E.1b}$$

Applying the Fourier transform of (2.13) to the altered equations (2.27) gives the set of equations:

$$\bar{T}_5(k,0) = 0 \tag{E.2a}$$

$$\bar{U}_3(k,0) = \bar{W}_3(k,0) \tag{E.2b}$$

$$\hat{T}_3(k,0) = \bar{T}_3(k,0) \tag{E.2c}$$

$$\hat{T}_5(k,0) = 0 \tag{E.2d}$$

$$\hat{T}_3(k,H) = 0 \tag{E.2e}$$

$$\hat{T}_5(k,H) = 0 \tag{E.2f}$$

Replacing the equations (2.28) by the equations (E.2), one can proceed to the solutions in the same fashion as shown in Chapter II.

APPENDIX F

It was stated, in section 4.2, that a maximum of seven harmonic terms were used for the expansion of the applied potential function of the transducer, given by equation (2.9b)

$$\psi(x,z) = \sum_{n} A_n f_n(z) \cos(n\pi x/L) \quad , \qquad (2.9b)$$

and the usual procedure is to terminate the series when the term A_n is less than 5% of the largest. This appendix will present a simple argument to justify this truncation of the harmonic expansion. For convenience, we will restrict ourselves to consideration of the "bipolar" drive case, for which the allowed values of 'n' are

$$n = 1,3,5,7, \ldots \quad ;$$

however, a discussion of the "unipolar" drive case will follow in a similar fashion. Since the purpose is to observe the relative contributions to the total wave solutions at a particular value of k, it is easier to consider the wave solutions in (k,z) space.

Inspection of the boundary condition equations, (2.29), shows that the coefficients C_m for the homogeneous solutions are directly related to the particular integral solutions as well as the terms $\bar{\phi}$ and $\phi(D/2)\sin(kD/2)$. Equations (2.23) - (2.26) show that the particular integral solutions are directly related to the functions $\bar{\phi}$ and $\phi(D/2)\sin(kD/2)$ and thus we will restrict ourselves to the two basic functions

$$\bar{\phi}(k,z) \quad \text{and} \quad \phi(D/2)\sin(kD/2) \,,$$

which are fundamental to all of the wave solutions.

The harmonic structure of the terms $\overline{\phi}$ and $\phi(D/2)$ was determined in Appendix A and presented in the definitions accompanying equations (2.15) as

$$\overline{\phi}(k,z) = \sum_n \lambda_n F_n(k) f_n(z)$$

and

$$\phi(D/2) = \sum_n \lambda_n N_n f_n(z) \quad ,$$

where

$$F_n(k) = \frac{\sin[(k - n\pi/L)D/2]}{(k - n\pi/L)} + \frac{\sin[(k + n\pi/L)D/2]}{(k + n\pi/L)}$$

$$N_n = \begin{cases} -1, & \text{if } m_o + n \text{ is odd} \\ +1, & \text{if } m_o + n \text{ is even, with } m_o L = D/2. \end{cases}$$

(Since $|\phi(D/2)| > |\phi(D/2)\sin(kD/2)|$ we shall consider the harmonic behaviour of $\phi(D/2)$ only.) It has been shown that the "weighting factors" λ_n are proportional to[24]

$$\frac{P_m(\cos\pi d/L)}{n} \quad ,$$

where $n = 2m + 1$, $m = 0,1,2,3, \ldots$. The P_m are the Legendre polynomials, d is the finger width and L is the center-to-center spacing of adjacent fingers. For $d/L = 0.5$, which is the usual case, the first three harmonics for the "bipolar" case are[19,24]

$$n = 1,5,9 \quad (m = 0,2,4) \ ,$$

with relative values of λ_n given by:

$$\lambda_1 = 1.0$$

$$\lambda_5 \simeq -0.1$$

$$\lambda_9 \simeq 0.05 \quad .$$

From the properties of Legendre polynomials[44], one can readily determine that the next four harmonics will be $n = 13, 17, 21, 25$ and that:

$$A_{13} \simeq -0.025$$

$$A_{17} \simeq 0.016$$

$$A_{21} \simeq -0.012$$

$$A_{25} \simeq 0.009 \quad .$$

One can thus see that the addition of harmonic terms for $n > 25$ will have no measurable effect on the function $\phi(D/2)$ and, in fact, the cumulative effect of the last four terms is considerably less than the effect of A_9. Thus, on this basis it would appear evident that seven terms of the harmonic expansion will certainly be sufficient, and to cut off the summation when the harmonic term is less than 5% of the largest is reasonable.

This assumption is even more valid for the function $\bar{\phi}$. For any value of $k \neq k_r$, where $k_r = \pi/L$, the function $F_n(k)$ decreases as $1/n$. Hence, the relative contributions to $\bar{\phi}$, given by $\bar{\phi}_n = A_n F_n(k) f_n(z)$ are:

$$\bar{\phi}_1 = 1.0$$

$$\bar{\phi}_3 \simeq -0.02$$

$$\bar{\phi}_5 \simeq 0.0055, \text{ etc.}$$

As can be seen, these terms decay very rapidly with increasing 'n', and hence termination of the summation after the first two or three terms is sufficient for accurate computation. Inspection shows that for $k = k_r$, the only term to contribute to $\bar{\phi}$ is $\bar{\phi}_1$.

We have made no mention of the layer thickness in the above discussion; however, as shown by Farnell et al.[24], when the layer thickness, H, is greater than about $0.2L$, the harmonic terms within the layer are essentially independent of H and are identical to those in the substrate.

BIBLIOGRAPHY

1. Achenbach, J.D., Epstein, H.I., Dynamic Interaction of a Layer and a Half-Space, J. of the Eng. Mech. Div., Proc. Amer. Soc. Civil Eng., EM-5, p. 27 (October 1967).

2. Armstrong, D.B., Investigation to Develop Acoustic Surface Wave Delay Lines for Microwave Frequencies to the Point where They can be used for Air Force Systems, Final Report AFCRL-70-0509 (1970).

3. Auld, B.A., Application of Microwave Concepts to the Theory of Acoustic Fields and Waves in Solids, IEEE Trans. on Micro. Theory and Tech., MTT-17, 11, p. 800 (November 1969).

4. Bateman, H., Tables of Integral Transforms, Vol. 1, McGraw Hill, N.Y., 1954.

5. Bateman, T., Elastic Moduli of Single-Crystal ZnO, J. Appl. Phys., 33, p. 3309 (1962).

6. Berlincourt, D.A., Curran, D.R., and Jaffe, H., Physical Acoustics, Vol. 1-A, Ed. by W.P. Mason, Academic Press, N.Y., 1964.

7. Berlincourt, D.A., Jaffe, H., and Shiozawa, L.R., Electroelastic Properties of the Sulfides, Selenides and Tellurides of Zinc and Cadmium, Phys. Rev., 129, 4, p. 1009 (February 1963).

8. Bernstein, B.T., Elastic Constants of Synthetic Sapphire at 27°C, J. Appl. Phys., 34, 1, p. 169 (January 1963).

9. Bleustein, J.L., A New Surface Wave in Piezoelectric Materials, Appl. Phys. Lett., 13, 12, p. 412 (December 1968).

10. Bogardus, E.H., Third-Order Elastic Constants of Ge, MgO, and Fused SiO_2, J. Appl. Phys., 36, 8, p. 2504 (August 1965).

11. Born, M., Wolf, E., Principles of Optics, 3rd Ed., Appendix III, Pergamon Press, Oxford, 1965.

12. Cermak, I.A., Silvester, P., and Wong, S.K., Capacitance Determination for Infinite Interdigital Structures, IEEE Trans. on Micro. Theory and Tech., MTT-18, 2, p. 116 (February 1970).

13. Cheng, D.K., Analysis of Linear Systems, Addison-Wesley, N.Y., 1959.

14. Collin, R.E., Field Theory of Guided Waves, Section 11.8, McGraw-Hill, N.Y., 1960.

15. Coquin, G.A., Tiersten, H.F., Detection of Piezoelectric Surface Waves, J. Amer. Acoust. Soc., 41, 4, p. 921 (1967).

16. Crisler, D.F., Cupal, J.J., and Moore, A.R., Dielectric, Piezoelectric and Electromechanical Coupling Constants of ZnO Crystals, Proc. IEEE, 56, p. 225 (1968).

17. De Klerk, J., Thin Film ZnO Transducers for Use in Microwave Devices, Ultrasonics, 8, 3, p. 159 (July 1970).

18. De Klerk, J., and Daniel, M.R., Measured Electrical Characteristics of Interdigital Surface Wave Transducers on $LiNbO_3$, Appl. Phys. Lett., 16, 4, p. 219 (March 1970).

19. Engan, H., Excitation of Elastic Surface Waves by Spatial Harmonics of Interdigital Transducers, IEEE Trans. on Elect. Devices, ED-16, 12, p. 1014 (December 1969).

20. Evans, D.R., Lewis, M.F., and Patterson, E., Sputtered ZnO Surface-Wave Transducers, Elect. Lett., 7, 18, p. 557 (September 9,1971).

21. Ewing, W.M., Jardentzky, W.S., and Price, F., Elastic Waves in Layered Media, McGraw-Hill, N.Y., 1957.

22. Fahmy, A.H., Structure and Properties of Sputtered ZnO Transducers, M. Eng. Thesis Electrical Engineering Department, McGill University, March 1971.

23. Farnell, G.W., Symmetry Considerations for Elastic Layer Modes Propagating in Anisotropic Piezoelectric Crystals, IEEE Trans. on Sonics and Ultrasonics, SU-17, 4, p. 229 (October 1970).

24. Farnell, G.W., Cermak, I.A., Silvester, P., and Wong, S.K., Capacitance and Field Distributions for Interdigital Surface Wave Transducers, IEEE Trans. on Sonics and Ultrasonics, SU-17, 3, p. 188 (July 1970).

25. Foster, N.F., Coquin, G.A., Rozgonyi, G.A., and Vannatta, F.A., CdS and ZnO Thin Film Transducers, IEEE Trans. on Sonics and Ultrasonics, SU-15, 1, p. 28 (January 1968).

26. Fuchs, B.A., Shabat, B.V., Functions of a Complex Variables and Some of Their Applications, Vol. 1, Pergamon Press, London, 1964.

27. Hanebrekke, H., Ingebrigtsen, K.A., Acoustoelectric Amplification of Surface Waves in Structure of CdSe Film on $LiNbO_3$, Elect. Lett., 6, 16, p. 520 (August 1970).

28. Hartemann, P., Dieulesaint, E., Acoustic Surface Wave Filters, Elect. Lett., 5, 25, p. 657 (December 11, 1969).

29. Hickernell, F.S., Private Communication with Dr. G.W. Farnell, May 1970.

30. Hickernell, F.S., Shulda, G.F., and Brewer, J.W., ZnO and CdS Overlay Surface Wave Transducers, Paper G-11, 1970 IEEE Ultrasonics Symposium, San Francisco, October 1970.

31. Hille, E., *Analytic Function Theory*, Vol. 1, Ginn & Co., N.Y., 1959.

32. Holland, M.G., Schulz, M.B., Matsinger, J.H., and Willingham, C.B., ZnO Overlay Film Surface Acoustic Wave Transducers, Paper P-3, Presented at the 1971 - IEEE Ultrasonics Symposium, Miami Beach, December 1971.

33. Humpryes, R.F., Ash, E.A., Acoustic Bulk-Surface-Wave Transducer, Elect. Lett., 5, 9, p. 175 (May 1969).

34. Jaffe, H., Berlincourt, D.A., Piezoelectric Transducer Materials, Proc. IEEE, 53, p. 1465 (1965).

35. Jones, W.S., Hartmann, C.S., and Claiborne, L.T., Evaluation of Digitally Coded Acoustic Surface-Wave Matched Filters, IEEE Trans. on Sonics and Ultrasonics, SU-18, 1, p. 21 (January 1971).

36. Joshi, S.G., White, R.M., Excitation and Detection of Surface Elastic Waves in Piezoelectric Crystals, J. Amer. Acoust. Soc., 46, 1.1, p. 17 (July 1969).

37. Kaplan, W., *Advanced Calculus* p. 555, Addison-Wesley, N.Y., 1959.

38. Kraus, J.D., *Antennas*, 1st Ed., McGraw-Hill, N.Y.,1950.

39. Lamb, H., On Wave in a Elastic Plate, Proc. Roy. Soc. London, 93A, p. 114 (1917).

40. LePage, W.R., *Complex Variables and the Laplace Transform for Engineers*, Section 5.15, McGraw-Hill, N.Y., 1961.

41. Loftus, D.S., Elastic Surface Waves on Layered Anisotropic Crystals, Appl. Phys. Lett., 13, p. 323 (November 1968).

42. Lord Rayleigh, On Waves Propagated Along the Plane Surface of an Elastic Solid, Proc. Lon. Math. Soc., 17, p. 4, (1885-86).

43. Love, A.E.H., *The Mathematical Theory of Elasticity*, 3rd Ed., Cambridge Press, 1920.

44. Margenau, H., Murphy, G.M., *The Mathematics of Physics and Chemistry*, 2nd Ed., Section 10.2, D. Van Nostrand, Princeton, N.J., 1956.

45. May, J.E., Jr., Ultrasonic Travelling Wave Devices for Communication, IEEE Spectrum, 2, p. 73 (October 1965).

46. Miller, G.F., Pursey, H., The Field and Radiation Impedance of Mechanical Radiators on the Free Surface of a Semi-Infinite Isotropic Solid, Proc. Roy. Soc. Lond., A-223, p. 521 (1954).

47. Morse, P.M., Feshbach, H., Methods of Theoretical Physics, Vol. 1, McGraw-Hill, N.Y., 1953.

48. Malamwar, A.L., Epstein, M., Immitance Characterization of Acoustic Surface Wave Transducers, Proc. IEEE, 60, 3, p. 336, March 1972.

49. Nye, J.F., Physical Properties of Crystals, Appendix E, Oxford, 1960.

50. Schmidt, R.V., Voltmer, F.W., Piezoelectric Elastic Surface Waves in Anisotropic Layered Media, IEEE Trans. on Micro. Theory and Tech., MTT-17, 11, pp. 920 (November 1969).

51. Schnitzler, P., Elastic Waves in a Layered System of CdS on Ge, Appl. Phys. Lett., 11, p. 273 (November 1967).

52. Schnitzler, P., Bergstein, L., and Strauss, L., Elastic Surface Waves: Thin Film Transducer and Layered System Dispersion, IEEE Trans. on Sonics and Ultrasonics, SU-17, 3, p. 185 (July 1970).

53. Schulz, M.B., and Matsinger, J.H., Rayleigh Wave Electromechanical Coupling Constants, (Unpublished - authors with Raytheon Research Division, Waltham, Mass.).

54. Skeie, H., Electrical and Mechanical Loading of a Piezoelectric Surface Supporting Surface Waves, J. Amer. Acoust. Soc., 48, p. 1098,(November 1970).

55. Slobodnik, A.J., Jr., and Conway, E.D., Microwave Acoustics Handbook, AFCRL-70-0164, Air Force Cambridge Research Labs. (1970).

56. Smith, A.B., Damon, R.W., A Bibliography of Microwave Ultrasonics, IEEE Trans. on Sonics and Ultrasonics, SU-17, 2, p. 86 (April 1970).

57. Smith, R.T., Temperature Dependence of the Electroacoustical Constants of Li-Doped ZnO Single Crystals, Abstract in J. Acoust. Soc. Amer., 46, 1.1, p. 105 (July 1969).

58. Smith, W.R., Gerard, H.M., Collins, J.H., Reeder, T.M., and Shaw, H.J., Analysis of Interdigital Surface Wave Transducers by Use of an Equivalent Circuit Model, IEEE Trans. on Micro. Theory and Tech., MTT-17, 11, p. 856 (November 1969).

59. Sneddon, I.N., Fourier Transforms, McGraw-Hill, N.Y., 1951.

60. Solie, L.P., Piezoelectric Acoustic Surface Waves for a Film on Substrate, Appl. Phys. Lett., 18, 4, p. 111 (February 1971).

61. Solie, L.P., Theoretical Study of Acoustic Waves in Layered Anisotropic Piezoelectric Crystals, Ph.D. Thesis, Microwave Laboratory, Stanford University, 1971.

62. Stern, E., Microsound Components, Circuits and Applications, IEEE Trans. on Micro. Theory and Tech., MTT-17, 11, p. 835 (November 1969).

63. Stoneley, R., Elastic Waves at the Surface of Separation of Two Solids, Proc. Roy. Soc. London, 106A, p. 416 (1924).

64. Stoneley, R., The Propagation of Surface Elastic Waves in a Cubic Crystal, Proc. Roy. Soc. London, 232A, p. 447 (1955).

65. Tancrell, R.H., Holland, M.G., Acoustic Surface Wave Filters, Proc. IEEE, 59, 3, p. 393 (March 1971).

66. Tiersten, H.F., Analysis of the Effect of Thin Isotropic Platings on Elastic Surface Wave Propagation in Isotropic Solids, Paper N-2, IEEE Ultra-Sonics Symposium, Vancouver, B.C., 1967.

67. Tyras, G., Radiation and Propagation of Electromagnetic Waves, Chapter 5.3, Academic Press, N.Y., 1969.

68. Vassell, M.O., Ganguly, A.K., Electric Field Distribution for a Surface Interdigital Transducer, IEEE Trans. on Elect. Devices, ED-18, 1, p. 66 (January 1971).

69. Viktorov, I.A., Rayleigh and Lamb Waves, Section 1.1, Plenum Press, N.Y., 1967.

70. Warner, A.W., Onoe, M., and Coquin, G.A., Determination of Elastic and Piezoelectric Constants for Crystals in Class (3m), J. Acoust. Soc. Amer., 42, p. 1223, 1967.

71. White, D.L., Sonic Circuits: A Wave-Guide System for Ultrasonic Surface Waves, Paper N-1, IEEE Ultrasonics Symposium, Vancouver, B.C., 1967.

72. White R.M., Surface Elastic Wave Propagation and Amplification, IEEE Trans. on Elect. Devices, ED-14, 4, p. 181 (April (1967).

73. White, R.M., Surface Elastic Waves, Proc. IEEE, 58, 8, pg. 1238 (August 1970).

74. White, R.M., Voltmer, F.W., Direct Piezoelectric Coupling to Surface Elastic Waves, Appl. Phys. Lett., 7, p.314 (December 1965).

75. White,R.M., Voltmer, F.W., Ultrasonic Surface-Wave Amplification in CdS, Appl. Phys. Letts., 8, 2, p. 40 (January 1966).

76. Wilde, D.J., *Optimum Seeking Methods*, Prentice-Hall, 1964.

77. Yoshida, K., Yamanishi, M., Interaction Between Surface Elastic Waves and Drifting Carriers in Layered System, Jap. J. Appl. Phys., 7, 9, p. 1143 (September 1968).